

POLISH ACADEMY OF SCIENCES – WROCLAW BRANCH
WROCLAW UNIVERSITY OF TECHNOLOGY

ARCHIVES OF CIVIL AND MECHANICAL ENGINEERING

Quarterly
Vol. V, No. 3

WROCLAW 2005



Selection of assembly equipment using expert system

B. REIFUR, T. JANKOWSKI

Wrocław University of Technology, Wybrzeże Wyspiańskiego 25, 50-370 Wrocław

In order to reduce the time of designing technological process and selection of optimal variant of process with regard to qualitative and economic aspects, expert systems are often used. Computer techniques improve and speed up the selection of assembly devices and also allow us to calculate the costs of their application in assembly process of a given product. Knowledge and experience of designer who cooperates with computer system make qualitative and quantitative aids of decision making in different stage of designing possible. In the paper, the use of techniques of Artificial Intelligence for creation of an expert system which aids decision making in the planning and selection of the elements of assembly devices like robot and gripper is presented.

Keywords: *robot, gripper, assembly, expert systems*

1. Introduction

The design of assembly and the selection of assembly tools constitute a multistage process which to a large extent determines the quality and price of manufactured machines. In order to obtain high quality and reliability of the manufactured machine, not only its individual components must be properly designed and made, but also their assembly and the assembly tools must be proper. The designer's knowledge and experience are the key elements which aid (both qualitatively and quantitatively) the design process and decision making at the different stages of design. The dispersion of knowledge, its complex structure and the difficult access to it greatly limit its availability. In this context, the efficient planning of assembly and the selection of assembly tools assume increasing importance.

To tap the procedural knowledge contained in software tools, the catalogue knowledge stored in databases and the expert knowledge stored in knowledge bases, an effective tool comprising solution search methodology, the selection of criteria and constraints and the determination of sought quantities, their values and directions of their variation are needed.

To shorten the time required for designing such a complex process as assembly and to achieve positive economic results, computer techniques and analyses aided by expert systems, artificial neural networks and relational databases are more and more often employed. In the design and visualization of assembly processes, expert systems should collaborate with computer-aided design (CAD) systems, production planning systems (PPS) and computer-aided assembly process planning (CAAPP) systems.

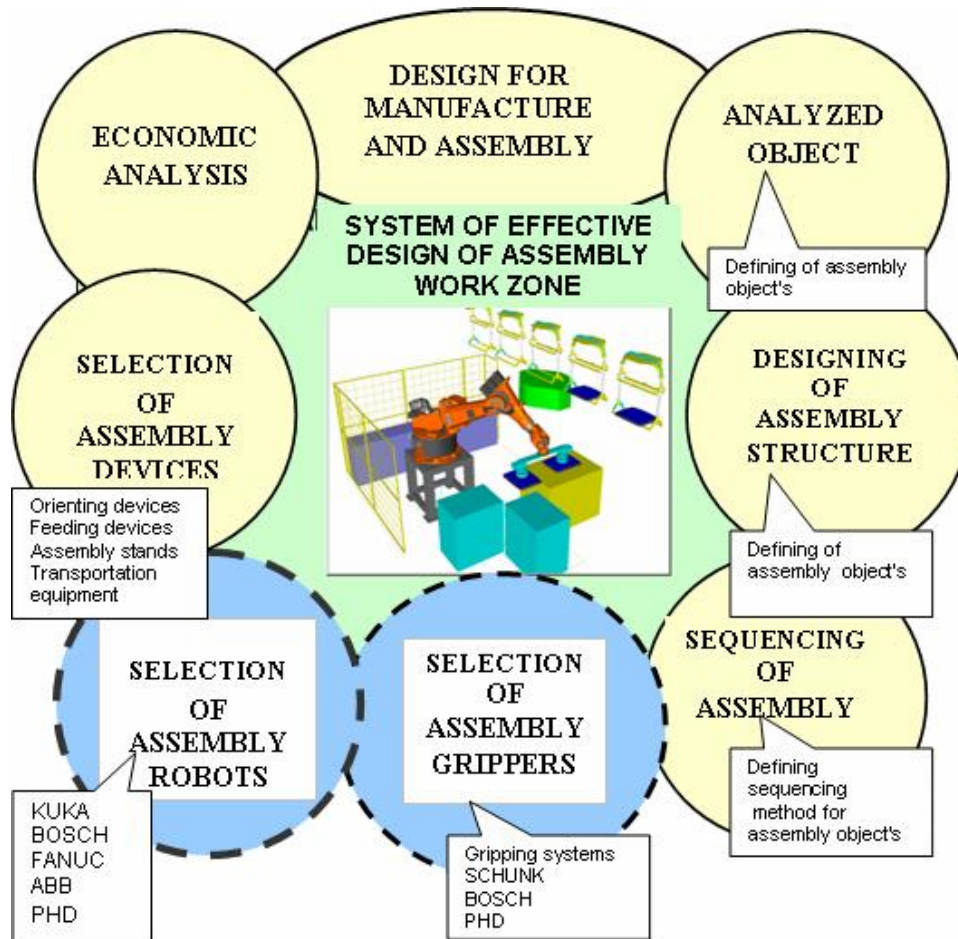


Fig. 1. Components of expert system for assembly work zone design

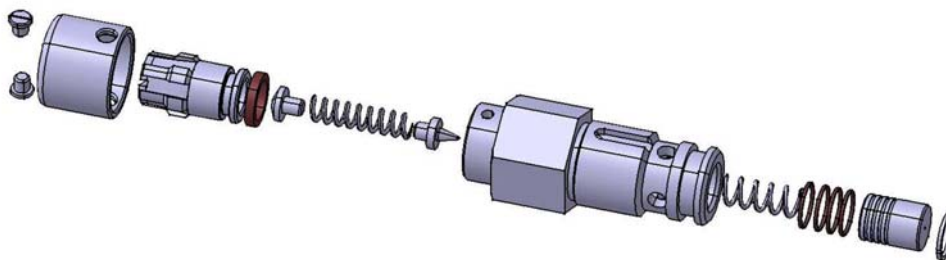


Fig. 2. Analyzed team of valve

By combining all these systems one can shorten the time of process design and select the optimum solutions for the technological process and for the tooling. The analysis of the process of optimum selection of the assembly–devices (the robot and gripper) was conducted for team of valve (see Figure 2).

2. Expert system software tools

An expert system aiding decision making in the planning and selection of assembly devices (including the estimation of costs connected with the use of the latter) has become an essential tool. Such systems are widely applied in order to solve highly technical problems requiring expertise and to perform complex tasks requiring great intellectual capacity [1, 2, 3]. Expert systems put forward solutions which the user can accept or reject and demand another solution.

The effectiveness of an expert system depends mainly on its database and to a lesser degree on its inference mechanism. The database contains knowledge (in the form of rules and facts) about the domain to which the problem belongs. The inference mechanism draws conclusions from the accumulated knowledge, which leads to the solution of the problem.

The system of GURU developed by the American company MDDBS and the Access 97 software for relational databases were used to build an expert system. The system forms an integrated environment (see Figure 1) which for prescribed conditions and costs selects assembly devices from a database on the basis of a knowledge base [4, 5]. This is illustrated in this paper for the selection of robot and grippers for a simple machine. GRIPPER and ROBNETEX expert systems and ASSEMBLY database, which stores catalogue data on robot and grippers, have been developed.

To create an expert system based on a knowledge base one must acquire knowledge from an expert (a human being) in a given field who often finds a solution to a problem on the basis of information about it and his/her own experience. An expert system which incorporates recorded expert knowledge in the given field can use this knowledge repeatedly in an economically effective way without the presence of the expert.

The power of an expert system to solve a given problem depends largely on the knowledge encoded in it and to a lesser degree on the formalism and the inference schemes which it uses. Briefly put, the fuller the knowledge about a given problem, the faster its solution [3, 5].

3. Expert system for selecting assembly equipment

An efficient system of configuring the assembly workspace should have an interface allowing the user to use advanced A.I. tools without entering their environments [6, 7, 8].

The success or failure of an expert system depends to a large extent on the ease of use and the quality of the user interface. To be user-friendly it must meet several requirements such as:

- the ease of use (it should not require long learning),
- errors in entered data (facts) should be early detectable and hints on how to correct them should be offered,
- the expert system's output should have a form acceptable to the user,
- the queries which the user must answer and the answers to the user's queries should be easily understood.

The interface (communication module) used here allows the user to communicate easily (in a way similar to a natural language) with the computer. The user-friendly interface is so designed that even users who do not know any programming can immediately use the program. The system which aids the design of a manufacturing process by automatically selecting an assembly robot or gripper is a component of a system for selecting assembly equipment for the assembly workspace. The latter is a hybrid system consisting of an expert system, a neural network, a database, and a user interface. It contains design data, technological data, knowledge and inference and association mechanisms needed for the selection of a robot or gripper. Its algorithm is shown in Figure 3.

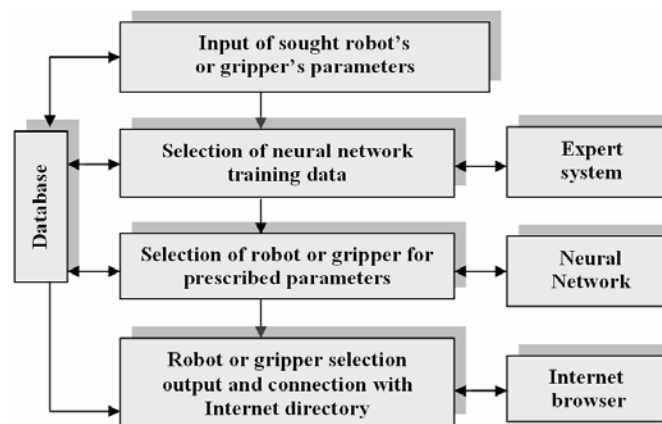


Fig. 3. Program algorithm

In the first step, the designer of the assembly process interactively enters some parameters of the sought robot or gripper which are encoded by the program. Then the expert system, having a knowledge of how to select patterns for neural network training from the database, is employed. A robot or gripper is selected by means of the neural network. First, the neural network is trained using data prepared by the expert system and then the trained neural network receives the sought robot's parameters. At the output the information about the type of the selected robot or gripper is obtained.

The expert system was used to provide patterns for the training of the neural network to the adequate level in the required range.

Data for neural network training are selected from the database on the basis of the information on the robot's application domain and its operating conditions assumed by the designer of the manufacturing process. The expert system's knowledge base incorporates rules according to which proper patterns are selected from the ones stored in the database.

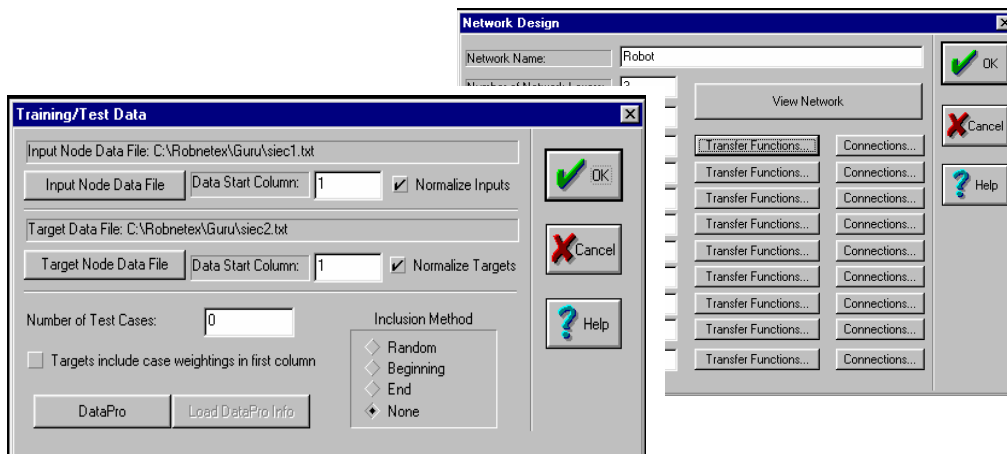


Fig. 4. Window for defining source sets for neural network training

A skeleton expert system, called Guru, was used to perform this task. The Qnet simulator with error back propagation training was used for the implementation of the neural network (Figure 4).

4. Selection of robot

The ROBNETEX user interface (see Figure 5) was created using the Delphi 3 software environment for the quick development of Windows applications. The interface consists of the following three main parts:

- data input,
- robot selection procedure,
- Internet directory of robots.

To define the sought robot in the ROBNETEX program, three groups of robot features, i.e. general, functional and spatial, are specified in the *data input* part.

General features define the robot's application domain with regard to the type of performed jobs and the conditions in which the robot is to work. They are used to reduce the number of potential solutions and the amount of neural network training data, whereby the learning time is considerably shortened.

Functional features define the sought robot's design parameters, i.e. the number of steered axles, the lifting capacity, the workspace size, the positioning accuracy and the speed of motion.

Spatial features define the way in which the robot can be mounted in the work area:

- immovable base – the robot secured to the floor or a wall or suspended from the ceiling,
- movable base – the robot moving (usually) along one axis,
- travelling robot: underhand or moving along one or two axes.

The *robot selection* part consists of three functions: neural network training data selection, neural network training and sought robot selection. The neural network training function is performed by the Qnet neural network simulator.

The *directory of robots* part has direct links to the Internet directories of robot manufacturers. By entering the robot's name and its type we can find the selected robot in the directory and obtain its numerical and graphical specifications. The program has links to the robot directories of BOSCH, ABB, Epson, Fanuc and Kuka. For analyzed team of valve (Figure 2) the system executed the choice of robot of the BOSCH firm introduced in Figure 5.

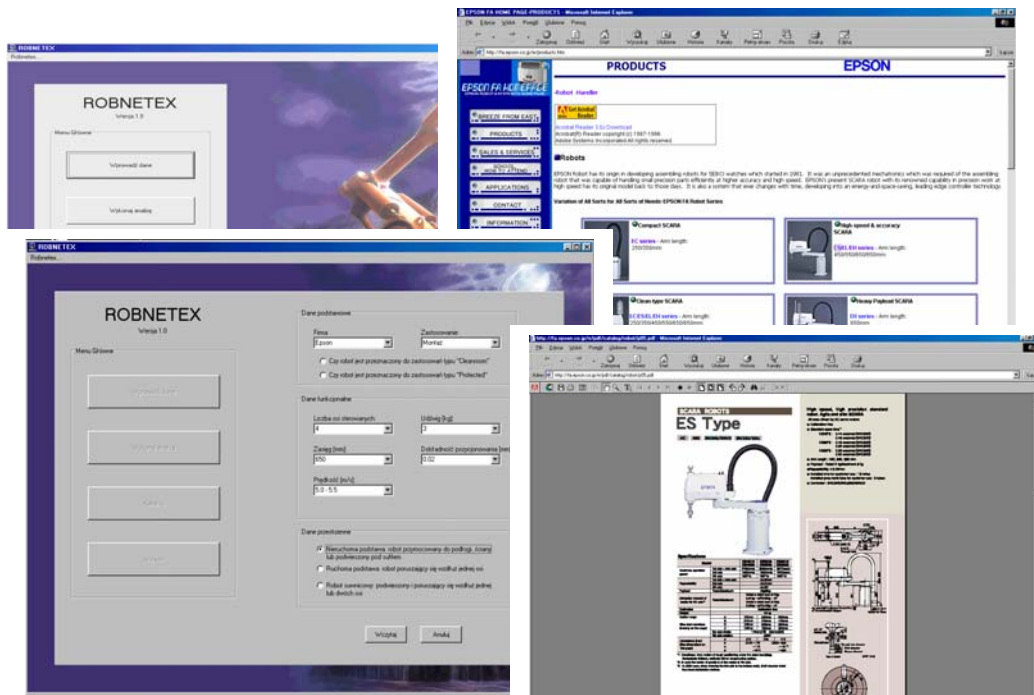


Fig. 5. The choice of robot by ROBOTEX system

The advantages gained from the ROBNETEX program are as follows:

- simple rules of the knowledge recording in expert system,
- processing of incomplete knowledge through neuronal net,
- taking advantage of literature,
- due to extension of base of robots it is possible to widen the range of accessible robots and the areas of their use,
- the service of the system is easy,
- quick results, low expenditure of work,
- no necessity of preview of many catalogues in order to find the solution,
- the possibility of quick selecting the robot demand.

5. Selection of gripper

To realize an assembly process, in which the state-of-the-art robots controlled by computers are employed, the robots must be equipped with sensors and executors such as grippers or tools.

In the manipulation process, the robot's gripping devices are used to perform the following elementary tasks:

- to grip the object of manipulation in the initial position,
- to hold it during manipulations,
- to release the object of manipulation in the target place.

A proper gripping of the object of manipulation depends on:

- the object's shape,
- the dimensions of the manipulated part,
- the object's weight,
- the position of the centre of mass,
- the moment of inertia,
- the kind of the object's material,
- the condition of the surface,
- the working tolerances of the gripped areas,
- the properties of the surface of gripped areas,
- the dynamic conditions of the manipulation and assembly processes.

As regards the gripper, the gripping of the object is determined by:

- the mode of gripping,
- the shape and geometric parameters of the gripping elements,
- the properties of the surface of the gripping elements,
- the force generated by the grippers' drives,
- the sensors.

For each technological task there exists the optimum gripper design. The selection of the proper gripper is thus of crucial importance for the process of manipulation.

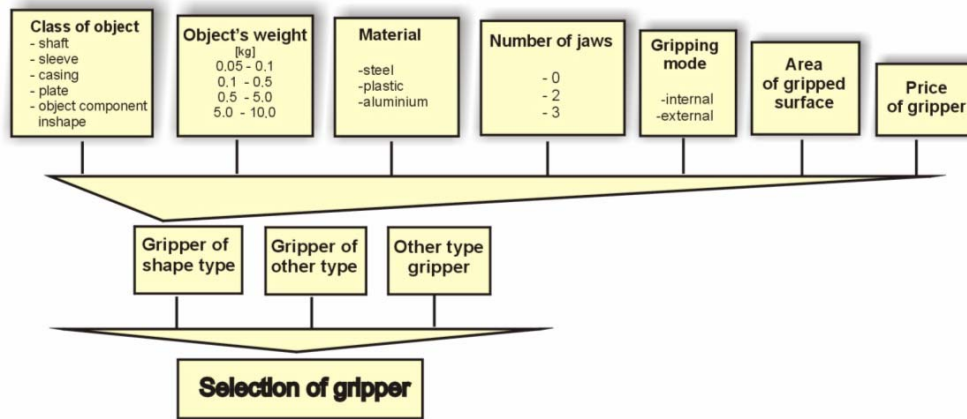


Fig. 6. Knowledge tree for gripper selection

The figure shows three screenshots from the CHWYTAK program. The top-left screenshot displays the input parameters for a gripper selection: 'Klasa przedmiotu : walek', 'Materiał przedmiotu : stal', 'Masa przedmiotu [kg] : 0.10', 'Powierzchnia uchwycenia przedmiotu : zewn', 'Liczba szczek chwytaka : 2.00', and 'Cena chwytaka : 300.00'. The top-right screenshot shows the program's output: 'Wybrano chwytak : silowy ze sztywnymi', 'Znaleziono pasujacych chwytakow : 2', and lists specifications for 'Typ : PGH30', 'Skok : 30.00', 'Udzwig : 2.60', 'Maxrozn : 60.00', and 'Koszt : 300.00'. The bottom-left screenshot shows the program's reasoning: 'Rule K1 (from c:/dyplo/chwytak.rsc) (fired)', 'Chwytak dobrano na podstawie katalogu firmy SCHUNK. W bazie danych ACCESS znajdziesz szczegolowe informacje odnosnie dobranego chwytaka.', and a list of rules: '(1) klasa przedmiotu manipulow += walek cf 100', '(4) rodzaj powierzchni chwytu += zewn cf 100', '(5) liczba szczek chwytaka += 2 cf 100', '(8) CHWYTAK += chwytak_silow cf 100', and 'CHWYTAK (from c:/dyplo/chwytak.rsc) K1 += chwytak_silowy cf 100'. The bottom-right screenshot shows a 3D model of a gripper with two arrows pointing to specific components: 'GS 65 to assembly of rings sealing up' and 'PGH 30 to assembly of metal elements'.

Fig. 7. Screens of CHWYTAK program elements

The purpose of the GRIPPER expert system is to aid decision making by the engineer during the selection and planning of assembly tools (grippers) for the design of the assembly of an object. On the basis of the user's specifications the system will select the proper gripper from the gripper database to grip the object which is to be assembled. The GRIPPER expert system is one of the subsystems in a global system for modelling the assembly work zone. The necessary information in the form of a knowledge tree (its fragment is shown in Figure 6) is entered as rules into GURU system. In the editor, besides writing a rule one must also enter the rule processing parameters. The rule consists of premise IF with conditions and conclusion THEN with objective variables. Then the variables must be specified and described. The description will be displayed when queries about the variables are made during consultation with the system or when the consultation process is being explained.

The program asks us if we want it to explain why and how and the goal of the consultation was achieved. If the answer is yes (Y by default), the program displays the explanations shown in Figure 7. If the answer is no (N), the consultation begins again.

The database is an important component of the system aiding the selection of assembly devices. It stores information about the parameters of the devices used in assembly and photographs of them. The gripper database is based on SCHUNK, SOMMER and BOSCH catalogues [9].

6. Conclusions

Computer software aiding the production engineer in the design of assembly and production planning processes plays an increasingly greater role, expanding design possibilities. An example of such software is the program presented which owing to the hybridization of the expert system and the artificial neural network makes for better and more efficient engineering design.

The main advantages of the presented system of aiding engineering design decisions by employing computer techniques and artificial intelligence methods can be itemized as follows:

- a reduction in design time;
- quick access to the results of work;
- if the initial data are changed, modifications can be easily made even at advanced stages of design;
- a reduction in design costs.

The program in conjunction with similar computer tools for the design of assembly workspace, including the selection of instrumentation, transport systems, feeders, gripping devices and so on, brings substantial benefits by reducing process design and implementation time.

References

- [1] Grewal S., Tran P., Bhaskare A.: *Assembly Planning Software*, Annals of the CIRP, 1995, Vol. 44, No. 1.
- [2] Kanai S., Takahashi H., Makino H.: *ASPEN: Computer-Aided Assembly Sequence Planning and Evaluation System Based on Predetermined Time Standard*, Annals of the CIRP, 1996, Vol. 45, No. 1.
- [3] Homem De Mello L., Lee S.: *Computer-Aided Mechanical Assembly Planning*, Kluwert Academic Publishers, Boston, 1991.
- [4] *Guru, Integrated Components Manual*, MDDBS, Inc., West Lafayette.
- [5] Reifur B.: *Expert System Aided Selection of Gripping Device for Assembly Process* (in Polish), MANUFACTURING'01, Poznań, 2001
- [6] Mulawka J.: *Expert Systems* (in Polish), WNT, Warsaw, 1996.
- [7] Niederliński A.: *Rule-Oriented Expert Systems* (in Polish), Wydawnictwo Pracowni Komputerowej Jacka Skalmierskiego, Gliwice, 2000.
- [8] Duch W.: *Neural Networks* (in Polish), Akademicka Oficyna Wydawnicza, Warsaw, 2000.
- [9] Schunk Gripper Catalogue: *Spann und Greiftechnik*.

Wybór wyposażenia montażowego za pomocą systemu ekspertowego

Projektowanie procesu technologicznego montażu oraz dobór właściwego oprzyrządowania jest działaniem wieloetapowym, mającym podstawowy wpływ na jakość oraz cenę wytwarzanych urządzeń. Wiedza i doświadczenie konstruktora są jednymi z czynników umożliwiających jakościowe i ilościowe wspomaganie procesu projektowania. Umożliwiają one wspomaganie procesu podejmowania decyzji na różnych etapach projektowania. Rozproszenie, trudny dostęp i złożona struktura rozpatrywanej wiedzy ograniczają w znacznym stopniu jej dostępność. W tym kontekście coraz większego znaczenia nabiera efektywne planowanie i dobór odpowiednich urządzeń montażowych wspomaganych przez systemy doradcze. Jeśli uwzględnić wykorzystanie wiedzy proceduralnej zawartej w narzędziach programowych, wiedzę katalogową zawartą w bazach danych oraz wiedzę ekspercką zawartą w bazach wiedzy, to konieczne staje się wykorzystanie efektywnego narzędzia obejmującego metodykę poszukiwania rozwiązania, dobór kryteriów i ograniczeń, określenie poszukiwanych wielkości oraz ich wartości lub kierunków ich zmian. W artykule przedstawiono budowę takiego systemu oraz wyniki doboru urządzeń typu robot i chwytak dla określonego zespołu zaworu.



Spectral response of linear system under Poisson driven pulses

MALGORZATA GŁADYSZ, PAWEŁ ŚNIADY

Wrocław University of Technology, Wybrzeże Wyspiańskiego 27, 50-370 Wrocław

In this paper, the dynamic response of a linear structure to a random train of pulses driven by a Poisson process is considered. An analytical method is developed to determine spectral density function of the response of the structure. Both stationary and non-stationary vibration problems are considered. To assume simple algebraic relations for both cases of response the dynamic influence function has been introduced.

Keywords: *structure, train of pulses, spectral analysis*

1. Introduction

Analysis of the response of vibratory systems to random train of pulses has received a great deal of attention in the past [1–6]. The shapes of the pulses have been assumed to be the Dirac delta function [1, 3, 11] or arbitrary function and have deterministic or random time duration. The response of a structure subjected to a random train of pulses is, in general case, a point stochastic filtering process and in particular a Poisson filtering process [2, 4, 5, 6]. This latter case occurs in the dynamics of highway bridges loaded with a vehicular traffic flow [9, 10]. A random train of pulses can model seismic, para-seismic, acoustic excitations and wind load [11].

In this paper, the dynamic response of a linear structure to a random train of pulses is considered. An analytical technique is developed to determine spectral density function of the response of the system.

Many random vibration problems are solved using the spectral analysis method. This method is applicable only to linear time-invariant system [7, 8]. Both stationary and non-stationary vibration problems are considered. There are two reasons why the spectral analysis method is used: the simplicity of the method and the fact that the spectral density function of the vibration system reflects the energy distribution in the frequency domain. The frequency domain method is particularly suited to the analysis of stationary responses of a linear system. It can also be applied to determine non-stationary responses. For stationary responses there exists a simple algebraic relation between the input and the output spectrum. When the linear system is excited by a random train of the pulses driven by a Poisson process there is no such a simple algebraic relation between the input and the output spectrum. To overcome these difficulties the dynamic influence function has been introduced which allows us to assume also simple algebraic relation for stationary and non-stationary responses.

2. Spectral density function of pulses train

At the beginning let us consider a time-invariant linear system subjected to the stochastic excitation $f(t)$. With the normal mode approach, the motion of a linearly elastic structure can be described by the set of uncoupled equations:

$$\ddot{y}_n(t) + 2\alpha_n \dot{y}_n(t) + \omega_n^2 y_n(t) = p_n f(t), \quad n = 1, 2, \dots, \quad (1)$$

where dots denote differentiation with respect to time.

The covariance function of the structure response to excitation $f(t)$ and its spectral density function require the knowledge of the spectral density function of that excitation. Let the function $f(t)$ be a stochastic process, stationary in the extensive meaning with the random characteristics $E[f(t)]$, $C_{ff}(t_2 - t_1) = C_{ff}f(t)$.

This stochastic process is assumed to be a train of pulses with random amplitudes occurring at random times. The process has the form of the following superposition:

$$f(t) = \sum_{k=1}^{N(t)} A_k S(t, t_k, T_k). \quad (2)$$

The amplitudes A_k of pulses composing the random train inducing vibrations of the structure, the times t_k of the pulses activation and the times T_k of their duration are, in general, random variables. It is assumed here that the amplitudes are mutually independent, random variables and their random characteristics are known and constant:

$$E[A_k] = E[A], \quad E[A_k^2] = E[A^2].$$

It is assumed also that the duration time of any pulse is the same, so $T_k = T_0$ for $k = 1, 2, 3, \dots$

The function $S(t, t_k, T_k) = S(t, t_k, T_0)$ in expression (2) describes the shape of the k^{th} pulse in the time interval $(t_k, t_k + T_0)$. Here it is assumed that the shape of each pulse does not depend on the arrival time t_k , but depends on the time distance between the observation and the arrival of the k^{th} pulse. So in this case the function $S(t, t_k, T_0) = S(t - t_k)$ has a form:

$$S(t - t_k, T_0) = \begin{cases} S(t - t_k) & \text{for } t_k \leq t \leq t_k + T_0, \\ 0 & \text{for } t < t_k \text{ or } t > t_k + T_0. \end{cases} \quad (3)$$

In the next section, some selected examples of the shape function of the pulses (Figure 1) are considered.

The symbol $N(t)$ in the sum (2) denotes the Poisson process with parameter λ that gives the number of pulses in the time interval $(0, t)$.

The excitation function $f(t)$ is a sum of the pulses loading the structure during observation. Taking into account the characteristics of the Poisson process the function $f(t)$ can be described as:

$$f(t) = \int_0^t A(\tau)S(t-\tau)dN(\tau). \quad (4)$$

The symbol $dN(\tau)$ denotes increment of the process $N(t)$ in the time interval $(\tau, \tau+d\tau)$

The general relationships between the covariance function $C_{xx}(\tau)$ and the spectral density function $\Phi_{xx}(\omega)$ for any stationary stochastic process $X(t)$ take the form:

$$\Phi_{xx}(\omega) = \frac{1}{2\pi} \int_{-\infty}^{\infty} C_{xx}(\tau)e^{-i\omega\tau} d\tau = \frac{1}{\pi} \int_0^{\infty} C_{xx}(\tau) \cos \omega\tau d\tau, \quad (5)$$

$$C_{xx}(\tau) = \int_{-\infty}^{\infty} \Phi_{xx}(\omega)e^{i\omega\tau} d\omega = 2 \int_0^{\infty} \Phi_{xx}(\omega) \cos \omega\tau d\omega.$$

Taking into account the assumptions presented earlier and accepted for the excitation $f(t)$ its covariance function can be described as:

$$\begin{aligned} C_{ff}(t_1, t_2) &= \int_{\max(t_1, t_2) - T_0}^{\min(t_1, t_2)} E[A^2(\tau)] E[S(t_1 - \tau)S(t_2 - \tau)] \lambda(\tau) d\tau \\ &= E[A^2] \lambda \int_{\max(t_1, t_2) - T_0}^{\min(t_1, t_2)} E[S(t_1 - \tau)S(t_2 - \tau)] d\tau, \end{aligned} \quad (6)$$

where $t_1 \geq T_0, t_2 \geq T_0$.

For deterministic functions $S(t-t_k)$ and the stationary excitation processes Equation (6) takes the form:

$$\begin{aligned} C_{ff}(t_1, t_2) &= C_{ff}(t) = E[A^2] \lambda \int_{\max(t_1, t_2) - T_0}^{\min(t_1, t_2)} S(t_1 - \tau)S(t_2 - \tau) d\tau \\ &= E[A^2] \lambda \int_0^{T_0 - |t|} S(T_0 - |t| - \tau)S(T_0 - \tau) d\tau \quad \text{for } |t| < T_0, \end{aligned} \quad (7)$$

where $|t| = |t_1 - t_2|$ and $C_{ff}(t) = 0$ for $|t| \geq T_0$.

The spectral density function of $f(t)$, after application of (5), can be obtained from the expression:

$$\Phi_{ff}(\omega) = \frac{1}{2\pi} \int_{-\infty}^{\infty} C_{ff}(\eta) e^{-i\omega\eta} d\eta = \frac{1}{\pi} \int_0^{\infty} C_{ff}(\eta) \cos \omega\eta d\eta. \quad (8)$$

The spectral density functions for some particular forms of excitation can be described by the following equations.

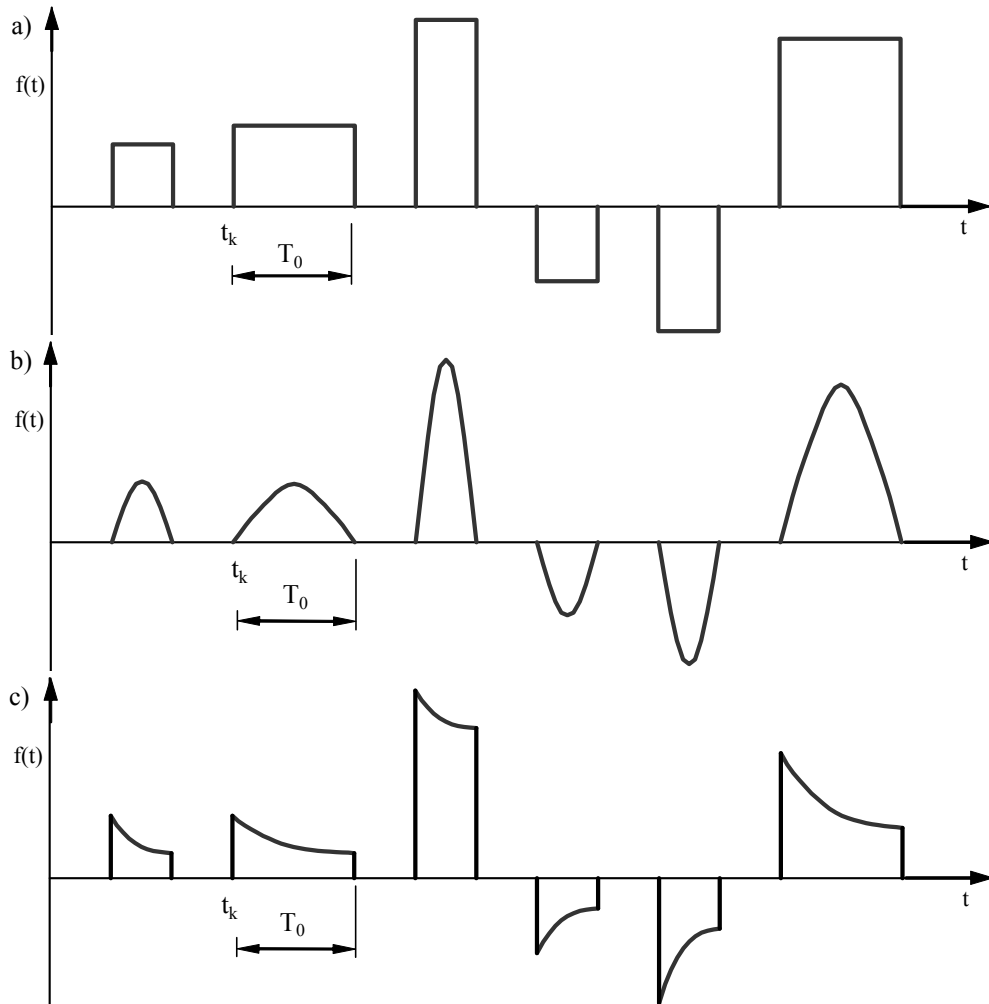


Fig. 1. Shape function of the pulses: a) rectangular, b) sinusoidal, c) exponential

1. When the structure is loaded with the stream of the rectangular pulses (Figure 1a) the function $S(t-t_k)$ takes the form:

$$S(t-t_k) = \begin{cases} 1 & \text{for } t_k \leq t \leq t_k + T_0, \\ 0 & \text{for } t < t_k \text{ or } t > t_k + T_0 \end{cases} \quad (9)$$

and the spectral density function of impulses and their covariance function can be described as (Figure 2):

$$\Phi_{ff}(\omega) = \frac{2E[A^2]\lambda}{\pi} \frac{1}{\omega} (1 - \cos \omega T_0), \quad (10)$$

$$C_{ff}(t) = E[A^2]\lambda(T_0 - |t|). \quad (11)$$

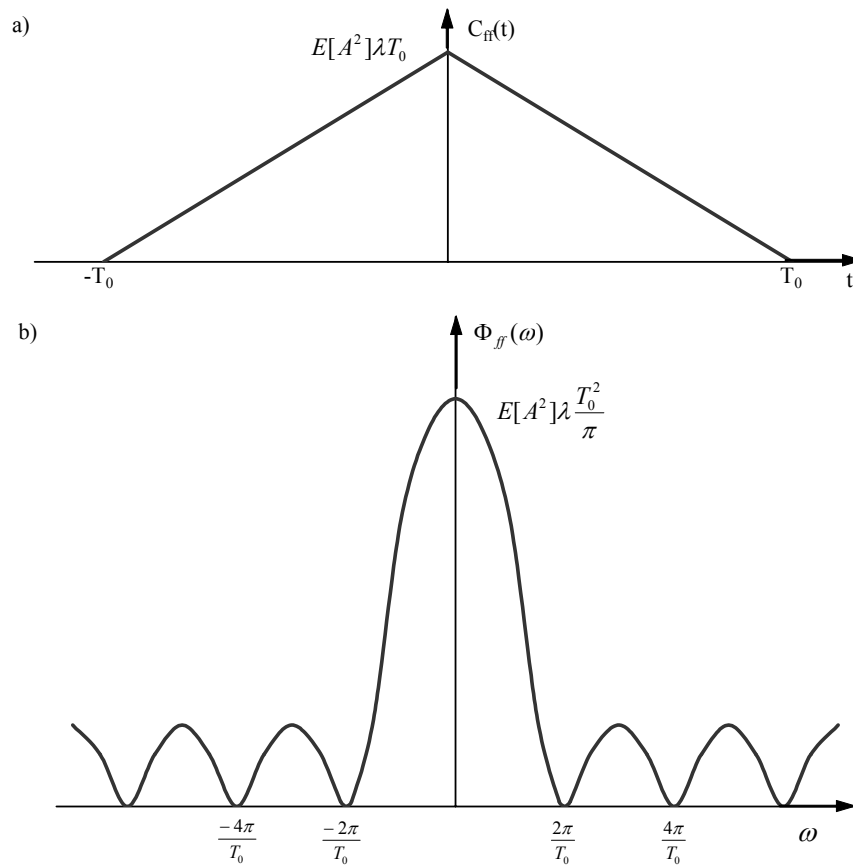


Fig. 2. Spectral density function (a) and covariance function (b) for rectangular pulses

2. In the case of the structure excited by a series of sinusoidal pulses (Figure 1b):

$$S(t-t_k) = \begin{cases} \sin p(t-t_k), & \text{where } p = \frac{\pi}{T_0}, \quad \text{for } t_k \leq t \leq t_k + T_0, \\ 0 & \text{for } t < t_k \text{ or } t > t_k + T_0, \end{cases} \quad (12)$$

the spectral density function of impulses and their covariance function take the form (Figure 3):

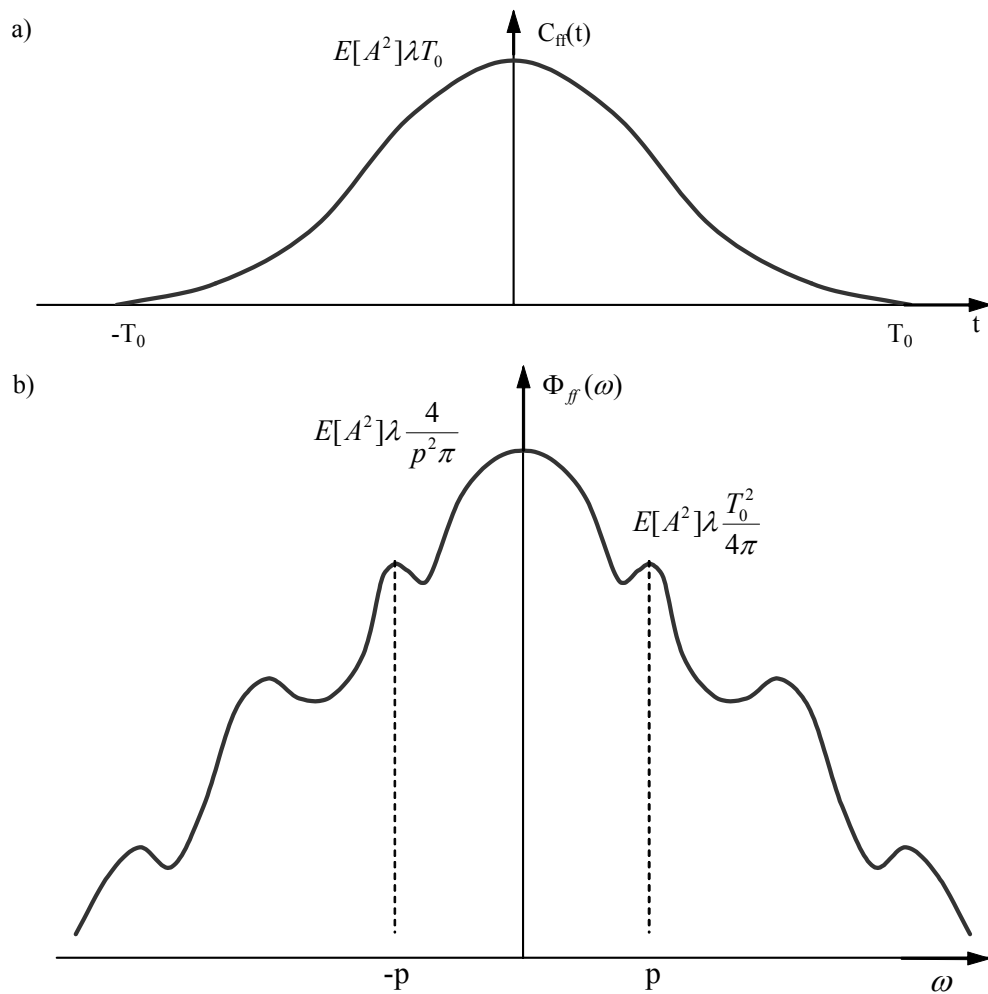


Fig. 3. Spectral density function (a) and covariance function (b) for sinusoidal pulses

$$\Phi_{ff}(\omega) = \frac{2E[A^2]\lambda}{\pi} \frac{p^2}{(p-\omega)^2(p+\omega)^2} (1 + \cos \omega T_0), \quad (13)$$

$$C_{ff}(t) = E[A^2]\lambda \frac{1}{2} \left[\frac{1}{p} \sin p|t| + (T_0 - |t|) \cos p|t| \right]. \quad (14)$$

3. For the series of exponential pulses (Figure 1c) the functions discussed are described by (Figure 4):

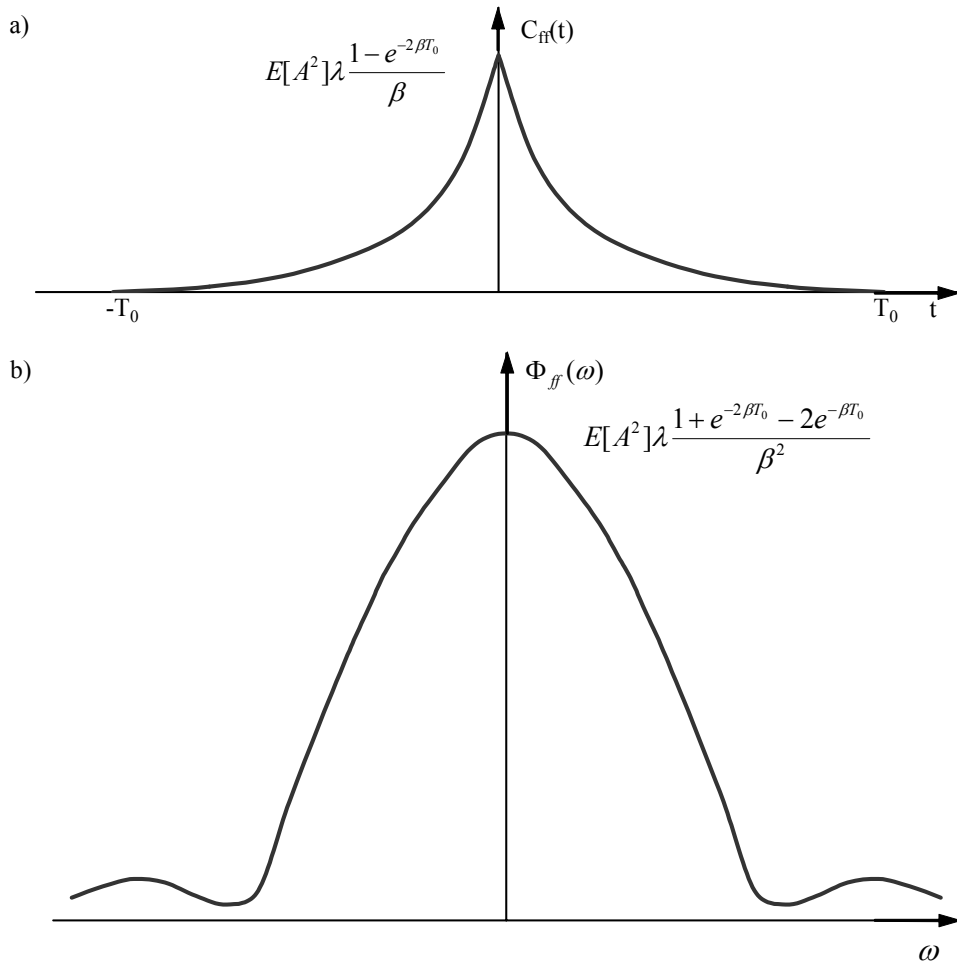


Fig. 4. Spectral density function (a) and covariance function (b) for exponential pulses

$$S(t-t_k) = \begin{cases} e^{-\beta(t-t_k)} & \text{for } t_k \leq t \leq t_k + T_0, \\ 0 & \text{for } t < t_k \text{ or } t > t_k + T_0, \end{cases} \quad (15)$$

$$\Phi_{ff}(\omega) = \frac{E[A^2]\lambda}{\pi} \frac{1}{(\omega^2 + \beta^2)} \left[1 + e^{-2\beta T_0} - 2e^{-\beta T_0} \cos \omega T_0 \right], \quad (16)$$

$$C_{ff}(t) = E[A^2]\lambda \frac{1}{2\beta} \left[e^{-\beta|t|} - e^{\beta(|t|-2T_0)} \right]. \quad (17)$$

3. Spectral analysis of the dynamic system

The frequency domain method is particularly suited to the analysis of stationary responses of a linear dynamic system (1). It can also be applied to determine non-stationary responses [12]. For stationary responses there exists simple algebraic relation between the input and the output spectra [7, 8]. When the linear system is excited by a random train of pulses driven by a Poisson process there is no such a simple algebraic relation between the input and the output spectra. To overcome this difficulty the dynamic influence function has been introduced, which allows us to assume also a simple algebraic relationship.

3.1. Stationary response of linear system

Let us consider a structure subjected to a weakly stationary stochastic excitation $f(t)$. The steady-state solution of Equation (1) is similar to the solution of the case where an excitation is a weakly stationary process. Assuming that the spectral density function $\Phi_{ff}(\omega)$ of excitation process $f(t)$ is known, the spectral density function of the response $\Phi_{y_n y_n}(\omega)$ is described by relation [7, 8]:

$$\Phi_{y_n y_n}(\omega) = H_n(\omega) H_n^*(\omega) \Phi_{ff}(\omega), \quad (18)$$

where an asterisk denotes the complex conjugate.

The complex frequency response function $H_n(\omega)$ is connected with the impulse response function $h_n(t)$ by equation:

$$H_n(\omega) = \int_0^{\infty} h_n(t) e^{-i\omega t} dt = \frac{P_n}{\omega_n^2 - \omega^2 + 2i\alpha_n \omega}, \quad (19)$$

where the symbol $i = \sqrt{-1}$ is the imaginary unit.

Equation (18) relates the input and the output spectral density functions through a simple algebraic relationship.

Let us now consider the response of the system (1) excited by the random train of the pulses driven by a Poisson process. The steady-state solution of Equation (1) in which the excitation process is described by relation (2) can be obtained in the form of a Stieltjes stochastic integral with respect to the Poisson process $N(t)$ as [4]:

$$y_n(t) = \int_{-\infty}^t \int_{\tau}^{\eta} A(\tau) h_n(t - \xi) S(\xi - \tau) d\xi dN(\tau), \quad (20)$$

where $h_n(t - \tau) = \Omega_n^{-1} \exp[-\alpha_n(t - \xi)] \sin \Omega_n(t - \xi)$ is the impulse response function, and $\Omega_n^2 = \omega_n^2 - \alpha_n^2$ is the damped natural frequency.

Let us assume that the random variables $A(\tau)$ are also independent of the Poisson process $N(t)$. The covariance function $C_{y_n y_n}(t_1, t_2)$ of the response has the form [4]:

$$C_{y_n y_n}(t_1, t_2) = E[A^2] \lambda \int_{-\infty}^t \int_{\tau}^{\eta_1} \int_{\tau}^{\eta_2} h_n(t_1 - \xi_1) h_n(t_2 - \xi_2) S(\xi_1 - \tau) S(\xi_2 - \tau) d\xi_1 d\xi_2 d\tau, \quad (21)$$

where $t = \min(t_1, t_2)$ and the symbol $E[\bullet]$ means the expected value.

From relation (21) it is difficult to obtain the general formulae for spectral density function similar to Equation (18). To overcome this difficulty let us introduce the dynamic influence function $G_n(t - \tau)$ which is the structure normal mode response at the time t to the pulse $S(t - \tau)$. The function $G_n(t - \tau)$ can be obtained from the integral:

$$G_n(t - \tau) = \begin{cases} G_n^{(1)}(t - \tau) = p_n \int_{\tau}^t h_n(t - \xi) S(\xi - \tau) d\xi & \text{for } t - T_0 \leq \tau \leq t, \\ G_n^{(2)}(t - \tau) = p_n \int_{\tau}^{\tau+T} h_n(t - \xi) S(\xi - \tau) d\xi & \text{for } 0 \leq \tau \leq t - T_0. \end{cases} \quad (22)$$

The covariance function for steady-state response of the system assumes the form:

$$\begin{aligned} C_{y_n y_n}(t_1, t_2) &= E[A^2] \lambda \int_{-\infty}^t G_n(t_1 - \tau) G_n(t_2 - \tau) d\tau = E[A^2] \lambda \int_0^{\infty} G_n(\xi) G_n(t_2 - t_1 + \xi) d\xi \\ &= C_{y_n y_n}(t_2 - t_1) = C_{y_n y_n}(t), \end{aligned} \quad (23)$$

where $t = t_2 - t_1$.

Equation (23) can be presented in the form:

$$\begin{aligned} C_{y_n y_n}(t) &= E[A^2] \lambda \int_{-\infty}^{t_1} \int_{-\infty}^{t_2} G_n(t_1 - \xi_1) G_n(t_2 - \xi_2) \delta(\xi_1 - \xi_2) d\xi_1 d\xi_2 \\ &= E[A^2] \lambda \int_0^{\infty} \int_0^{\infty} G_n(\eta_1) G_n(\eta_2) \delta(t + \eta_2 - \eta_1) d\eta_1 d\eta_2, \end{aligned} \quad (24)$$

where $\delta(t)$ denotes the Dirac delta function.

Relation (24) can be used to find the spectral density function $\Phi_{y_n y_n}(\omega)$ of the response $y_n(t)$. Taking into account Equation (24) and the relationship between the covariance function and the spectral density function (5) we obtain:

$$\begin{aligned} \Phi_{y_n y_n}(\omega) &= \frac{1}{2\pi} \int_{-\infty}^{\infty} C_{y_n y_n}(t) e^{-i\omega t} dt \\ &= \frac{1}{2\pi} E[A^2] \lambda \int_{-\infty}^{\infty} \int_0^{\infty} \int_0^{\infty} G_n(\eta_1) G_n(\eta_2) \delta(t + \eta_2 - \eta_1) e^{-i\omega t} d\eta_1 d\eta_2 dt \\ &= \frac{1}{2\pi} E[A^2] \lambda \int_0^{\infty} G_n(\eta_1) e^{-i\omega \eta_1} d\eta_1 \cdot \int_0^{\infty} G_n(\eta_2) e^{i\omega \eta_2} d\eta_2 \cdot \int_{-\infty}^{\infty} e^{-i\omega t} \delta(t) dt. \end{aligned} \quad (25)$$

Expression (25) can be presented in the short form which is similar to (18):

$$\Phi_{y_n y_n}(\omega) = \frac{E[A^2] \lambda}{2\pi} J_n(\omega) \cdot J_n^*(\omega). \quad (26)$$

The frequency influence function $J_n(\omega)$ has the form:

$$J_n(\omega) = \int_0^{\infty} G_n(\eta) e^{-i\omega \eta} d\eta = \int_0^{T_0} G_n^{(1)}(\eta) e^{-i\omega \eta} d\eta + \int_{T_0}^{\infty} G_n^{(2)}(\eta) e^{-i\omega \eta} d\eta, \quad (27)$$

and an asterisk denotes complex conjugate.

Relationship (27) can be also presented in the form:

$$J_n(\omega) = p_n \int_0^{T_0} e^{-i\omega \eta} \left(\int_0^{\eta} h_n(\eta - \xi) S(\xi) d\xi \right) d\eta + p_n \int_{T_0}^{\infty} e^{-i\omega \eta} \left(\int_0^{T_0} h_n(\eta - \xi) S(\xi) d\xi \right) d\eta. \quad (28)$$

3.2. Non-stationary response of linear system

Let us consider now non-stationary vibrations of the system. The response of the system and its covariance function assume, respectively, the form:

$$y_n(t) = \int_0^t A(\tau) G_n(t - \tau) dN(\tau) \quad (29)$$

and

$$\begin{aligned} C_{y_n y_n}(t_1, t_2) &= E[A^2] \lambda \int_0^t G_n(t_1 - \tau) G_n(t_2 - \tau) d\tau \\ &= E[A^2] \lambda \int_0^{t_1} \int_0^{t_2} G_n(t_1 - \tau_1) G_n(t_2 - \tau_2) \delta(\tau_1 - \tau_2) d\tau_1 d\tau_2, \end{aligned} \quad (30)$$

where $t = \min(t_1, t_2)$.

We extend the spectral analysis presented above for stationary vibrations to non-stationary response of the system using evolutionary spectral density method proposed by Priestley [12]. The non-stationary stochastic process $f(t)$ can be presented in the form:

$$f(t) = \int_{-\infty}^{\infty} A(t, \omega) e^{i\omega t} dX(\omega), \quad (31)$$

where $dX(\omega)$ is an orthogonal increment of the stationary process $X(\omega)$:

$$E[dX(\omega) dX^*(\omega)] = \begin{cases} \Phi_{XX}(\omega) d\omega & \text{for } \omega_1 = \omega_2 = \omega, \\ 0 & \text{for } \omega_1 \neq \omega, \end{cases} \quad (32)$$

where the asterisk denotes complex conjugate.

The covariance function of the non-stationary process $f(t)$ can be presented in the form [12]:

$$C_{ff}(t_1, t_2) = \int_{-\infty}^{\infty} a(t_1, \omega) a^*(t_2, \omega) \Phi_{XX}(\omega) e^{i\omega(t_1 - t_2)} d\omega. \quad (33)$$

The product $\Psi_{ff}(t, \omega) = |a(t, \omega)|^2 \Phi_{XX}(\omega)$ is known as the evolutionary spectral density. Let us find the evolutionary spectral density function for the response of the system given by Equation (29). From Equation (30) we have:

$$\begin{aligned} C_{y_n y_n}(t_1, t_2) &= E[A^2] \lambda \int_{-\infty}^{\infty} \int_0^{t_1} \int_0^{t_2} G_n(t_1 - \tau_1) h_n(t_2 - \tau_2) e^{i\omega(\tau_1 - \tau_2)} d\tau_1 d\tau_2 d\omega \\ &= E[A^2] \lambda \int_{-\infty}^{\infty} \left[\int_0^{t_1} G_n(\xi_1) e^{-i\omega \xi_1} d\xi_1 \cdot \int_0^{t_2} G_n(\xi_2) e^{-i\omega \xi_2} d\xi_2 \right] e^{i\omega(t_1 - t_2)} d\omega. \end{aligned} \quad (34)$$

In the above case, the evolutionary spectral density function takes the form:

$$\Psi_{y_n y_n}(t, \omega) = E[A^2] \lambda a_n(t, \omega) a_n^*(t, \omega), \quad (35)$$

where:

$$a_n(t, \omega) = \int_0^t G_n(\xi) e^{-i\omega \xi} d\xi. \quad (36)$$

Taking into account that the dynamic influence function has two different forms (22), expression (36) can be presented as follows:

$$a_n(t, \omega) = \begin{cases} \int_0^t G_n^{(1)}(\xi) e^{-i\omega \xi} d\xi & \text{for } 0 \leq t \leq T_0, \\ \int_0^{T_0} G_n^{(1)}(\xi) e^{-i\omega \xi} d\xi + \int_{T_0}^t G_n^{(2)}(\xi) e^{-i\omega \xi} d\xi & \text{for } t > T_0. \end{cases} \quad (37)$$

4. The numerical examples

Let us consider the case where the structure is loaded with the stream of rectangular pulses (Figure 1a). The shape functions of pulses, their spectral density function and covariance function are described by relationships (9), (10) and (11). In this special case of the load, function (27) takes the form:

$$J_n(\omega) = \frac{1}{\omega_n^2} (1 - e^{-i\omega T_{01}}) \left[\frac{1}{i\omega} - \frac{2\alpha_n + i\omega}{(\alpha_n + i\omega)^2 + \Omega_n^2} \right], \quad (38)$$

where $\Omega_n^2 = \omega_n^2 - \alpha_n^2$.

The spectral density function of the response $y_n(t)$ (26) is described by the following expression:

$$\Phi_{y_n y_n}(\omega) = \frac{E[A^2]\lambda}{2\pi} \frac{1}{\omega_n^4} (2 - 2\cos\omega T_0) \left[\frac{1}{\omega^2} + \frac{\omega^2 - 4\alpha_n^2}{(\omega_n^2 - \omega^2)^2 + 4\alpha_n^2 \omega^2} \right]. \quad (39)$$

Figures 5, 6, 7 and 8 show the graphs of function (39) dependent on the excitation frequency ω ($\omega = 0, 0.5, 1, \dots, 30$ Hz). The results are presented for the natural frequency $\omega_n = 5$ Hz and the damping ratio $\xi = 0.02$, where $\xi = \alpha_n \omega_n^{-1}$. The quantity T_0 is the duration time of a single pulse and $T_0 = \eta T_n$, where $T_n = 2\pi\omega_n^{-1}$. It is assumed here that the coefficient η has a value in turn on the graphs: $\eta = 0.2, 0.5, 1.0$ and 2.0 . We can observe that spectral density function (39) has clear peaks near $\omega = \omega_n$ if $\eta < 1$ and the distribution of function (39) becomes more mild for $\eta = 1.0$ or 2.0 . Also

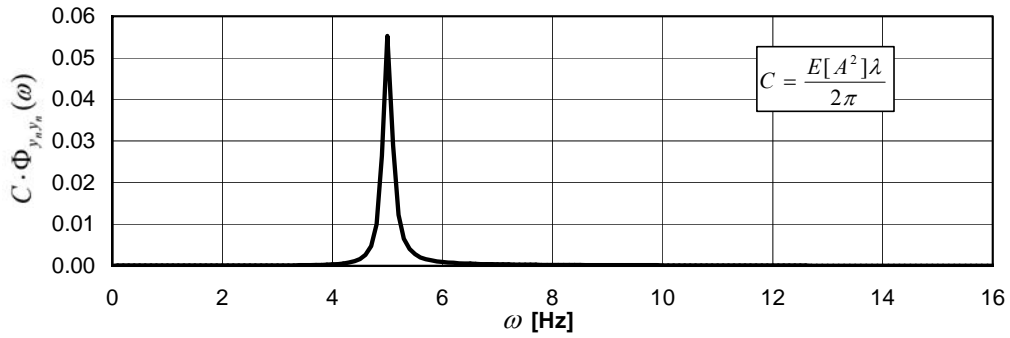


Fig. 5. The spectral density function for $\eta = 0.2$ and $\omega_n = 5$ Hz

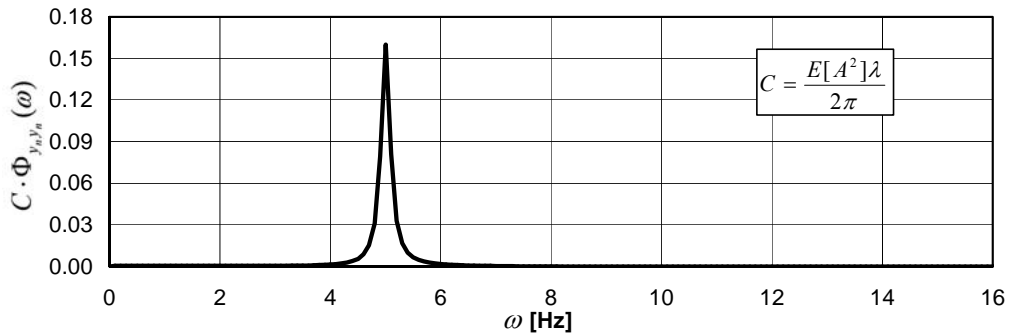
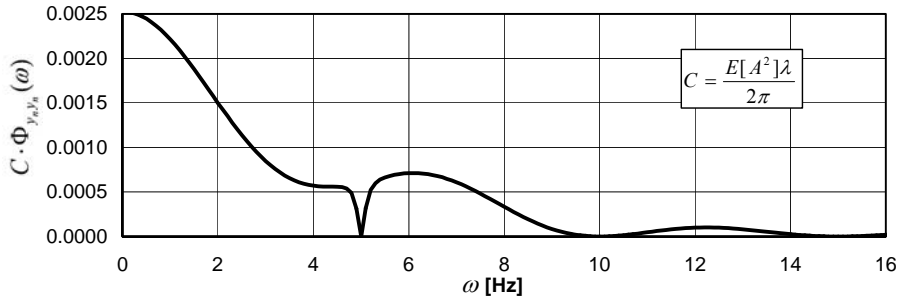
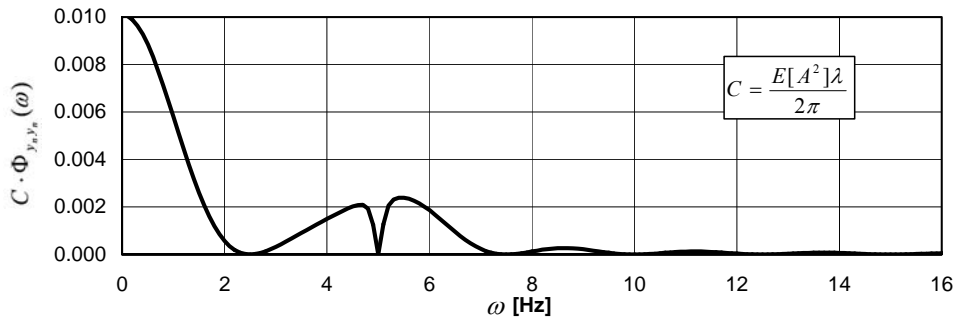
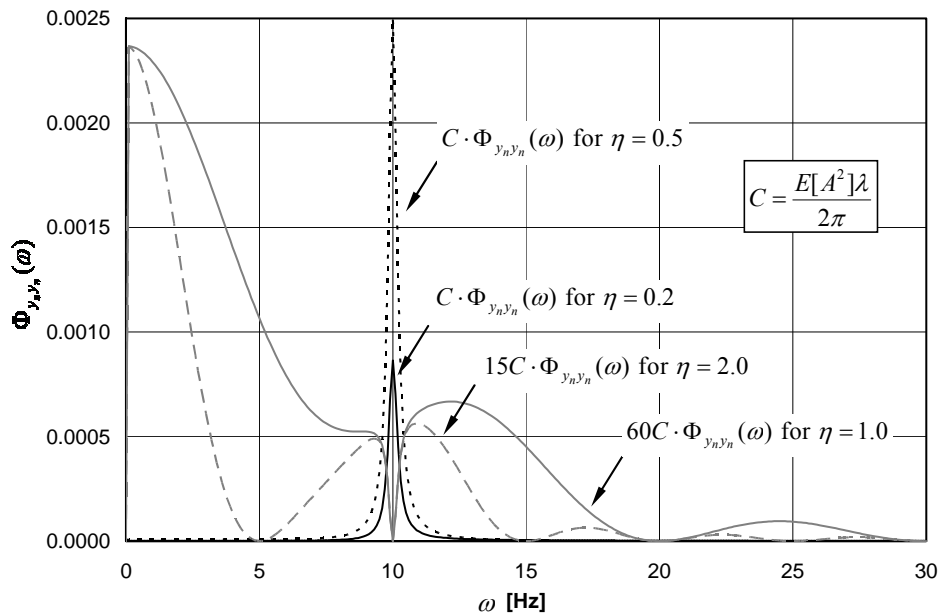


Fig. 6. The spectral density function for $\eta = 0.5$ and $\omega_n = 5$ Hz

Fig. 7. The spectral density function for $\eta = 1.0$ and $\omega_n = 5$ HzFig. 8. The spectral density function for $\eta = 2.0$ and $\omega_n = 5$ HzFig. 9. The spectral density functions for $\eta = 0.2, 0.5, 1.0, 2.0$ and $\omega_n = 10$ Hz

for another values of ω_n (e.g. $\omega_n = 10$ Hz in Figure 9) the spectrum of function (39) reveals sharp peaks for $\omega = \omega_n$ and centres around this value. Similar graphs were presented in [6] for variance of the normal mode dependent on duration of the pulses T_0 . We can also notice that for the duration of the pulse equal to $T_0 = 0.5T_n = \pi\omega_n^{-1}$ the response of the system is the most narrow-band process.

5. Conclusions

The spectral analysis method is suited to the analysis of stationary responses of a linear dynamic system. Dynamic response of linear system under random train of pulses driven by a Poisson process constitutes a filtered Poisson process. In this case, the spectral analysis of the response of linear system cannot be obtained using the complex frequency response function (18). To overcome this difficulty the dynamic influence function and the frequency influence function have been introduced. Taking advantage of these both functions also in the case of non-stationary responses we can arrive at a simple algebraic relation between the input and the output spectrum.

The relationship describing the spectral density function has the simple form (26) easy to use in the numerical analysis.

References

- [1] Roberts J.B.: *The response of linear vibratory systems to random impulses*, Journal of Sound and Vibration, 1965, 2, 375–390.
- [2] Lin Y.K., Cai G.Q.: *Probabilistic Structural Dynamics, Advanced Theory and Applications*, 1995, McGraw Hill Inter Editions.
- [3] Srinivasan S.K., Subramanian R., Kumaroswamy S.K.: *Response of linear vibratory systems to non-stationary stochastic impulses*, Journal of Sound and Vibration, 1967, 6, 169–179.
- [4] Śniady P.: *Dynamic response of linear structures to a random stream of pulses*, Journal of Sound and Vibration, 1989, 131 (1), 91–102.
- [5] Gładysz M., Śniady P.: *Random vibrations of a discrete system under a series of loads constituting a Poisson process* (in Polish), Archiwum Inżynierii Łądowej, 1984, XXX, (1), 37–51.
- [6] Mazur-Śniady K., Śniady P.: *Dynamic response of linear structures to random streams of arbitrary impulses in time and space*, Journal of Sound and Vibration, 1986, 110, 59–68.
- [7] Soong T.T., Grigoriu M.: *Random Vibration of Mechanical and Structural Systems*, 1993, PTR Prentice-Hall, Inc.
- [8] Śniady P.: *Podstawy stochastycznej dynamiki konstrukcji* (in Polish), 2000, Oficyna Wydawnicza Politechniki Wrocławskiej.
- [9] Tung C.C.: *Random response of highway bridges to vehicle loads*, Journal of Engineering Mechanical Division, 1967, 93 (EMS), 73–94.

- [10] Sieniawska R., Śniady P.: *Life expectancy of highway bridges due to traffic load*, Journal of Sound and Vibration, 1990, 140 (1), 31–38.
- [11] Verne-Jones D.: *Stochastic models for earthquake occurrence*, Journal of The Royal Statistical Society, 1970, series B 32, 1–62.
- [12] Priestley M.B.: *Power spectral analysis of non-stationary random process*, Journal of Sound and Vibration, 1967, 6, 86–97.

Gęstość widmowa odpowiedzi układu liniowego obciążonego serią impulsów

Zaprezentowano analizę widmową odpowiedzi układu liniowego obciążonego losową serią impulsów tworzących proces Poissona. Przedstawiono związki opisujące funkcję gęstości widmowej i kowariancję dla różnych funkcji kształtu impulsów. Praca zawiera ogólne rozwiązania dla funkcji gęstości widmowej w przypadku stacjonarnych i niestacjonarnych drgań układu w postaci związków o prostej budowie, które można wykorzystać w analizie numerycznej.



Stability analysis of cylindrical composite shells in MSC/Nastran

I. KREJA

Gdańsk University of Technology, Gabriela Narutowicza 11/12, 80-952 Gdańsk, Poland

In the paper, the capabilities of the *MSC/NASTRAN* system in the field of stability analysis of composite laminated shells are critically tested. Two selected benchmark examples of laminated cylindrical panels under axial compression are examined. The *MSC/NASTRAN* results obtained either in buckling analysis or in nonlinear incremental calculations are compared with the solutions available in the literature.

Keywords: *composite shells, buckling, FE analysis*

1. Motivation

In the last few years, structural engineers who use commercial computer systems for FE structural analysis have considerably increased in number. Among the main advantages one can recognize the following features of a typical *big commercial FEA system*

- a convenient access to the computational module through a graphical interface of pre- and postprocessors,
- wide range of linear and nonlinear analyses offered,
- a rich library of elements available in the system.

On the other hand, every user trying to perform any non-standard calculations meets also disadvantages of a big system, to mention here just a relatively complex manual and very limited information on a theoretical background. The latter together with a lack of any access to the source code makes the user see the system as a proverbial *black box*, where all one knows is the input and the output but few really know what is happening inside.

The author shares belief that *NASTRAN* can be treated as a very typical member of the family of *big commercial FEA systems*. It happened that the author had to perform a nonlinear analysis of laminated composite shells with the *MSC/NASTRAN* system after a rather short experience with that program. According to promotional materials

1. The *MSC/NASTRAN* system is a powerful tool in the range of linear and nonlinear analyses of structures.
2. The shell element QUAD4 available in system is suitable to model laminated shells.

Trying to verify those promises the author has applied the *MSC/NASTRAN* system to recalculate several well-known benchmark examples of large deformation analysis for composite laminated shells. However, the scope of the present paper is limited to the stability analysis of laminated cylindrical panel under axial compression as shown in Figure 1. It is assumed that the curved edge *BC* is fixed, whereas the boundary conditions at the curved edge *AD* allow only a rigid translation of the whole rim along the generatrix. The boundary conditions at the straight edges *AB* and *CD* vary, depending on the example considered.

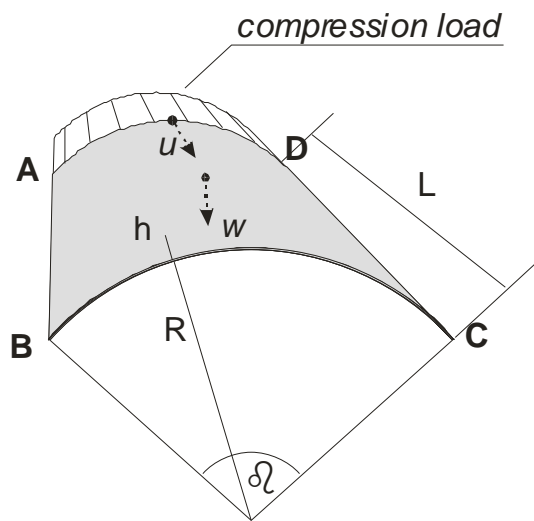


Fig. 1. Composite cylindrical panel under axial compression

One can easily notice an obvious similarity between the problem considered and the stability analysis of the isotropic cylindrical panel under axial compression being the classical illustration of the buckling problem with non-symmetric bifurcation point [1]. The basic difference herein lies in the different boundary conditions and the layered structure of the panel.

2. Computational model

2.1. Literature review

Numerical analysis of laminated plates and shells has been presented in a large number of research papers. Due to a limited space of the present report, it is impossible to list here a comprehensive bibliography of the subject. Let us focus mainly on review papers, each carrying a long list of references. At the beginning of the nineties Noor et al. published a series of articles [2, 3] presenting the state-of-the-art with re-

gard to computational models for laminated shells. Piskunov and Rasskazov [4] surveyed 180 papers to trace an evolution of theoretical models for laminated plates and shells. The list of references of the cross-sectional article by Qatu [5] contains as many as 374 positions. An extensive bibliography of the topic can be found also in the recent papers of Carrera [6, 7]. As the Finite Element Method is the predominant tool in the computational analysis of laminated shells, one may not omit here papers devoted to the review of shell finite elements [8–10].

It should be emphasized that the topic of stability analysis of cylindrical composite shells is just a fraction of the subject matter of the aforementioned papers. A review of the literature dedicated strictly to the buckling analysis of cylindrical laminated shells can be found, for example, in [11].

2.2. Basic equations in stability analysis

The first approximation to a critical load and a corresponding buckling mode can be obtained in a *linearized buckling analysis* [12]. A standard eigenvalue problem to be solved in such a case can be described by the following equation

$$[\mathbf{K}^{(\text{con})} + \lambda \mathbf{K}^{(\sigma)}] \mathbf{v} = \mathbf{0}, \quad (1)$$

where $\mathbf{K}^{(\text{con})}$ is the constitutive stiffness matrix, $\mathbf{K}^{(\sigma)}$ stands for the stress (geometrical) stiffness matrix, λ is the critical load multiplier, and \mathbf{v} symbolizes the eigenvector representing the buckling mode of the structure. One should notice that Equation (1) has been obtained with strong linearization assumptions and therefore should not be applied to examine problems with severe nonlinearities.

The second option is to trace the whole equilibrium path of the structure by means of the *nonlinear incremental analysis* [12]. Depending on the algorithm applied, such a strategy enables one to find singular points of different kind – for example adopting the arc-length technique based on the application of extended system of equations one can detect limit points as well as bifurcation points [12]. A governing equation of an incremental approach in its standard form can be written as

$$[\mathbf{K}_T({}^1\mathbf{q})] \Delta \mathbf{q} = \mathbf{R}({}^1\mathbf{q}), \quad (2)$$

$${}^2\mathbf{q} = {}^1\mathbf{q} + \Delta \mathbf{q},$$

where ${}^1\mathbf{q}$ and ${}^2\mathbf{q}$ symbolize the global vector for displacements at the actual and at the searched configuration, respectively, and $\Delta \mathbf{q}$ represents the increment of displacements. The tangential stiffness matrix $\mathbf{K}_T({}^1\mathbf{q})$ and the vector of residual forces $\mathbf{R}({}^1\mathbf{q})$ depend on the actual state of deformation.

2.3. Laminated shells analysis with Nastran

The history of Nastran is almost 40 years long, the first version of the program was designed in the course of a NASA-sponsored project which still finds its reflection in the name of the program (NASTRAN = **N**ASA **S**T**R**uctural **A**Nalysis Program). The program is available in several different releases offered simultaneously by various vendors. The most popular version of the program, the *MSC/NASTRAN for Windows* [13, 14] distributed by the MacNeal-Schwendler Corporation, has been selected for use in the present research.

According to promotional materials the MSC/NASTRAN system is *a general purpose, computer-aided engineering tool based on Finite Element Method (FEM)*. Among different finite elements available in the system one can find a 4-node shell element QUAD4 that is applicable in a structural analysis of laminated composite shells. It is quite understandable that details of the FE procedures applied are trade secrets of the MSC. One can guess that the current shell element QUAD4 originates from the shell element proposed by MacNeal in 1978 [15]. QUAD4 appeared to be one of the most effective low-order FE elements in the analysis of isotropic shells of the Mindlin–Reissner type [9, 16]. An extension of the QUAD4 element formulation to the geometrical non-linear analysis is based on the corotational concept [17]. The layered structure of the shell is considered according to the *Classical Lamination Theory*, i.e. it is assumed that the laminae are perfectly bonded together (no slip is allowed between laminae) and each lamina is in a plane stress state. According to the *First Order Shear Deformation Theory* a linear variation of deformations through the laminated thickness is postulated; however, an appropriate shear correction factor is applied to fix the error of constant transverse shear strains in contrast to the more realistic parabolic distribution. Stability analysis in *MSC/Nastran for Windows* is possible either as a *linear buckling* (see Equation (1)) or as a *nonlinear incremental analysis* (Equation (2)). The latter can be performed with application of *arc-length technique* which allows tracing quite complicated equilibrium paths; however, the details of the procedures offered are not accessible which forces users to adopt the choice of default parameters.

3. Numerical examples

3.1. Cylindrical panel No. 1 – simply supported straight edges

In the first numerical example, an axial compression of a 16-layer composite cylindrical panel is considered assuming that the straight edges AB and CD are simply supported with the possibility of moving along the generatrix. The lamination scheme can be described as $[45/-45_2/45/0_4]_S$. Each lamina is made of carbon-epoxy composite XAS-914C with the following parameters: $E_a = 130 \cdot 10^6$ kPa, $E_b = 10 \cdot 10^6$ kPa, $G_{ab} = G_{ac} = G_{bc} = 5 \cdot 10^6$ kPa and $\nu_{ab} = 0.3$. The geometry of the panel is characterized

by the height $h = 16 \times 0.125 = 2$ mm, the radius $R = 250$ mm, the length $L = 540$ mm and the opening angle $\beta = 1.6848$ rad.

The origin of this, one of the most popular buckling problems of laminated shells, is referred to the experimental and numerical study by Snell and Morley [18] which was, however, not available to the author of the present report. Jun and Hong [19] performed a nonlinear buckling analysis using 8-node degenerated shell elements within Updated Lagrangian formulation. Laschet and Jeusette [20] presented results of linear and nonlinear buckling analyses obtained with solid-shell multilayered 16-node finite elements (3 translational DOFs per node). Wagner [21] calculated the linear buckling load of the panel employing different meshes of 4-node shell elements with reduced integration and hourglass control. Brank and Carrera [22] applied 4-node mixed ANS shell elements based on the refined FSDT with finite rotations.

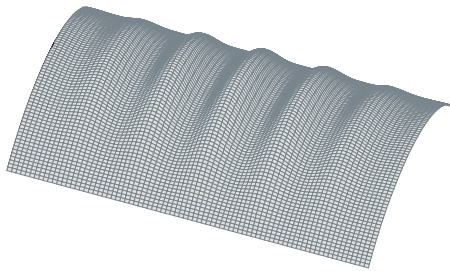
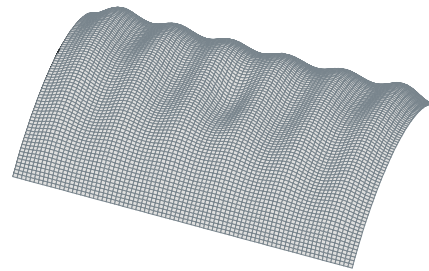
It is quite symptomatic that the descriptions of the analyzed panel given by the authors of the five papers cited above are not quite consistent. There are some differences in the interpretation of boundary conditions on the straight edges which are described as “simply supported” – for instance Jun and Hong [19] and Wagner [21] constrained only radial and circumferential translations at all nodes lying on the straight edges. However, due to the isoparametric formulation of the finite elements applied this approach does not fix the rotations about the normals to the edge. One can expect that the deformation of the panel obtained in this model largely depends on the number of nodes assumed along the straight edges. The details of the boundary conditions applied by Laschet and Jeusette [20] are not clear – just from the figure given in their paper one can expect that they applied an additional row of shell elements on both sides of the panel. Brank and Carrera [22] admitted that they themselves met some problems with the description of boundary conditions.

The MSC/Nastran has been used to compute the critical load for the examined cylindrical panel applying a linear buckling analysis as well as a non-linear incremental analysis. The calculations have been performed using uniform meshes of 20×20 , 40×40 and 80×80 QUAD4 elements. The results obtained with the MSC/Nastran are in a good agreement with reference solutions [18–21] as is shown in Table 1. The only exception is the solution of Brank and Carrera [22] which noticeably differs from all the others. The difference with respect to the experimental results is contained within the range of just several per cents. One can observe that an increase in the mesh density results in a decrease in the buckling load estimated.

As the values of the critical load estimated in the linear buckling analysis are very close to those obtained from the non-linear incremental analysis, one can conclude that the pre-buckling deformations do not differ too much from the linear solution. In these circumstances, one could expect a better agreement between the buckling mode corresponding to the first eigenvector (Figure 2) and the deformation form determined in the non-linear analysis (Figure 3).

Table 1. Buckling load for cylindrical panel with simply supported straight edges

Model	Mesh	Critical load [kN]	
		Linear buckling	Incremental analysis
8-node elements Jun & Hong [19]	8×10	–	143.2
16-node elements Laschet & Jeusette [20]	8×10	143.9	137.8
	12×18	140.3	–
4-node elements Wagner [21]	4×12	145.6	–
	4×16	142.2	–
	4×20	140.8	–
	4×40	140.0	–
	4×80	139.6	–
4-node elements Brank & Carrera [22]	32×32	–	150
QUAD4 MSC/Nastran	20×20	144.56	144.35
	40×40	141.56	142.34
	80×80	140.34	140.38
[18]	Experiment	134	

Fig. 2. The first buckling mode, $P_{\text{crit}} = 140.34$ kNFig. 3. Deformation at $P_{\text{max}t} = 140.38$ kN

3.2. Cylindrical panel No. 2 – free straight edges

A 16-layer composite cylindrical panel analysed in the second example is very similar to that considered above. The main difference lays in the boundary conditions at the straight edges AB and CD , which now remain free of any support. A buckling of such a panel made of graphite-epoxy composite AS4/3501-6 had been examined by Chaplin and Palazotto in [23]. The material parameters taken after [23] are: $E_a = 135.8 \cdot 10^6$ kPa, $E_b = 10.9 \cdot 10^6$ kPa, $G_{ab} = G_{ac} = 6.4 \cdot 10^6$ kPa, $G_{bc} = 3.2 \cdot 10^6$ kPa and $\nu_{ab} = 0.276$. A geometry of the panel is described by the following data: $h = 16 \times 0.127 = 2.032$ mm, $R = 304.8$ mm, $L = 508$ mm and $\beta = 1$ rad. The assumed layer stacking sequence is $[0/45/-45/90]_{2S}$.

Two different meshes of finite elements have been used in the computations:

- model A – 24×40 QUAD4 elements,
- model B – 48×80 QUAD4 elements.

The equilibrium paths in the geometrically non-linear analysis traced with the arc-length control technique are presented in Figure 4.

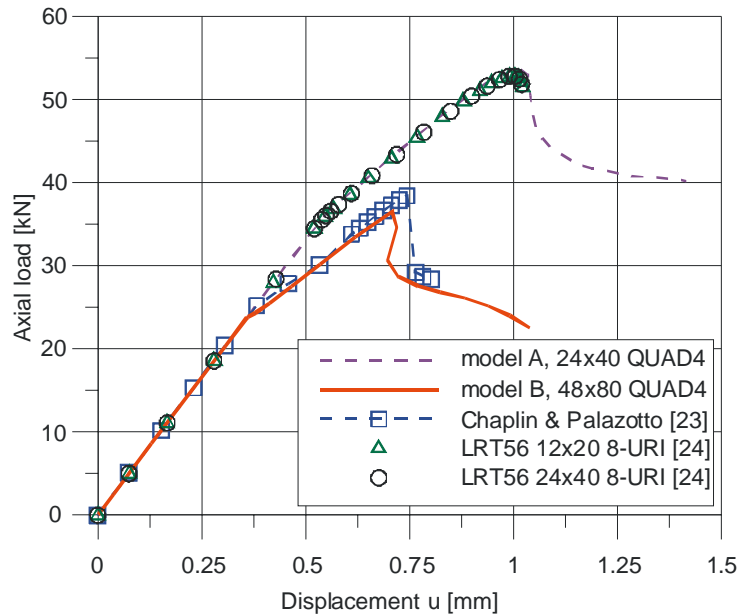


Fig. 4. Equilibrium paths for cylindrical panel No. 2

It can be observed in Figure 4 that the graph obtained for model B is very close to that given in [23]. At the first glimpse, the difference between the graphs for models A and B seems to result from the variation of the mesh density in those two models. To verify those findings additional computations have been performed with the own author's program for analysis of laminated shells SHL04 [24]. The results obtained with SHL04 for two discretizations: 12×20 and 24×40 8-node elements are almost identical with those of model A. Since on one hand the formulation incorporated in program SHL04 provides a very exact description of the geometry, and on the other hand all calculations in SHL04 are performed with a double precision, one can suppose that the different answer for model B can result from the jump between the fundamental and the post-bifurcation paths. To verify this deduction a linear buckling problem has been solved in MSC/NASTRAN for the cylindrical shell under consideration. The five lowest eigenvalues calculated for models A and B are gathered in Table 2.

Numbers presented in Table 2 show that in a case of a linear buckling analysis there are very little differences between the results for the models A and B. It is also quite characteristic that, on the contrary to the previous case of the panel No. 1, the lowest

eigenvalue computed for the panel No. 2 in the linear buckling analysis (24.4 kN) is significantly smaller than the critical load estimated in the incremental analysis (52.8 kN for model A and 36.5 kN for the model B). Looking again at the curves in Figure 4, one can observe that the distinction between the paths obtained for models A and B starts at the load level near the lowest eigenvalue determined in the linear buckling analysis (24.4 kN). This observation seems to support the opinion that the graph for model B does not represent the (fundamental) equilibrium path for an ideal structure.

Table 2. Linear buckling solution for panel No. 2

N	Eigenvalues of the buckling load [kN]	
	Model A	Model B
1	24.4326	24.3988
2	27.5549	27.4879
3	28.4660	28.4560
4	29.3149	29.3056
5	36.9095	36.8081

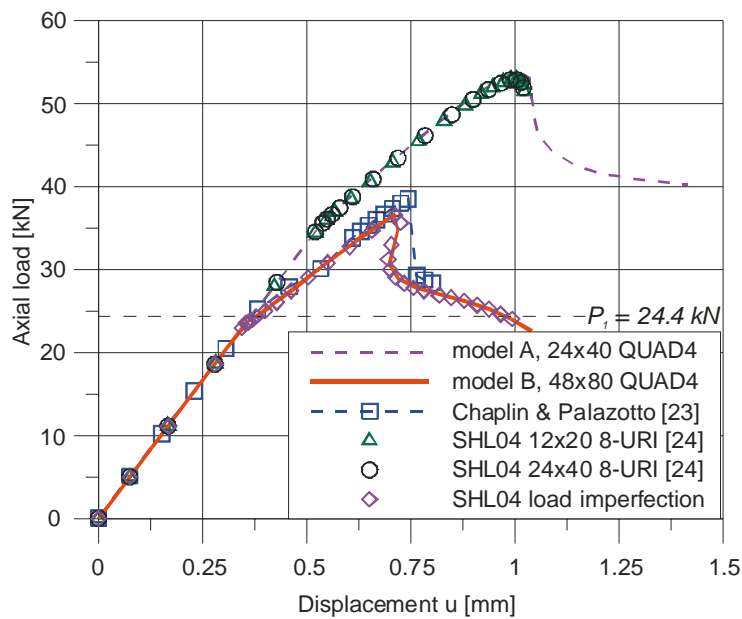


Fig. 5. Influence of imperfection in analysis of cylindrical panel No. 2

To decisively verify this suggestion additional computations have been performed with the program SHL04, where, additionally, to the axial load a very small load imperfection has been introduced taken as a transverse force acting in the middle of the

panel and equal to 0.0001 fraction of the axial load. The curve representing the imperfection case (see Figure 5) almost accurately matches the curve corresponding to model B, which, in author's opinion, entirely confirms the hypothesis that numerical round-off errors appearing in the large MSC/Nastran model B (inaccurate mapping of geometry and single precision computations) acted as a kind of imperfection which can direct a solution into the post-bifurcation path. However, on the other hand, it is important to remark that in a case that is as strongly sensitive to imperfections as the panel analysed, the results obtained for the ideal structure on no account should be used to determine the load capacity.

3. Conclusions

Capabilities of the *MSC/NASTRAN system for Windows* in the field of stability analysis of composite structures were critically tested. Two selected examples of 16-layer composite cylindrical panels under axial compression were examined with varied boundary conditions. The results obtained with *MSC/NASTRAN for Windows* were compared with the solutions available in the literature. The comparative study presented in the paper confirmed in full the power of the system to perform an advanced stability analysis of composite shells either as buckling analysis or as nonlinear incremental calculations. Additionally, it was observed that boundary conditions along the longitudinal edges significantly affect the bifurcation sensitivity of the panel. It was also shown that some numerical round-off errors can cause that the solution obtained in the *MSC/NASTRAN* jumps from a primary equilibrium path to a post-bifurcation branch.

References

- [1] Waszczyszyn Z., Cichoń C., Radwańska M.: *Stability of structures by finite element method*, Elsevier, Amsterdam, 1994.
- [2] Noor A.K., Burton W.S.: *Assessment of computational models for multilayered composite shells*, Appl. Mech. Rev., 1990, Vol. 43, 67–97.
- [3] Noor A.K., Burton W.S., Peters J.M.: *Assessment of computational models for multilayered composite cylinders*, Int. J. Solids Structures, 1991, Vol. 27, 1269–1286.
- [4] Piskunov V.G., Rasskazov A.O.: *Evolution of the theory of laminated plates and shells*, International Applied Mechanics (Plenum Publ. Corp.), 2002, Vol. 38, No. 2, 135–166.
- [5] Qatu M.S.: *Recent research advances in the dynamic behavior of shells: 1989–2000*, Part 1: *Laminated composite shells*, Appl. Mech. Rev., 2002, Vol. 55, 325–350.
- [6] Carrera E.: *Developments, ideas, and evaluations based upon Reissner's Mixed Variational Theorem in the modeling of multilayered plates and shells*, Appl. Mech. Rev., 2001, Vol. 54, 301–329.
- [7] Carrera E.: *Historical review of Zig-Zag theories for multilayered plates and shells*, Appl. Mech. Rev., 2003, Vol. 56, 287–308.

- [8] Gilewski W., Radwańska M.: *A survey of finite element models for the analysis of moderately thick shells*, Finite Elements in Analysis and Design, 1991, Vol. 9, 1–21.
- [9] MacNeal R.H.: *Perspective on finite elements for shell analysis*, Finite Elements in Analysis and Design, 1998, Vol. 30, 175–186.
- [10] Yang H.T.Y., Saigal S., Masud A., Kapania R.K.: *A survey of recent shell finite elements*, Int. J. Num. Meth. Engng., 2000, Vol. 47, 101–127.
- [11] Simitses G.J.: *Buckling of moderately thick laminated cylindrical shells: A review*, Composites Part B, 1996, Vol. 27B, 581–587.
- [12] Waszczyszyn Z.: *Stability problems and methods of analysis of nonlinear FEM equations*, [in:] *Handbook of Computational Solid Mechanics*, M. Kleiber (Ed.), Springer-Verlag, Berlin, Heidelberg, 1998, 253–323.
- [13] *MSC/NASTRAN for Windows installation and application manual*, Mac Neal–Schwendler Corp., 1995.
- [14] *MSC/NASTRAN Encyclopedia for Version 69*, Mac Neal–Schwendler Corp., 1996.
- [15] MacNeal R.: *A simple quadrilateral shell element*, Computers & Structures, 1978, Vol. 8, 175–183.
- [16] Hoff C.C., Harder R.L., Campbell G., MacNeal R.H., Wilson C.T.: *Analysis of shell structures using MSC/NASTRAN's shell elements with surface normals*, Proc. 1995 MSC World Users' Conf., Universal City, CA, 8–12 May, 1995.
- [17] Hoff C.C.: *Improvements in Linear Buckling and Geometric Nonlinear Analysis of MSC/NASTRAN's Lower Order Elements*, MSC 1993 World Users' Conference, Arlington, VA, May 24–28, 1993.
- [18] Snell M., Morley N.: *The compression buckling behaviour of highly curved panels of carbon fibre reinforced plastic*, Proceedings of 5th Int. Conf. on Composite Materials, 1985, 1327–1354.
- [19] Jun S.M., Hong C.S.: *Buckling behavior of laminated composite cylindrical panels under axial compression*, Computers & Structures, 1988, Vol. 29, 479–490.
- [20] Laschet G., Jeusette J.-P.: *Postbuckling finite element analysis of composite panels*, Composite Structures, 1990, Vol. 14, 35–48.
- [21] Wagner W.: *Zur Formulierung eines geometrisch nichtlinearen Finite Elementes für zylindrische Faserverbundschalen*, Static und Dynamik in Konstruktiven Ingenieurbau, Festschrift Wilfried B. Krätzig, SFB 151 – Berichte, 1992, Nr 23, B3–B10.
- [22] Brank B., Carrera E.: *A family of shear-deformable shell finite elements for composite structures*, Computers and Structures, 2000, Vol. 76, 287–297.
- [23] Chaplin C.P., Palazotto A.N.: *The collapse of composite cylindrical panels with various thickness using Finite Element Analysis*, Computers & Structures, 1996, Vol. 60, 797–815.
- [24] Kreja I., Schmidt R.: *Large rotations in First Order Shear Deformation FE analysis of laminated shells*, Int. J. Non-Linear Mechanics (submitted).

Analiza stateczności kompozytowych paneli cylindrycznych w MSC/NASTRAN

Zanalizowano przydatność systemu *MSC/NASTRAN for Windows* w zakresie analizy stateczności kompozytowych powłok cylindrycznych. Przedstawiono krótki przegląd literatury dotyczącej numerycznej analizy powłok warstwowych. Omówiono zasadnicze równania opi-

sujaące problem stateczności konstrukcji w zakresie uogólnionego zagadnienia własnego stateczności początkowej oraz na drodze wyznaczenia pełnej ścieżki równowagi układu z zastosowaniem podejścia przyrostowego. Zaprezentowano podstawowe informacje o systemie *MSC/NASTRAN for Windows* ze szczególnym uwzględnieniem elementu powłokowego QUAD4. Obliczenia przeprowadzono dla dwóch wybranych przykładów paneli cylindrycznych poddanych równomiernemu ściskaniu w kierunku tworzącej, dokonując analizy zarówno stateczności początkowej, jak i problemu geometrycznie nieliniowego w procesie przyrostowym. Podstawowa różnica między analizowanymi przykładami polegała na przyjęciu innych warunków podparcia na prostych krawędziach: w przypadku pierwszego badanego panelu przyjęto swobodne podparcie prostych brzegów, podczas gdy w drugiej rozpatrywanej powłoce proste krawędzie były swobodne. Dla obu rozważanych wariantów przyjęto, że zakrzywione krawędzie są utwierdzone, z tym że jedna z nich ma możliwość sztywnej translacji na kierunku tworzącej. Otrzymane wyniki zestawiono z rozwiązaniami dostępnymi w literaturze oraz z rozwiązaniami uzyskanymi za pomocą własnego programu SHL04. Przeprowadzone badania porównawcze w pełni potwierdziły bogate możliwości systemu *MSC/NASTRAN for Windows*. Zaobserwowano ponadto, że zmiana warunków podparcia na wzdłużnych krawędziach paneli ma decydujący wpływ na zmianę jej podatności na imperfekcje. Jak wykazano w drugim przykładzie, numeryczne niedokładności modelu MSC/Nastran w przypadku konstrukcji wrażliwej na imperfekcje mogą prowadzić do przeskoku rozwiązania na ścieżkę pobifurkacyjną.



The influence of cyclic loading on the bond between concrete and steel bars

JANUSZ PĘDZIWIATR

Wrocław University of Technology, Wybrzeże Wyspiańskiego 27, 50-370 Wrocław

Research on bond under cyclic loading is usually performed using specimens of a very short bond length. Results of such a research show very often that bond can be completely destroyed. According to that, most standards demand some extra anchorage length of steel bars. Different results were obtained by the author from experiments on long specimens under eccentric tension. If a concrete member is properly designed for the sake of limit states and fatigue, anchored length of a steel bar can be the same as for ordinary concrete members.

Keywords: *concrete, cyclic loading, bond, anchorage length, model, experiments*

1. Introduction

There are two general types of cyclic loading: high-cyclic (fatigue) and low-cyclic (earthquake) loads. The aim of this paper was to show some problems of cyclic loading, which is a load history containing many cycles, but at a rather low bond. In Polish Standards [1], fatigue of construction must be taken into account if a number of cycles is higher than $5 \cdot 10^5$ and such loading is greater than 60% of the whole loads. Crane beams, bridge members, offshore structures are often subjected to such cyclic loadings. High-cycle loading mainly influences serviceability limit states. Taking account of the bond slip, it is important to distinguish two cases of loading – repeated loading when a sign of loading remains constant and reversed loading in which the sign is changing.

The bond refers to the phenomenon, which allows transferring load between the bar and the surrounding concrete. Until the strains in concrete and steel are of the same value, the bond is perfect and exists owing to adhesion. The secondary bond starts when a crack appears in a tension zone and there is a relative slip between a steel bar and the surrounding concrete. The main components of a bond are the bearing pressure against the steel lugs and friction between a bar and concrete. The forces acting on a surrounding concrete can cause some irreversible changes. The main of them are those shown in Figure 1. At a relatively low level of loading (bond), a slip of a bar causes breaking of adhesion at the lug surfaces 1. When slip is getting greater, the same process takes place in concrete between lugs 2 and some microcracks appear in the top of a lug 3. When a slip is getting greater, some damages of concrete in compression zone may appear 4, 5.

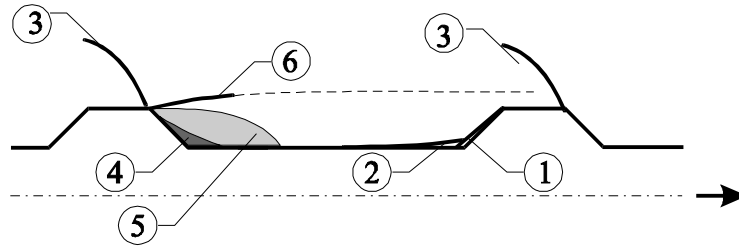


Fig. 1. Schematic view of the changes in concrete near a bar caused by bond forces

2. Research on bond under cyclic loading – short review

Generally, all researches on a bond under cyclic loading can be divided into two groups:

1. Slip-controlled tests, where graduated damage of bond can be seen as a decreasing value of bond stress.
2. Load-controlled tests, where graduated increasing of slip leads to pulling out a bar from concrete.

In the most experimental researches, specimens shown in Figure 2 were used. A steel bar was cast axially in a massive concrete cube. The bonded length was too small ($l_b \leq 5d_b$) to ensure the validity of an assumption of a constant value of bond stress. Such a small bond length causes that the bond phenomenon is not the same as in the real construction. If concrete cover is bigger than $3d_b$, a bar is confined very well and it makes impossible to split a cover. The only mechanism of bond failure is pulling out a bar from concrete. In a real concrete member, this can happen very seldom. Besides, some interesting observation can be easily made and lots of parameters can be taken into account in those kinds of experiments.

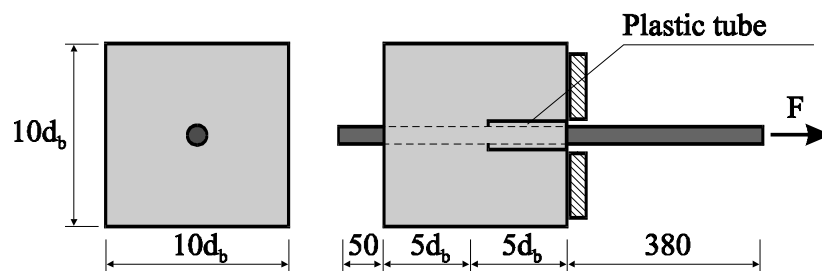


Fig. 2. A schematic view of a typical specimen for bond test

Rehm and Eligehausen [2] were ones of the first, who tested the bond behaviour under cyclic loads using lots of specimens being pulled out (more than 308). They

used cylinder member where the basic bond length was equal to $3d_b$ and a concrete cover was greater than $4d_b$. Only the bond failure due to shearing of concrete between ribs was possible. Two concrete mixtures and three bar diameters (but of almost the same related rib area $f_r \approx 0.075$) were used. During tests, a progressive increasing of slip measured at unloaded end was observed. Ultimate values of those slips (at failure) depended on a level of loading but in each case were greater than 0.5 mm. For loads causing the bond stress less than $0.65\tau_{b,\max}$, even more than 10^6 cycles did not lead to bond failure. In all cases, the dependence between a slip and a logarithm of load cycles was linear.

The most interesting conclusion from their experiments is that the repeated load has a similar influence on bond slip and on pure concrete. This means that the fatigue characteristic of the concrete between lugs is one of the most important factors. They also suggest that if the upper load is smaller than about 50% of the ultimate load for bond failure under monotonic loading, no fatigue failure of bond can occur.

As was said, the tests on concrete members with short embedded lengths ($l_b \leq 5d_b$) allow establishing the following relationships between a slip and a bond stress: $\tau_b = \tau_b(\Delta)$, where Δ (or s) is a slip of a steel bar. Many of the results of experiments on cyclic load have similar forms. It is interesting to answer the following questions:

- Is it possible to describe a bond behaviour under cyclic loading using only $\tau_b = \tau_b(\Delta)$ relationship for monotonic loads and additionally a damage parameter depending on number of cycles?
- How can be taken into account an influence of rib geometry?
- Can $\tau_b = \tau_b(\Delta)$ function, for monotonic loading, be used for establishing bond failure criterion for cyclic loads?

Some interesting conclusions drawn for a slip behaviour under cyclic loading at the constant value of a load (bond) were presented by Balazs [3]. There were three phases in slip increasing. At first, an increment in a slip was decreasing, then its value was constant and when the total value of slip reached s_1 (see Figure 3), each next increment was higher. This led to a complete pulling out a bar from concrete. That process took place, if the bond length was rather small, i.e. $\leq 5d_b$, and the residual slip occurred at a free end of a bar.

If a bonded length was longer ($l_b = 18d_b$ or $l_b = 24d_b$), each slip at a free end occurred and after some cycles the total value of the slip became constant [3]. We can say that for these embedded lengths there is no possibility to destroy a bond by pulling out a bar from concrete. Of course, this does not mean that at small values of concrete covers we can be sure that they are prevented from splitting.

During slip-controlled tests, bond degradation is observed as a decreasing value of a force (bond stress). The deterioration of a bond stress strongly depends on a value of slip excursion [4]. If it is less than lug spacing, there is any possibility to completed bond failure. Residual value of a bond is strictly connected with frictional part of bond. It decreases during each cycle in an asymptotic way because of polishing concrete but its final value is higher than zero.

For cyclic loading, it is very important to distinguish bond resistance components and to describe the rules governing their behaviours under cycles of loading.

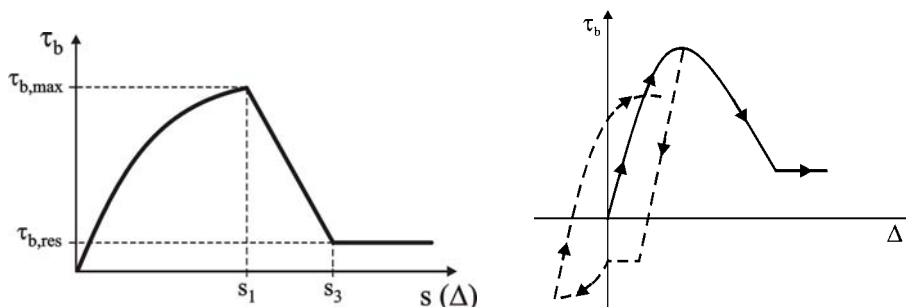


Fig. 3. Relationship $\tau_b = \tau_b(\Delta)$ for monotonic and cyclic loadings

That very short review of experimental and theoretical researches leads to the following conclusions:

- All tests and theories deal with a problem of bond failure caused by pulling out a bar from concrete and forces are acting directly on that bar.
- In some tests, cyclic loading causes bond failure, but there are also results showing that after a lot of cycles a bond stress is greater than zero and a bar cannot be pulled out from concrete.
- There is no test for checking the second mode of bond failure – splitting of concrete cover.
- Boundary conditions of bond during tests are very far from these of a real concrete structure.

3. Research program and theoretical results

In our research, the specimens similar to that shown in Figure 4 were used [5, 6]. The length of each specimen was 700 mm. This allowed several cracks to appear as in a real structure. The main experimental parameters were steel bar diameter and concrete cover (concrete member diameter). Almost a half of specimen was covered with an elasto-optical surface. This allowed us to see the changes in concrete strains on a whole surface and both appearance and development of cracks.

The elasto-optical surface allowed confirming the previous theoretical research on internal cracks. In Figure 5, such a crack which started from a steel bar and penetrates through a member and outside is seen.

The materials used in the preparation of concrete were ordinary Portland cement, natural sand and graded gravel of 8 mm maximum size with a water to cement ratio of 0.5. An average concrete cubic strength was in a range of 28–35 MPa after 28 days. An average tension splitting strength ranged from about 2.5 to 3.2 MPa and the modulus

of elasticity for a first monotonic loading was found to be approximately 31 GPa. One day after casting all specimens were stored in water for a week and later covered with water and laid in a box to avoid a shrinkage influence.

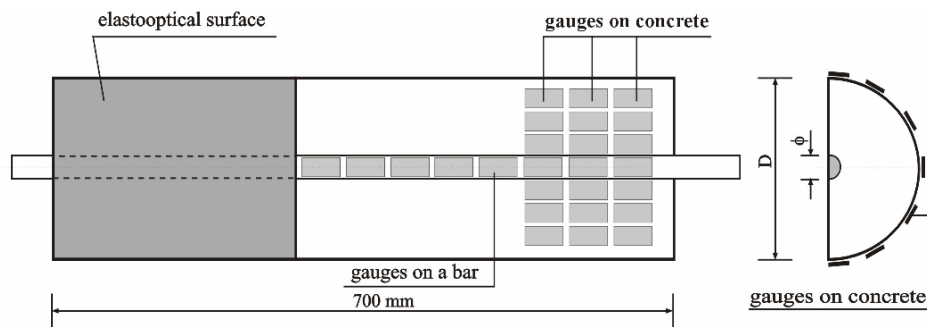


Fig. 4. Schematic view of a specimen used in bond test

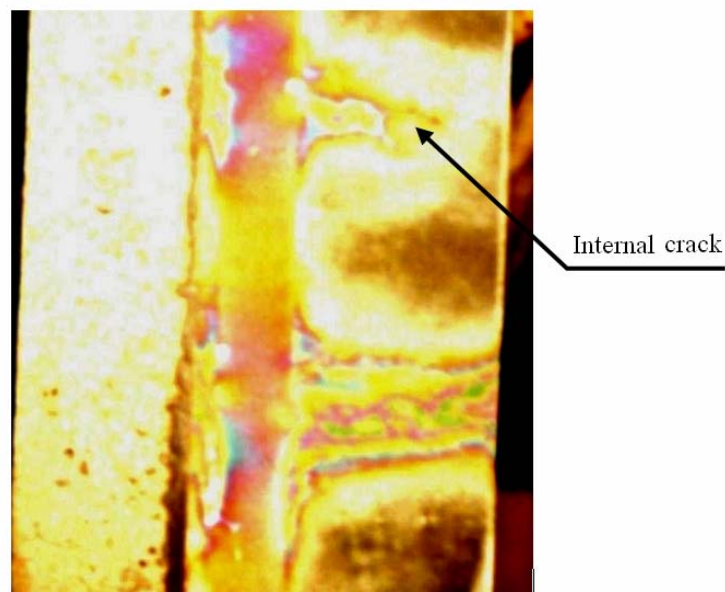


Fig. 5. The view of cracks in a member – top crack is an internal crack and bottom is a primary crack [7]

Strain gauges of a 15-mm base were glued to a priori mould bars one next to another. Their number varied from 19 to 21 for different specimens. Data from those gauges allowed checking strains distribution in a bar with a quite good accuracy. In the next step, the changes of a bond stress could be established using the following formule:

$$\tau_{b,j} = \frac{E_s d_b}{4} \frac{\varepsilon_{s,i+1} - \varepsilon_{s,i}}{x_{i+1} - x_i}. \quad (1)$$

Relationship (1) stands for a differential equation describing bond stress in function of steel stress changes. Since the distances between gauges were small, the above approximation is good enough. The value of $\tau_{b,j}$ concerns a cross-section between x_i and x_{i+1} . It is also possible to calculate $\tau_b(x)$ in a different way. Direct data from gauges can be approximated by a continuous function and then one can differentiate it. The results from both methods are very similar, but usage of Equation (1) is more comfortable. Some electric gauges were situated on a concrete to observe the changes in strains. Their location depended on a kind of phenomenon, which was tested. Some of the most interesting are as follows:

- *Additional strains in concrete caused by bond forces.* Those tests needed gauges situated in several cross sections at different distances from a crack. In every of those places three or more gauges were glued at different distances from a steel bar axis. This allowed us to establish clearly the value of those additional strains in a function of $\tau_b(x)$, a distance x from a crack and distance y from a bar axis.

- *Direction of bond stress.* In those tests the rosette gauges were used. They were glued as near to a steel bar as possible in three different cross sections.

- *Changes in concrete strains during arising and developing of cracks.* Optical methods are very useful to look after the strain changes in a large surface. They visualize the phenomenon but, on the other hand, the elasto-optical surface changes the properties of a tension concrete. The strain gauges were glued in two rows parallel to a bar axis.

- *Changes of neutral axis.* In that case, strain gauges were situated at the convex part of a specimen in three different cross-sections to check the influence of a distance from cracked cross-section.

Most of experimental researches deal with a monotonic loading, but several of them allow us to show the influence of cyclic loading. There were two basic loading histories:

- Cyclic loading between maximum and minimum levels of load.
- Monotonic loading to a level very close to yielding of a steel bar and next partial unloading and cyclic loading.

Researches were conducted with a strength machine where a slip of a bar was under control.

4. Theoretical backgrounds

The changes in concrete surrounding a steel bar (Figure 1) describe a situation where a slip has a great value. Such damages and irreversible changes take place if

a slip value is of the same order as a distance between ribs of a bar. Polish steel 34 GS of $d_b = 14$ and 16 mm was used in research and axial distances equalled 7 mm and 10 mm, respectively. This means that irreversible changes are possible if a slip is at least in the a range of 0.7–1.0 mm. Such a great value of a slip is often observed in test on specimens of a very small bond length. In a real concrete structure under service load it is impossible. The main slip occurs in a cracked cross-section and is limited by a half of a crack width. Even in the worst situation, it is smaller than 0.15 mm, if a member is properly designed. So we can assume that at service level of load, bond forces cannot cause significant damage like crushing concrete. Only some micro-cracks can appear near tops of the lugs and discontinuity on tension part of lugs. The only exception takes place very close a crack. A significant strain concentration was observed there during research. Due to an elasto-optical surface it was seen that the phenomenon is limited to a distance of about $2d_b$ only. Since a bond length is much longer, in practical aspect the damages in that area can be neglected.

If we assume that irreversible changes in concrete are of minor importance, the bond phenomenon under cyclic loading can be described as follows. Let a bar of a length l_b and a diameter d_b be fixed at one end and be loaded with a force F_0 . Its elongation $\Delta_0(x)$ under the stress $\sigma_0 = 4F_0 / (\pi d_b^2)$ is equal to:

$$\Delta_0(x) = \frac{\sigma_0}{E_s} (l_b - x), \quad (2)$$

where $x=0$ at loaded end. In a similar bar embedded in a concrete, a part of a force F_0 is transferred from a bar to the surrounding concrete which causes graduated decreasing of a steel stress. According to the theory presented earlier [4] it can be described by the following equation:

$$\sigma(x) = \sigma_0 \exp(-2gx^2 / d_b). \quad (3)$$

In that situation, a bar elongation will be less:

$$\Delta_1(x) = \frac{\sigma_0}{E_s} \int_x^{l_b} \exp(-2g\alpha^2 / d_b) d\alpha. \quad (4)$$

A relative difference between those elongations is equal to:

$$\beta(x) = \frac{\Delta_0(x) - \Delta_1(x)}{\Delta_0(x)} = 1 - \frac{1}{l_b - x} \int_x^{l_b} \exp(-2g\alpha^2 / d_b) d\alpha. \quad (5)$$

In Equation (5), g is a bond parameter (m^{-1}). It depends on a value of σ_0 , but during cyclic loading the changes of steel stress in a cracked cross-section are small enough to assume that g is constant. This implies that in any point $x = x_i$, the value of β is also constant. Particularly, this means that for any cycle a residual slip can be evaluated from Equation (6):

$$\Delta_r^i(x) = \Delta_0^i(x)\beta(x). \quad (6)$$

Residual slip causes development of residual strains in steel and concrete. Steel bar is under tension and concrete under compression. Residual strains in a bar can be calculated from the following equation:

$$\varepsilon_{s,r}(x) = \frac{\Delta_r(x)}{dx} = \frac{\sigma_s(x=0)}{E_s} \left\{ [1 - \beta(x)]^2 + [2\beta(x) - 1] \exp(-2gx^2 / d_b) \right\}. \quad (7)$$

The actual value of a steel strain is a sum of residual strain and strain caused by the latest loading.

The function (5) is increasing which means that remaining relative strain in steel has the smallest value of cracked cross-section and the biggest one at the end of bond length. In Figure 6, the distributions of two strains at different values of the parameter g are shown. A dotted line represents a smaller value. Since after unloading the bigger strains remain in the cross-section lying far from a crack, during the next loading cycle the strains in steel are getting more uniformly distributed along the bonded length which can be seen in Figure 7. Dotted line is represents the first cycle.

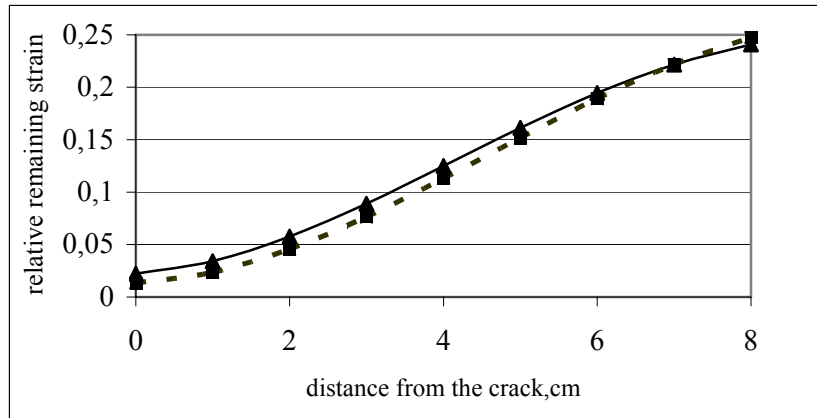


Fig. 6. Dependence of relative residual steel strain on the distance from a crack

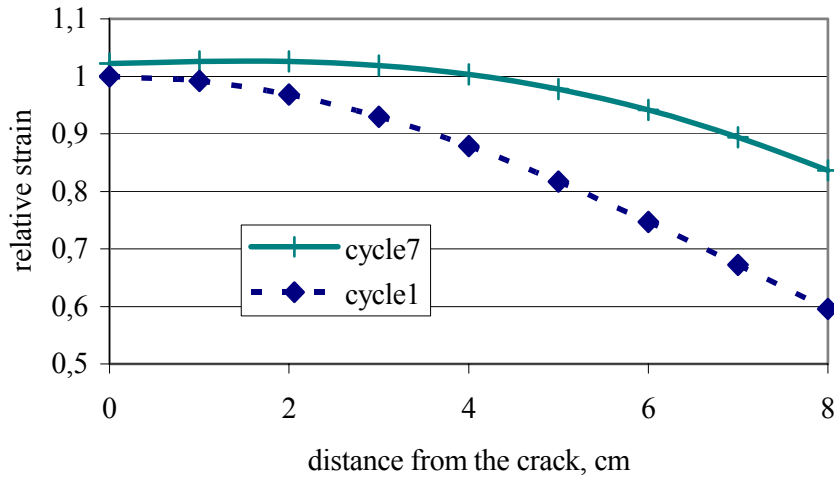


Fig. 7. Strain distribution at the first loading and after a full cycle

Theoretical model leads to some interesting conclusions:

- Residual stress at cracked cross-section is equal to $\sigma_r^i = \sigma_0^i \beta^2(x=0)$ and it depends on the bond parameter g . The smaller the value of g , the smaller the value of residual stress in steel. This means that relatively higher values of residual stresses occur at smaller values of stress. In consequence, the value of steel stress in cracked cross-section stabilizes practically very quickly after few cycles.
- Since larger increasing of steel stress occurs in cross-sections lying farther from a cracked section, the steel stress distribution is getting to be more uniform. This causes decreasing of a bond stress, particularly in the area next to a cracked cross-section. The point of a bond peak value is moving away towards to an end of bond length.
- During each cycle the slip of steel bar is growing at much higher rate than the steel stress in crack. Relatively large values of residual slip occur in the cross-section lying at a large distance from crack. Similar to the behaviour of steel stresses, relatively high values of residual slips occur for smaller values of stress.

From practical point of view, it is important to estimate the final values of steel stress and slip of a steel bar. As we assume that the bond parameter g is constant, the stresses in steel at cracked cross-section will create the following sequence: σ_0 , $\sigma_0 + \sigma_0 \beta^2(0)$, $\sigma_0 + \sigma_0 \beta^2(0) + \sigma_0 \beta^4(0)$, ... If a number of cycles tends to infinity, the steel stress can be calculated from the formule:

$$\sigma_0^\infty = \frac{\sigma_0}{1 - \beta^2(0)}. \quad (8)$$

In the same way, we can calculate the final values of slip and residual slip at the point $x=x_0$. The crack width can be interpreted as a double value of total slip (actual and residual). Its ultimate value after cycle loading can be estimated as:

$$w_{\infty} = 2 \left[\frac{A_0}{1-\beta^2} + \frac{A_0\beta}{1-\beta} \right] = w_0 \frac{1+\beta+\beta^2}{1-\beta^2}. \quad (9)$$

The value of crack width calculated from (9) overestimated its real value for, as was mentioned earlier, during cycles the loading values of g and β decrease slightly. Formulas (5) to (9) are valid if cyclic loading takes place between steel stresses equal to $\sigma=\sigma_0$ and $\sigma=0$. If lower level of loading is greater than zero, the rule of superposition can be used. Residual slip at stress $\sigma=\sigma_1>0$ can be calculated from Equations (5)–(7) substituting σ_s for $\Delta\sigma_s$ and using bond parameter g adequate for σ_1 .

5. Some experimental results

All the results obtained from tests on specimen described in chapter 2 were very similar independently of a bar diameter or a kind of steel. Even if a level of loading is relatively high, neither significant changes of steel strain distribution nor of bond after several cycles were observed. We can say that in a concrete member with typical reinforcement and bond length determined by crack spacing, any damages of bond did not occur.

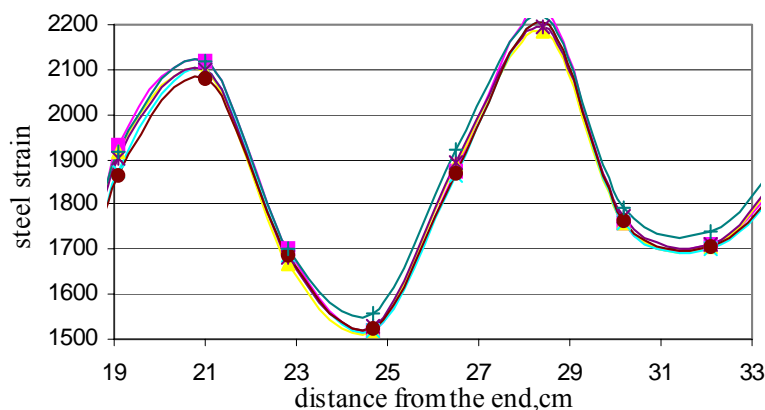


Fig. 8. Typical strain distributions measured during test at high level of loading

A typical steel strain distribution measured in an eccentric tension member is shown in Figure 8 (the values of strain in all figures are multiplied by 10^6). It is worth noticing that stress in steel in cracked cross-sections is much higher than at servicing level of loading and it is only slightly lower than yielding. Even so, an increase in steel

strain during cycles is very small. In Figure 9, the distributions of that strain in two cross-sections are shown. It is easy to see that an increase in strain is in both sections very small, but in a cracked cross-section (Figure 9b) it is significantly smaller than in the point in the middle of cracks (Figure 9a). The changes observed in width of crack confirm that an increase in steel strain during cycles is very small and does not influence bond dramatically (Figure 10a). Such results are in agreement with the theoretical model presented. They confirm all predicted trends in the behaviour of steel strain and bond stress under cyclic loading. In most cases, theoretical results are more conservative, i.e. they lead to a higher increase in crack width.

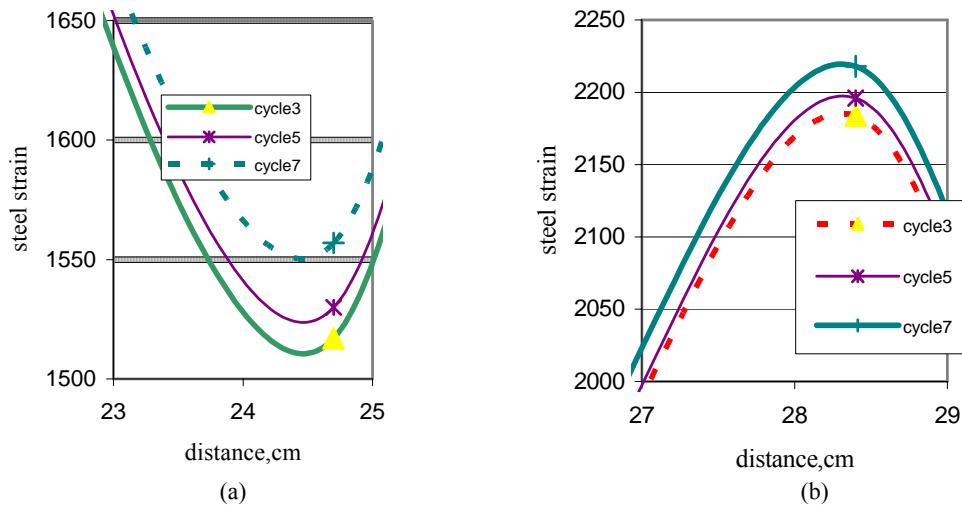


Fig. 9. Strain distribution near a local minimum (a) and maximum (b)

Besides the main trends, it is worth perceiving some other interesting phenomena. In every cycle, curves of loading are similar, but they differ from the curves of unloading. During one full cycle the curve representing loading is below an analogous curve representing following unloading. It is another evidence that the whole process is asymptotic. The same behaviour can be observed in respect to a width of crack (Figure 10b).

In some tests, where a crack width in the first cycle was greater than 0.35 mm, some significant changes in bond stress distribution were observed. A typical example is shown in Figure 11. The curves represent the bond stress distribution near a crack ($x \approx 24.2$ cm) for loading path (solid lines) and unloading (dotted lines) at two levels of loading. These pictures based on the strain measured can lead to some interesting conclusions:

- In every case, the distribution of bond stress near a crack during loading is strictly convex, while during unloading has a concave part.

- At loading part of cycle, there is a clear point of maximum bond stress situated fairly near a cracked cross-section.
- During unloading this peak value has almost the same value but it is situated rather far from the crack (peak moves away).
- During unloading path a bond stress decreases in a region near a crack, but it increases at farther distance from it, so total bond forces remain the same.

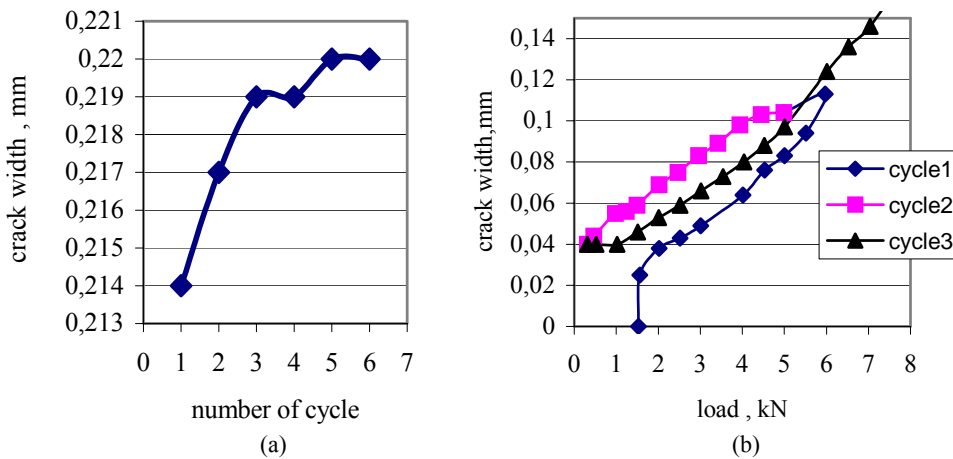


Fig. 10. Changes of crack width during cycles

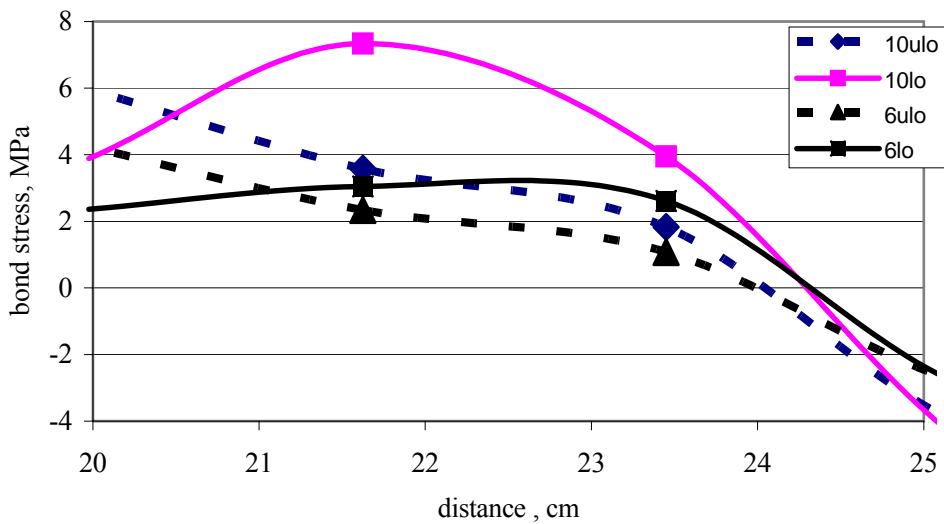


Fig. 11. Bond stress distribution near a crack

Such an observation can be made only if a specimen is long enough for several cracks to appear.

Such results seem to be strange if we compare them with the data well known from the literature. Most of them suggest that under cyclic loading there is a great increase both in steel strain and in width of crack. Especially this it refers to the first cycle. Those differences can be explained quite easily if we take into consideration the influence of a specimen kind on the results obtained. As was already mentioned, most tests were carried out on specimens of very short embedded length where a slip of a bar at its free end is measured. Sometimes, if a test is connected with the changes of a crack width, the specimens with artificial crack are used. That crack is made mechanically. Its width and depth are chosen arbitrarily. Such a procedure makes measurement easier since a position of a crack is known. On the other hand, such a crack in a real structure corresponds to a well-established level of loading. If a performed crack has a large depth or width, it may occur that it fits in with much higher level of loading than that used for cyclic loading. In such a case, there is a great difference in a specimen behaviour between the first and the second cycles. During the first cycle (loading) artificial crack does not influence much the steel strain in cracked cross-section and its neighbourhood. Unloading path differs, since only a part of a crack can be closed and that part corresponds to actual level of loading. The remaining width is much greater if a specimen was not cracked before testing. In consequence, a remaining strain in a steel bar is also higher. During the second cycle the strain in a bar is a sum of the remaining strain and the actual strain and is higher than an equivalent strain in a non-precracked member. In the next cycle, a specimen exhibits the behaviour like a member under certain loading but with an inadequate residual stress.

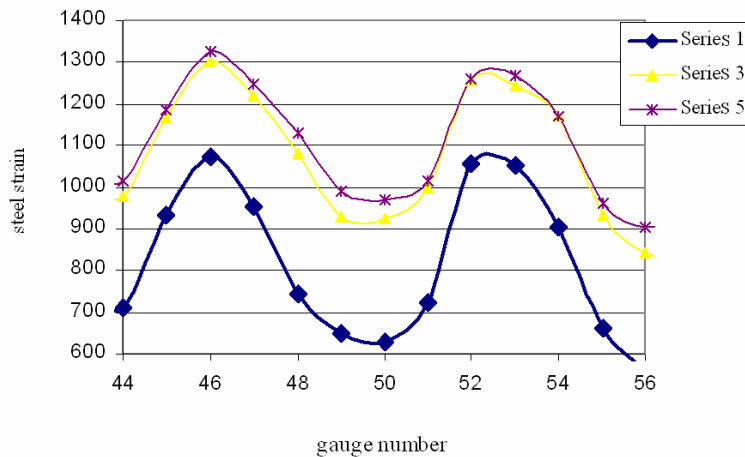


Fig. 12. Typical curves representing steel strain during the test in which a specimen was loaded to higher level than during cyclic loading

The situation is even worse if a specimen is a concrete member with a very short embedded length. In that case, a front of a specimen is an ideal crack including the whole cross-section. The width of such a “crack” is unknown and a hypothetical loading responsible for that is also unknown. The remaining slip and steel strain after the first cycle cannot even be estimated theoretically.

The hypothesis of a great influence of a specimen kind on the results of cyclic loading was verified. Some typical specimens were loaded to a certain level, then partially unloaded and later that lower level of load was tested under cyclic loading. In Figure 12, the results of such testing are shown. That specimen was loaded to 18 kN and then tested under cyclic loading in a range of 0–10 kN. A “series 1” represents the first loading to 10 kN. Then the specimen was loaded to 18 kN, unloaded to zero and again loaded to 10 kN – “series 3”. There is a significant difference in steel strains between those cycles. As was said, it is caused by a residual stress connected with the load equal to 18 kN. In the next cycle that remaining stress does not change and following lines lie near each other (“series 3” and “series 5”). That phenomenon was observed in all tests if a specimen was loaded to the value higher than a level of cyclic loading. This can explain similar results reported in literature, obtained from the members with artificial crack or a short length.

6. Conclusions

Several kinds of important concrete structures work under cyclic loading. They are designed using traditional methods based on the theory of linear stresses, which makes their safety margin very large, much larger than that in limit states methods. Additionally, the standards require some extra anchorage length for bars in those structures. Such conservative recommendations are based on the results obtained from tests suggesting that cyclic loading can easily lead to bond failure and very significant increase in width of cracks.

The author’s theoretical and experimental research suggests that in a real structure cyclic loadings are not responsible for such dangerous phenomena. In correctly designed concrete structure, typical development of length will be good enough. Bond deterioration is rather small which is connected with a relatively small decrease in maximum value of bond stress and its movement away from cracked cross-section. The highest changes in steel strain take place in a region of the middle between adjacent cracks and do not pose any danger for a member. They only cause a certain growth of crack width. A theoretical way of estimating that increment of width was presented. It is worth noticing that at higher levels of loading (greater crack width) an increase is smaller than at a small initial width.

A way of testing has a great influence on experimental results. In some cases, the embedded part of a structure was so long as to guarantee the existence of a point where a slip was equal to zero. Results of those tests were similar to the ones presented above – there was not bond failure [8]. When the tests were carried out on

specimens with a very short bond length, the results were completely different. After some cycles a bond was broken. If a test was slip-controlled, a bond stress diminished to residual value. If a test was force-controlled, a bar was pulled out from a specimen.

In really existing structures designed properly, according to standard recommendations, a bond failure cannot occur. Cyclic loading cannot pull out a bar from surrounding concrete nor split a concrete cover. The only considerable effect is the increase in a crack width, but it is not very drastic.

References

- [1] PN-B-03264:2002: *Plain, reinforced and prestressed concrete structures – Analysis and structural design* (in Polish).
- [2] Rehm G., Eligehausen R.: *Bond of Ribbed Bars Under High Cycle Repeated Loads*, ACI Journal, Symposium Paper, February 1979, pp. 297–309.
- [3] Balazs G.: *Fatigue of Bond*, ACI Materials Journal, 1991, Vol. 88, No. 6, pp. 620–628.
- [4] Pochanart S., Harmon T.: *Bond-Slip Model for Generalized Excitations Including Fatigue*, ACI Materials Journal, 1989, Vol. 86, No. 5, pp. 465–474.
- [5] Pędziwiatr J.: *The new model for cracking analysis of tension reinforced members*, Archives of Civil Engineering, 1996, pp. 47–64.
- [6] Pędziwiatr J., Hoła J., Styś D.: *Study of the transfer of tensile forces by bond in eccentric reinforced concrete members*, 13th ECF, San Sebastian, 2000, pp. 137–144.
- [7] Jankowski L., Pędziwiatr J., Styś D.: *Some problems of researches on bond in reinforced concrete members* (in Polish), 18th Symposium on Experimental Mechanics of Solids, 1998, pp. 217–222.
- [8] Moro M., Ogawa J.: *Bond behavior of anchored deformed bar under high-stressed reversal loading*, International Conference on Bond in Concrete, Riga, 1992, pp. 1–79.

Wpływ obciążeń cyklicznych na przyczepność stali do betonu

Badania wpływu historii obciążenia, podobnie jak i inne testy, przeprowadza się głównie na elementach, w których długość odcinka przyczepności jest bardzo mała. Jest to bardzo wygodne, jeżeli chodzi o prowadzenie badań, ale uzyskane rezultaty są mało wiarygodne. Gdy bada się wpływ obciążeń cyklicznych na przyczepność, wtedy dochodzi się do wniosku, że kolejne cykle tak osłabiają przyczepność, że w ostateczności ulega ona całkowitemu zniszczeniu.

Własne badania prowadzono na długich elementach mimośrodowo rozciąganych i zginanych. Ich wymiary gwarantowały powstawanie stanu zarysowania analogicznego do istniejącego w rzeczywistych konstrukcjach. Usytuowanie odpowiednio frezowanej stali zbrojeniowej bezpośrednio przy powierzchni elementu umożliwiło bezpośredni pomiar zmian odkształceń w stali. Te pomiary stanowiły podstawę do analizy zjawiska przyczepności traktowanego jako mechanizm transferu siły ze stali do otaczającego betonu.

Wyniki takich badań uprawniają do stwierdzenia, że konstrukcje poddane działaniu obciążeń wielokrotnie zmiennych, zaprojektowane zgodnie z wymaganiami normy, nie są narażone na zniszczenie mechanizmów współpracy stali i betonu. Oznacza to w szczególności, że zby-

teczne jest zalecane przez normę 50% zwiększanie długości zakotwienia prętów użytych w tych konstrukcjach.

W pracy podano również uproszczony model teoretyczny pozwalający śledzić zmiany odkształceń w stali podczas obciążeń cyklicznych oraz obliczać zmiany szerokości rozwarcia rys. Wyniki teoretyczne są zgodne z rezultatami badań, ale sytuują się po stronie bezpiecznej.

Wnioski płynące zarówno z badań, jak i rozważań teoretycznych mogą pomóc w racjonalnym projektowaniu konstrukcji żelbetowych poddanych działaniu obciążeń wielokrotnie zmiennych.



Study on dynamic characteristics of timber frame structure by microtremor measurements

NAOYA SHOJO

Akashi National College of Technology, 679-3 Nishioka Uozumi-cho Akashi City 674-8501 Japan

YOSHINOBU FUJITANI

Hiroshima International University, 5-1-1 Hirokoshinkai, Kure City 737-0112 Japan

SHINYA MATSUMOTO

Hiroshima University, 1-4-1 Kagamiyama Higashi-Hiroshima City 739-8527 Japan

YOSHIAKI OHNO

WOOD ONE Co.,Ltd. , 1-1 Mokuzaikou-Minami Hatsukaichi City 738-8502 Japan

YOSHIMITSU OHASHI

Musashi Institute of Technology, 1-28-1 Tamazutsumi Setagaya-ku Tokyo 158-8557 Japan

In this paper, the dynamic characteristics of a timber frame structure are given based on microtremor measurements. The microtremor was measured in two stages of construction. In the first stage, the columns, the beams and the floors are constructed, and in the second stage the bearing walls are added to them.

Moreover, a natural frequency obtained by this microtremor measurement was compared with the analytical solution obtained by using the rigid bar element with the springs for bending in both ends.

Keywords: *full-scale timber frame structure, microtremor measurement, natural frequency, frame analysis*

1. Introduction

In 1995, many timber structures in Japan were damaged by the Hanshin Great Earthquake, and the research on timber structures has been developed gradually. The frame structure has a high flexibility for the floor planning, and it is appropriate for Skeleton-Infill Housing. Therefore, realization of the timber frame structure is to be expected in near future. But, the jointing techniques with strong stiffness are required in order to resist horizontal force such as seismic force.

We have proposed a jointing technique using round bars and drift pins. We also carried out the bending test on the beam-column joints and the column base joints. Then we verified the rotation rigidity and the bending strength [1, 2]. Furthermore, we conducted the tension test on the drift-pin-joint and the compressive grain test as elementary experiments for the moment resisting elements. Next, the moment resisting elements of the joint and spring elements were modelled, and the relation between the bending moment and the rotational angle of joints was calculated. Then we can grasp

the relationship between elementary experiments and bending experiments of joints [3].

In this paper, the results of the microtremor measurements for an actual building based on the timber frame structure are summarized. The microtremor was measured in two construction stages. In the first stage, the columns, the beams and the floors were constructed, and in the second stage, the bearing walls were added to them.

2. Outline of the building by the timber frame structures

The building to be measured is bi-directional timber frame structure with 4 m and 6 m spans. The general views of this building are shown in Figure 1 and Figure 2, and the list of main structural materials is given in Table 1. Laminated Veneer Lumber (LVL) was used as a main structural material. The round bars and drift pins are used in the beam-column joints and in the column base joints shown in Figure 3.

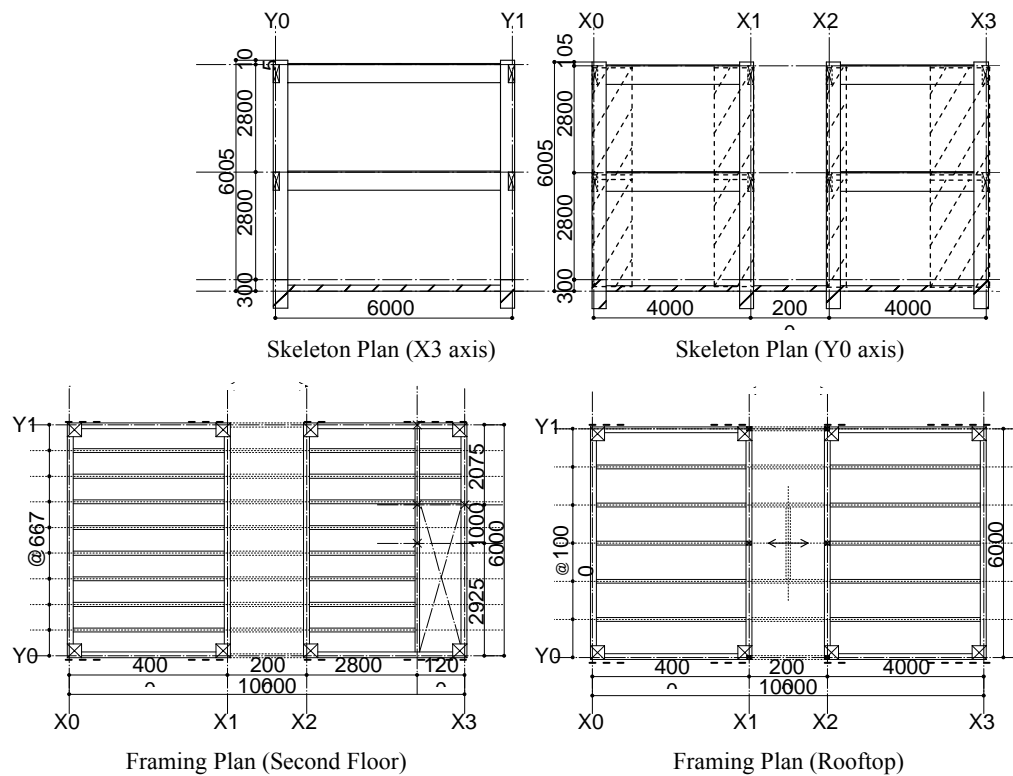


Fig. 1. The framing plan and the skeleton of the building
(dotted line: installation position of the bearing wall)



Fig. 2. View of the building (left: the framework stage, right: the framework-wall stage)

Table 1. The list of main structural materials

Structural part	Material classification (wood classification: radiata pine)	Mechanical grade classification (Japanese industrial standard)	Cross section width×height (unit: mm)
Sill	LVL for structural	80E	105×105
Column	LVL for structural	110E	360×360
Girder	LVL for structural	110E	150×480
Beam	LVL for structural	110E	105×240
Floor plywood	Plywood for structural	–	thickness: 28.0
Exterior plywood	Plywood for structural	–	thickness: 9.0

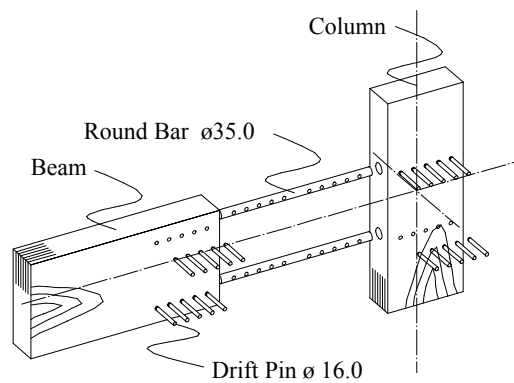


Fig. 3. The beam-column joint

3. Microtremor measurement

3.1. Outline of the measurement

The microtremor is measured in two construction stages. In the first stage, the columns, the beams and the floors are constructed (henceforth, it is called *the framework stage*), and in the second stage, the bearing walls are added to them (henceforth, it is called *the framework-wall stage*). Moreover, the static experiment is conducted in each stage, the microtremor is measured before and after that static experiment. The stages are divided into the following four patterns:

- I. The framework stage before the static experiment.
- II. The framework stage after the static experiment.
- III. The framework-wall stage before the static experiment.
- IV. The framework-wall stage after the static experiment.

The microtremors are measured on one side of the building. And they are measured in the directions of 4-m spans and 6-m spans. The microtremors are measured by servomotor accelerometer of Tokyo Sokuhin Co., Ltd. The vibration data is recorded for 60 seconds. The accelerometers are set on the foundation level, the second floor level, and the top level of the building.

3.2. The results of the microtremor measurement

A natural frequency of the building structure is obtained by using spectrum analysis. The vibration data is shown in Figure 4 as an example, and Figure 5 shows each Fourier spectrum in the framework stage before the static experiment, in the 4-m span direction. The natural frequencies for all the stages are listed in Table 2.

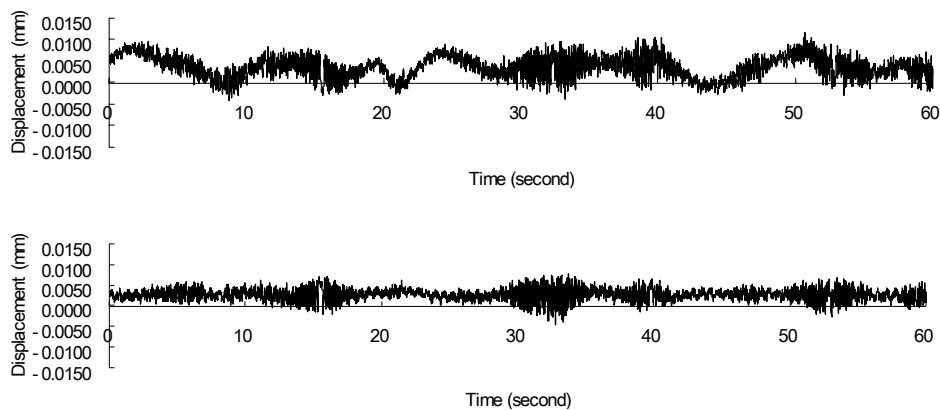


Fig. 4. An example of the vibration data
(above: the top level, below the second floor level)

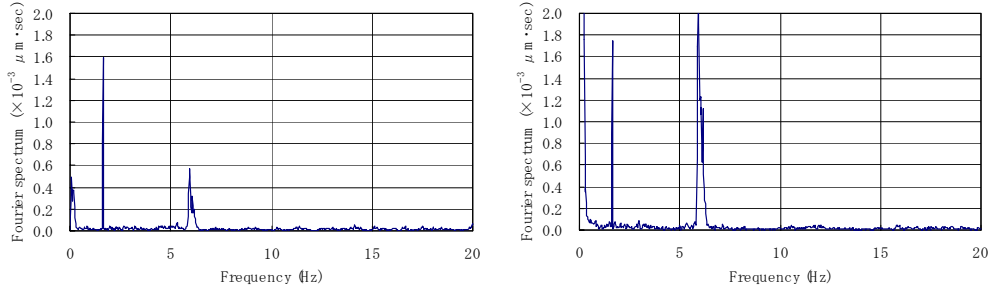


Fig. 5. The Fourier spectrum (left: the second floor level, right: the top level)

Table 2. The natural frequencies (in Hz)

	Framework stage		Framework-wall stage	
	Before	After	Before	After
4-m span direction	5.91	5.30	7.47	6.91
6-m span direction	5.86	5.86	6.08	5.83

The difference in the Fourier spectrum before and after static experiments in the framework stage for 4-m span direction is approximately 10%. On the other hand, this difference for 6-m span direction is negligibly small because of non-loading direction in the static experiment.

4. Numerical analysis of the natural frequencies

As the rotational rigidity of the joints is very small compared to the flexural rigidity of the column and the beam in a timber frame structure, the dynamic behaviour of the timber structure is almost exclusively determined by the rotational rigidity of the joints. Therefore, the natural frequency of two-storey framed structure is represented by the rigid bar model.

4.1. Derivation of a natural frequency using the rigid bar model

The two-storey and one-span model is considered (see Figure 6).

If the horizontal force of the top level P acts on the two-storey and one-span model, the horizontal displacement δ is calculated by the slope-deflection method, following Equations (1) and (2):

- the horizontal displacement of the second-floor level,

$$\delta_1 = \frac{\alpha_1}{\alpha_0} \frac{H^2}{12E_1I_1}, \quad (1)$$

- the horizontal displacement of the top level

$$\delta_2 = \frac{\alpha_2}{\alpha_0} \frac{H^2}{12E_1I_1}, \quad (2)$$

where

$$\alpha_0 = 36E_2^2I_2^2H^2k_1k_2^2 + 18E_1I_1E_2I_2Hk_2\{2E_2I_2(3k_1+k_2) + k_1k_2L\} + E_1^2I_1^2(6E_2I_2+k_2L)\{6E_2I_2(k_1+2k_2) + k_1k_2L\},$$

$$\alpha_1 = P(18E_2^2I_2^2H^3k_1k_2^2 + 12E_1^3I_1^3(6E_2I_2+k_2L)^2 + 9E_1I_1E_2I_2H^2k_2(18E_2I_2k_1 + 8E_2I_2k_2 + 3k_1k_2L) + E_1^2I_1^2H(6E_2I_2+k_2L)(30E_2I_2k_1 + 78E_2I_2k_2 + 5k_1k_2L)),$$

$$\alpha_2 = P(36E_2^2I_2^2H^3k_1k_2^2 + 24E_1^3I_1^3(6E_2I_2+k_2L)^2 + 8E_1^2I_1^2H^2(6E_2I_2+k_2L)(3E_2I_2(4k_1+5k_2) + 2k_1k_2L) + 9E_1I_1E_2I_2H^2k_2(42E_2I_2k_1 + 10E_2I_2k_2 + 7k_1k_2L)),$$

in which H means the height of the storey, I_1, I_2 are the geometrical moments of inertia of the sections, E_1, E_2 are the values of Young's modulus of the members and k_1, k_2 stand for the spring constant of the joints.

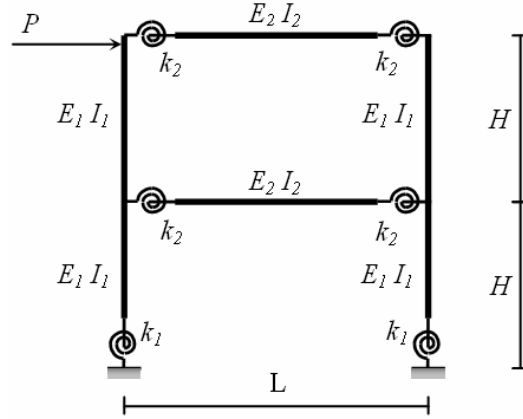


Fig. 6. The two-storey and one-span model

If the rigid bar model (the flexural rigidity $EI \rightarrow \infty$) is applied to Equations (1) and (2), the horizontal displacement is computed by the following equations:

- the horizontal displacement of the second-floor level δ_1

$$\lim_{\substack{E_1 I_1 \rightarrow \infty \\ E_2 I_2 \rightarrow \infty}} \delta_1 = \frac{H^2}{k_1 + 2k_2} P_2, \quad (3a)$$

- the horizontal displacement of the top level δ_2 ,

$$\lim_{\substack{E_1 I_1 \rightarrow \infty \\ E_2 I_2 \rightarrow \infty}} \delta_2 = \frac{2H^2}{k_1 + 2k_2} P_2. \quad (3b)$$

The storey rigidities k_1 and k_2 from these equations are expressed by the following equation:

$$K_1 = K_2 = \frac{k_1 + 2k_2}{H^2} + K_w, \quad (4)$$

where K_w means the rigidity added by the bearing wall.

If the natural frequency is computed based on the two-degree-of-freedom system model and taking into account the storey rigidity obtained from Equation (4), it is given by the following equation:

$$f = \frac{1}{2\pi} \sqrt{\frac{(k_1 + 2k_2 + H^2 K_w)(m_1 + 2m_2 - \sqrt{m_1^2 + 4m_2^2})}{2H^2 m_1 m_2}}. \quad (5)$$

In the case without bearing wall, K_w is omitted.

4.2. Comparison of model results with the results of microtremor measurements

In the numerical analysis of the natural frequencies, the rotation rigidities of the beam–column joint and the column base joint are approximately 6000 kNm/rad. and 12500 kNm/rad., respectively. And the wall rigidity K_w obtained in static experiment carried out on the bearing wall whose tangential rigidity at the origin of the envelope is adopted is 3.93 kN/mm. The natural frequencies and experimental ones obtained by the microtremor measurement are given in Table 3.

Table 3. Comparison of the analytical and experimental results (in Hz)

Static experiment		Framework stage		Framework-wall stage	
		Before	After	Before	After
4-m span direction	Analysis	5.48		6.38	
	Microtremor	5.91	5.30	7.47	6.91
6-m span direction	Analysis	5.48		5.48	
	Microtremor	5.86	5.86	6.08	5.83

In the framework stage, there is a close correspondence between the natural frequencies obtained by the analysis of the rigid bar model and by the microtremor measurements. However, in the framework-wall stage for the 4-m span direction, the calculated natural frequency is approximately by 10% lower compared to measurements. It is considered that the rigidity of the bearing wall is underestimated.

5. Conclusions

In this paper, we presented the results of the microtremor measurement of the timber frame structure and the natural frequencies were verified by their comparison with the analytical frequencies obtained based on the rigid bar model.

The natural frequencies of the timber frame structure expressed by the microtremor measurement ranged from 5.30 to 5.91 Hz in the framework stage and from 6.91 to 7.47 Hz in the framework-wall stage in the 4-m span direction. And the natural frequency was reduced by approximately 10% after the static experiment.

The natural frequency was computed based on the rigid bar model and then compared with the microtremor measurements. In the framework stage there was a close correspondence between the computed and measured results. In the frame-wall stage in 4-m span direction, the natural frequency was approximately by 10% lower compared with the measurements. It is considered that the rigidity of the bearing wall is underestimated.

References

- [1] Naoya Shoji, Yuji Makishima, Hiroyuki Nogomi, Yoshiaki Ohno, Yoshinobu Fujitani, Yoshimitsu Ohashi: *Study on the Joint of Timber Frame Structures* (in Japanese) (Part 1), (Part 2), (Part 3), Summaries of Technical Papers of Annual Meeting of Architectural Institute of Japan (kanto), Structural III, 2001, pp. 123–128.
- [2] Yoshiaki Ohno, Yusyo Nakamoto, Naoya Shoji, Hiroyuki Nogomi, Yuji Makishima, Yoshinobu Fujitani, Yoshimitsu Ohashi: *Experiment on the Joint Using Drift Pins in Timber Frame Structures and an Examination of the Rotation Rigidity* (in Japanese), Architectural Institute of Japan Journal of Technology and Design, 2001, No. 14, pp. 107–112.
- [3] Yoshiaki Ohno, Yuji Makishima, Naoya Shoji, Hiroyuki Nogomi, Yoshinobu Fujitani, Yoshimitsu Ohashi: *Study on the Beam-Column Joint of Timber Frame Structures Using Drift Pins* (in Japanese), Journal of Structural and Construction engineering (Transactions of Architectural Institute of Japan), 2003, No. 567, pp. 85–92.
- [4] Naoya Shoji, Yoshinobu Fujitani, Yuji Makishima, Hiroyuki Nogomi, Yoshiaki Ohno, Yoshimitsu Ohashi: *Study on the Beam-Column Joint of Timber Frame Structures Using Drift Pins, Part 2. Examinations by the experiments of the moment resisting elements and full-scale structure* (in Japanese), Journal of Structural and Construction Engineering (Transactions of Architectural Institute of Japan), 2004, No. 578, pp. 91–97.

- [5] Kasal B., Pospisil S., Jirovsky I., Heiduschke A., Drdacky M., Haller P.: *Seismic performance of laminated timber frames with bar-reinforced joints*, Earthquake Engineering and Structural Dynamics, 2004, Vol. 33, pp. 633–646.
- [6] Larsen H.J., Jensen J.L.: *Influence of semi-rigidity of joints on the behaviour of timber structures*, Progress in Structural Engineering and Materials, 2000, Vol. 2, pp. 267–277.

Badania dynamicznej charakterystyki drewnianej konstrukcji ramowej poddanej mikrowstrząsom

Przedstawiono wyniki pomiarów przemieszczeń i częstotliwości drgań spowodowanych mikrowstrząsami podczas wznoszenia drewnianej konstrukcji nośnej budynku. Wielkości te były mierzone w dwóch etapach realizacyjnych: w pierwszym po wykonaniu szkieletu konstrukcji składającego się ze słupów, belek i stropów oraz drugim po dodaniu do tego szkieletu ścian nośnych usztywniających. Ponadto w każdym z tych etapów przeprowadzono doświadczenia statyczne polegające na badaniach wytrzymałościowych złączy, przy czym przemieszczenia i częstotliwości drgań mierzono przed i po tych doświadczeniach statycznych. Przeprowadzono cztery następujące rodzaje badań dynamicznych:

- I : badanie dynamiczne szkieletu przed badaniami statycznymi,
- II: badanie dynamiczne szkieletu po badaniach statycznych,
- III: badania dynamiczne konstrukcji szkieletu + ściana przed badaniami statycznymi,
- IV: badania dynamiczne konstrukcji szkieletu + ściana po badaniach statycznych.

Częstotliwość drgań mierzono na poziomie posadowienia, stropu nad parterem i na poziomie stropu nad drugim piętrem. Częstotliwość drgań własnych otrzymano stosując analizę spektralną. W pracy podano wartości częstotliwości drgań własnych zmienionych podczas podanych wyżej rodzajów badań oraz wartości tych częstotliwości uzyskane w wyniku analizy numerycznej dwupiętrowej jednonawowej konstrukcji ramowej przy wykorzystaniu modelu sztywnego pręta. Uzyskano stosunkowo dobrą zgodność wyników badań otrzymanych dzięki zastosowaniu tych metod dla przypadku etapu szkieletu konstrukcji, w przypadku zaś konstrukcji szkieletu ze ścianą usztywniającą częstotliwość drgań własnych otrzymana w wyniku analizy jest około 10% niższa niż uzyskana w pomiarach.



Strain and stress patterns in the normal cross-sections of bended gypsum elements

S. KLIN

Agricultural University of Wrocław, Pl. Grunwaldzki 24, 50-363 Wrocław

The study presents the results of examining the distribution of strains and stresses in the normal cross-sections of bended gypsum beams, dry prepared, made of building gypsum pastes at water-to-gypsum (W/G) ratios equal to 0.5, 0.6, 0.8, 1.0 and 1.5. The strain was measured by the strain gauge method, whereas deflections of the beams were measured with displacement sensors. Strain distributions were found to be almost linear at the effort level of $\sigma_{gt}/f_{gt} = 0.9$, which is according to the Bernoulli distribution. The limit values for strains in the cracking zone were determined from the formula $\varepsilon_{gtb} = 46.24 f_{gc}^{0.0888} \cdot 10^{-5}$. Various patterns of internal forces, i.e. stresses in the bended normal cross-sections, were analyzed. The following calculation schemes were assumed: a triangular one in the compression zone and rectangular one in the cracking zone. The pattern developed on the basis of original test results conforms to the Murashev theory formulated for concrete cross-sections. The formula for the representative tensile strength of bended gypsum elements was proposed as $f_{gt}^n = 0.5\delta f_{gtb} = 0.574 f_{gtb}$, where f_{gtb} is the standard strength, as for elastic materials. The elastic/plastic bending index for gypsum cross-sections was proposed as $W_{gep} = W_{ge} / 0.5\delta = 1.7496 W_{ge}$, where: $W_{ge} = bh^2 / 6$, as for elastic materials. The formula for bending capacity of gypsum cross-sections was suggested in the form of $M_n = W_{gep} f_{gt}^n$.

Keywords: *gypsum, bending strength, strain, limit load capacity*

1. Introduction

Gypsum is one of the commonly used building materials characterized by many outstanding features. Currently, gypsum products – wide range of dry mortars and pre-fabricated gypsum plaster boards – dominate in the inside building finishing operations.

In the past decades, after the World War II, in the time of the cement deficiency due to a considerable destruction of the building industry, structural walls of many dwelling houses were made of gypsum pastes, mortars and concrete by casting and shuttering method with hollow masonry units [3, 16] or planks [15] made of gypsum. The “Pras-Gips” process was used for erection of large-size partition walls [18]. For the analysis of designs and processes used for building the gypsum houses see the reference studies [9, 17].

In the period of 1985–1997, in Poland some new structural systems were developed and officially implemented in dwelling building industry. In such systems, concrete or reinforced concrete skeletons were located in vertical channels formed in

load-bearing walls by arrangement of special hollow masonry units made of gypsum. For design solutions, in chronological order, see [20, 29, 13, 24, 25, 2]. The concrete load bearing structures were not exposed to possible creeping in the case of accidental damping of the gypsum hollow blocks. Therefore, the problem of possible loss of strength of gypsum units used in such hybrid structures became less important.

Nevertheless in the building industry, the strength of gypsum remained still important. The buildings with structural walls made of gypsum erected in past decades [16, 9] (among others 110 dwelling houses in Łódź, in Bałuty and Rokita Nova districts, 26 two-storey houses made of gypsum planks in Zgorzelec, houses built in the vicinity of Busk, including those erected in the period of 1922–1939 and still lived-in, buildings erected and occupied in Wrocław, Warsaw, near Pińczów and Rawa Mazowiecka) require continuous inspection and maintenance. Currently, due to complete lack of prescriptive regulations concerning the methods of calculation or assessment of load capacity of gypsum walls, we are in the state of technical and legal paralysis. There are no possibilities of determining statics and strength of these buildings, usually necessary for repair purposes, for structural survey, for evaluation of safety or for determination of the procedures needed in the case of emergency, e.g. extinguishing house fire with water. Our current standards established for brickworks [21, 22] cannot be applied to structures made of gypsum.

This issue refer to gypsum houses not only in Poland, but also in other European countries [16], in particular to the former Soviet Union area, where gypsum was used in building [3, 31].

Currently, in the conditions of wide application of the gypsum plaster board in finishing work, there are no standards of calculation of safety factors to be considered in the case of underslung floors, built-in lofts and execution of ceilings. The monograph by Hanusch [5] provides the methods for calculation of strength of vertical partitions in multilayer walls with gypsum plaster board shielding based on very simplified theory of elasticity adopted for such multi-layer elements.

The considerations presented in the study are aimed at providing a scientific basis for future defining the strength and safety standards required for the application of gypsum elements in well-founded cases. The tests and analyzes refer to the elements in dry conditions. In the conditions of moisture, creeping of gypsum under permanent and variable loads plays the decisive role. Determination of strength limits for such cases is a separate scientific problem, which should be solved to enable qualitative and quantitative assessment of the actions to be taken in cases of accidental moistening or flooding a part of a building. Contributory studies of other authors [6, 27, 28] have not clarified these issues.

2. Examination methods

The examinations were carried out using the building-grade gypsum β -CaSO₄·0.5H₂O made of natural raw materials by its calcination in rotary kilns, currently

available in the market, marked with the laboratory code numbers 2-02 and 2-03. For mineral composition of the gypsum see the Table.

Table. Mineral composition of the building grade gypsum

Components	Percentage [%]	
	Gypsum No. 2-02	Gypsum No. 2-03
Gypsum hemihydrate (CaSO ₄ ·0.5H ₂ O)	80.87	82.43
Anhydrite III (CaSO ₄)	0.00	0.00
Stabilized anhydrite II (CaSO ₄)	2.80	1.78
Anhydrite II (CaSO ₄)	0.31	0.26
Gypsum dihydrate (CaSO ₄ ·2H ₂ O)	4.67	4.26
Inactive substances	10.46	10.74
Moisture	1.20	0.71

The tests were carried out with the beams 4 cm × 4 cm × 16 cm and similar beams 6 cm × 10 cm × 50 cm made of gypsum pastes at water-to-gypsum (*W/G*) ratios from 0.4 to 1.5. Deformation in the bended cross-sections was measured with extensometer sensors (Figure 1), and deflection was measured at the same time with displacement sensors.

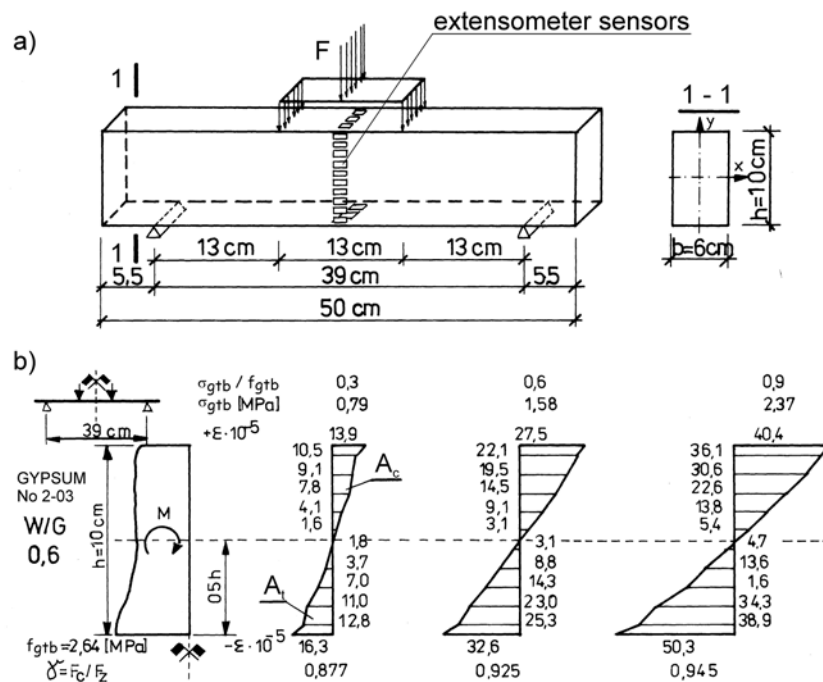


Fig. 1. a) Arrangement of loads and extensometer sensors on the bended dry beams made of building gypsum; b) the strain values ϵ in the cross-section of the beam made of gypsum paste at *W/G* = 0.6: σ_{gtb} – bending stress in the beam, f_{gtb} – total yield stress (fracture), A_c – compression zone, A_t – tension zone

3. Examination of strain and stress patterns in the normal cross-sections of the gypsum beams bended

The examples of strain and stress patterns in the normal cross-sections of the beams made of pastes at W/G ranging from 0.5 to 1.5 and the load levels of σ_{gtb}/f_{gtb} equal to 0.3, 0.6 and 0.9 are given in Figure 2.

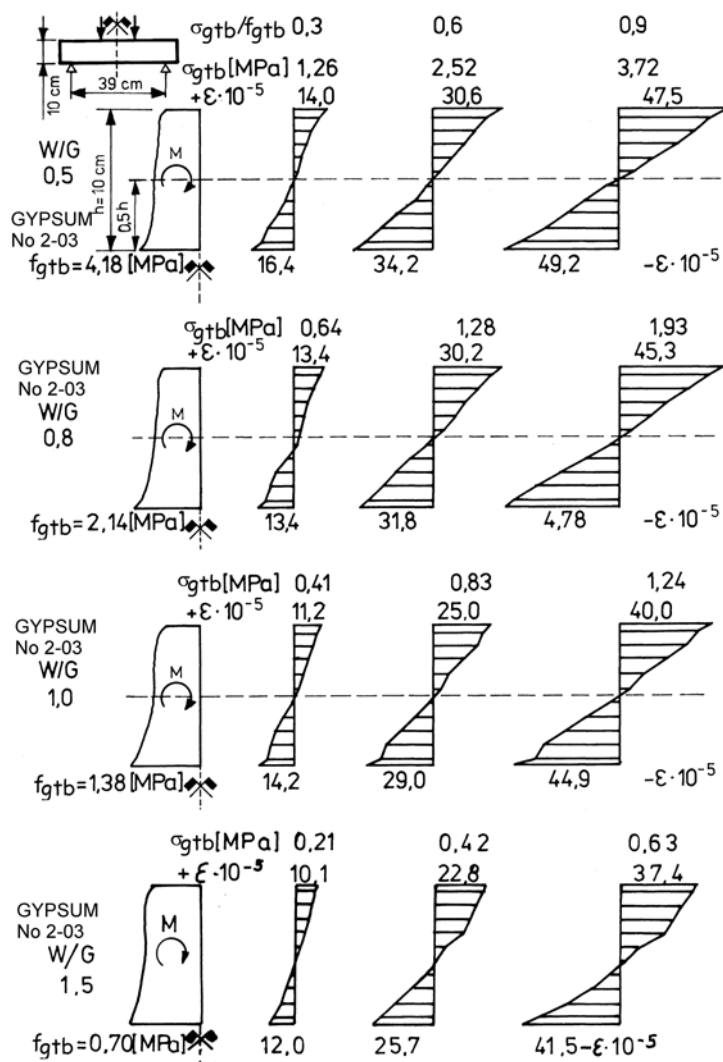


Fig. 2. Distribution of strain values ϵ in the normal cross-sections of bended dry beams made of building gypsum: σ_{gtb} – normal stress in the bended beam (1), f_{gtb} – bending strength, W/G – water-to-gypsum ratio

Tensile stress in bended samples was calculated according to the following standard formula:

$$\sigma_{gtb} = \frac{6M}{bh^2}. \quad (1)$$

Each series of beams manufactured at the same W/G ratio underwent a pilot test, in which their strength f_{gtb} for brittle fracture was determined. The beams were examined with bonded wire strain gauges. The deformation ε at three load levels, i.e. at σ_{gtb}/f_{gtb} equal to 0.3, 0.6 and 0.9, was measured.

Results of the examination shown in Figure 2 suggest that in the whole load range (σ_{gtb}/f_{gtb} is from 0.3 to 0.9) the validity of the Bernoulli distribution may be assumed: flat cross-sections prior and after the strain. However, the bottom tension fibers have the tendency to deform to a greater extent (partial plasticizing). In the whole range of consecutively increasing loads, the neutral axis of the cross-section was maintained, at the technical accuracy, in the geometric center of the beam cross-section. The ratio of the deformation area in the compression zone A_c to the area of the tension zone A_t expressed as

$$\rho_c = \frac{A_c}{A_t} \quad (2)$$

varies within the range from 0.877 to 0.945. Therefore, as the rule, the tensile area prevailed over the compression area in the upper zone. In the whole series of the examinations at $W/G = 0.5, 0.6, 0.8, 1.0, 1.5$, the results of measurements are qualitatively similar.

Figure 3 presents the σ - ε diagrams for the outermost fibers in the bend tests. In Figure 3a, there are collected the σ - ε_{gb}^+ diagrams for the outermost fibers compressed, Figure 3b shows the σ - ε_{gb}^- diagrams for the outermost fibers tensioned, for the $6 \times 10 \times 50$ cm beams and for the $4 \times 4 \times 16$ cm beams made of gypsum paste at W/G ranging from 0.5 to 1.5. The outermost points form an envelope of the ultimate tension values ε_{gtb}^- , which – in the actual conditions of the tests – varied within the range of:

$$\max \varepsilon_{gtb}^- = \varepsilon_{gtu} = (4.5 - 5.6) \cdot 10^{-4} \text{ for the } 6 \text{ cm} \times 10 \text{ cm} \times 50 \text{ cm beams,}$$

$$\max \varepsilon_{gtb}^- = \varepsilon_{gtu} = (5.0 - 6.7) \cdot 10^{-4} \text{ for the } 4 \text{ cm} \times 4 \text{ cm} \times 16 \text{ cm beams.}$$

For the bended plates made of dental gypsum obtained at W/G ranging from 0.6 to 1.0 Denkiewicz [1] obtained similar ε_{gtb}^- values that varied from $5.5 \cdot 10^{-4}$ to $6.0 \cdot 10^{-4}$.

Based on statistical analysis, there was determined an ultimate value of deformation ability for the tension zone ε_{gtb}^- of the bended beams made of building gypsum pastes within a wide range of W/G ratios and for compression strength f_{gc} . At the correlation factor of $R^2 = 0.9892$ it is as follows:

$$\max \varepsilon_{gtb}^- = \varepsilon_{gtu} = 46.24 f_{gc}^{0.0888} \cdot 10^{-5}, \quad (3)$$

where $\max \varepsilon_{gtb}^- = \varepsilon_{gtu}$ is the extreme deformation of the outermost tension “fibres” in the bended element, f_{gc} stands for the compression strength of the pastes.

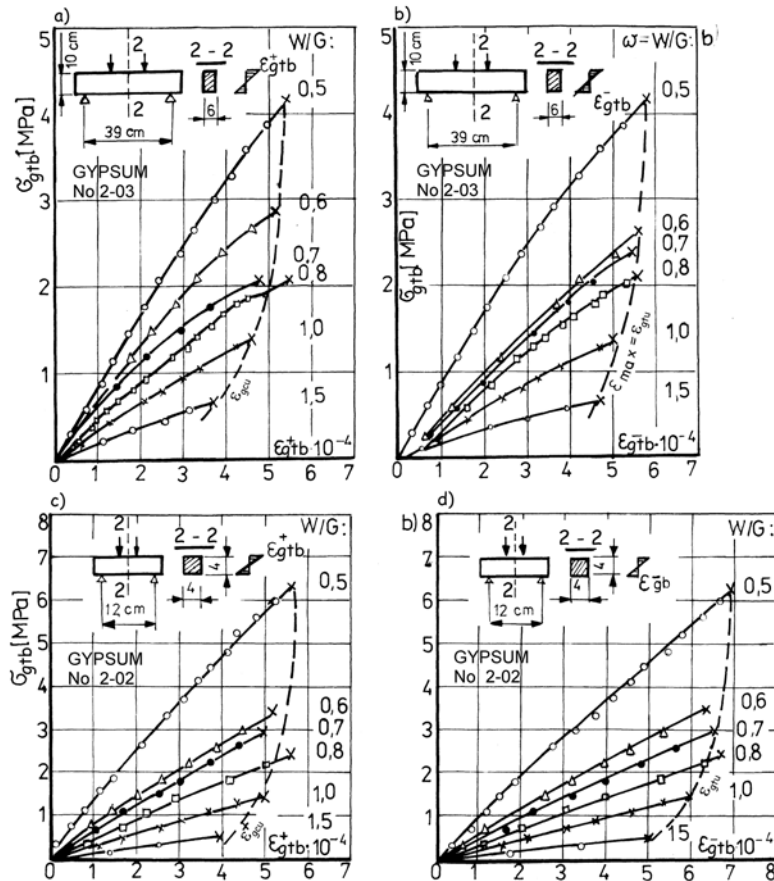


Fig. 3. Function diagrams $\sigma - \varepsilon$ for the outermost fibers of bended dry beams made of building gypsum: a) and c) curves of ε_{gb}^+ for the outermost compressed fibers, b) and d) curves of ε_{gb}^- for the outermost tension fibers, W/G – water-to-gypsum ratio

Figure 4a presents experimental strength functions of the building gypsum 2-03, namely the compression strength $f_{gc} = f(\omega)$ and the bending strength $f_{gtb} = f(\omega)$. Figure 4a shows a considerable reserve of load capacity in the compression zone compared to rather poor strength of the tension zone. In Figure 4b, the values of $\varepsilon_{gtb, \max}^- = \varepsilon_{gtu}$ that increase together with increasing f_{gtb} and are correlated with f_{gc} , strength values, are shown as the function. Figure 4 presents also elastic constants of gypsum determined for the outermost fibers according to the following formulas:

- elastic constant in the compression zone

$$E_{gb}^+ = \frac{\Delta\sigma}{\Delta\varepsilon_{gb}^+}, \quad (4)$$

- elastic constant in the tension zone

$$E_{gb}^- = \frac{\Delta\sigma}{\Delta\varepsilon_{gb}^-}. \quad (5)$$

The constants E_{gb}^+ and E_{gb}^- increase monotonically as the function of diminishing ratios W/G , quite similar to compression strength values $f_{gc} = f(\omega)$. That is why the correlation $E_{gb} = f(f_{gc})$ may be determined in the way similar to the standard procedure used in theory of concrete (Godycki [4], Kamiński [7, 8]).

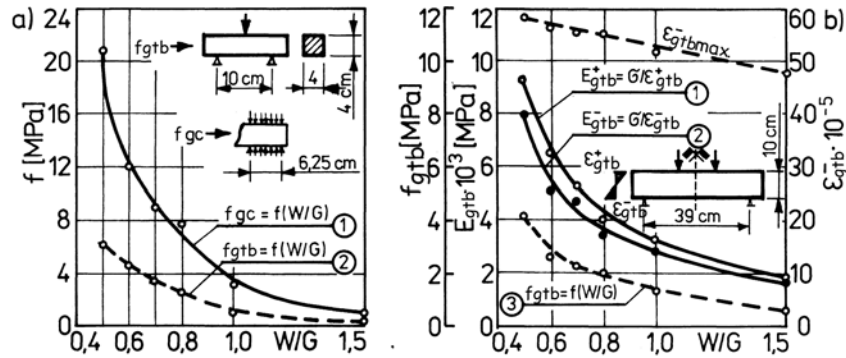


Fig. 4. Dependence of strength of dry cured pastes made of building gypsum 2-03 upon the ratios W/G :

f_{gb} – bending strength, f_{gc} – compressive strength (a); diagrams of the deformations ε and

elastic constants E for cured gypsum pastes at various ratios W/G (b): E_{gb}^+ – deformability module

for the outermost compression fibers, E_{gb}^- – deformability module for the outermost tension fibers,

$\varepsilon_{gtb, \max}^- = \varepsilon_{gtu}$ – ultimate deformation values for the bottom fibers of the bended beams

4. Distribution of internal forces and bending capacity of gypsum beams cross-sections

Figure 5 shows analytical distribution of internal forces in the bended gypsum elements. The linear distribution of internal forces shown as ① in Figure 5 enables determination of the tensile stress of the bending σ_{gtb} and the ultimate strength values f_{gtb} for the outermost fibers at the experimentally determined breaking moment M_n . In diagram ①, which illustrates standard relation (1), the breaking moment M_n is equalized by the moment of internal forces M_1 according to the following relation:

$$M_n = M_1 = 0.1667bh^2 f_{gtb} \quad (6)$$

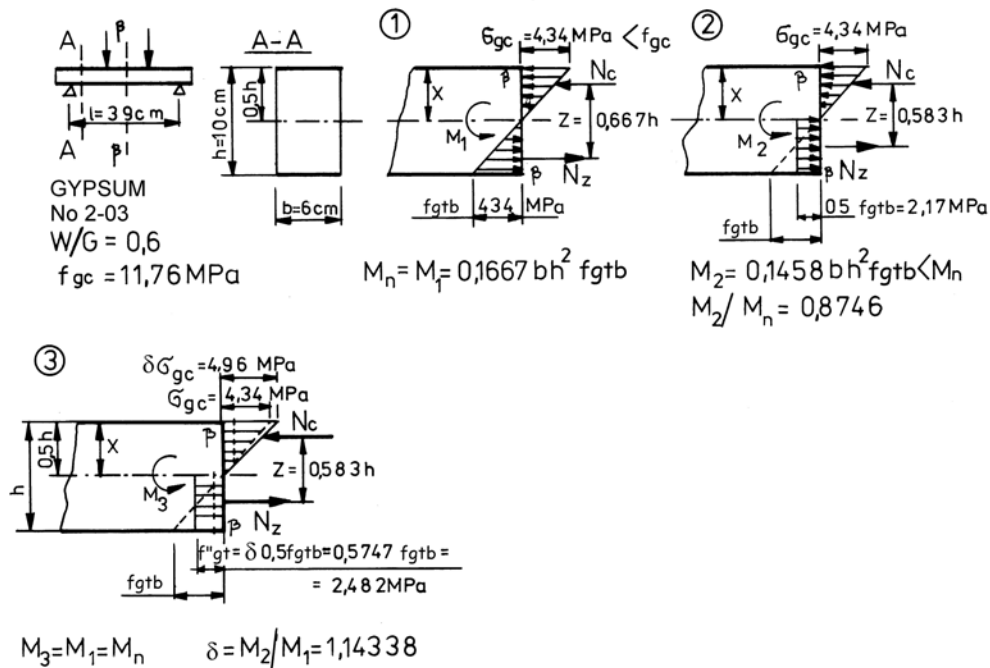


Fig. 5. Diagram of distribution of internal forces in the bended dry gypsum beam obtained at $W/G = 0.6$

However, the tensile strength at bending f_{gtb} determined from relation (6) is considerably higher than tensile strength of gypsum determined in the tests of the axial tension f_{gt} or in the tests of splitting of cylinder samples f'_{gt} . The results of my own experiments suggest that – according to the analysis of data as in Figure 6 – the proportion of f'_{gt} to the tensile strength at bending f_{gtb} (calculated from formula (1)) in the following form:

$$\alpha_1 = \frac{f'_{gt}}{f_{gtb}} = f(f_{gc}) \quad (7)$$

may be approximated to a linear form, $\alpha_1 = f(f_{gc})$, as follows:

$$\alpha_1 = 0.62 - 0.01f_{gc}. \quad (8)$$

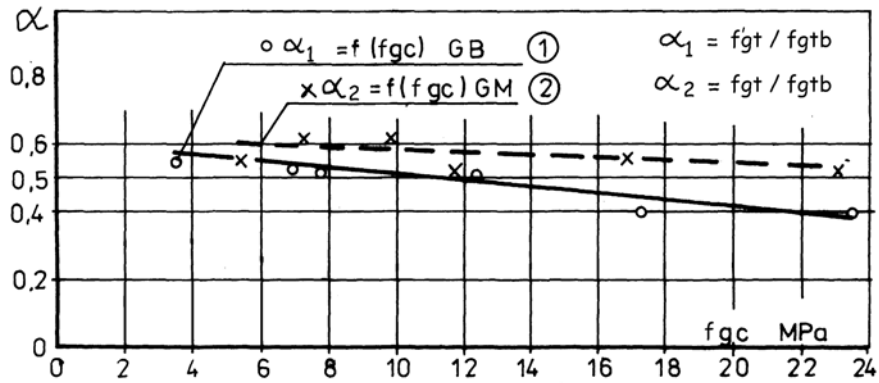


Fig. 6. Graphical data for approximation of the function $\alpha_1 = f'_{gt}/f_{gtb} = f(f_{gc})$ for dry building gypsum (original test results) and of the function $\alpha_2 = f_{gt}/f_{gtb} = f(f_{gc})$ for the gypsum "Molda Normal" (based on the results obtained by Wianecki [30])

From the analysis of the results shown in Figure 6 we can conclude that the value of α_1 for gypsum pastes having the compression strength $f_{gc} < 12.0$ MPa (equivalent to $W/G > 0.6$ for the building gypsum binder GB-N1) amounts to:

$$\alpha_1 > 0.5 \quad \text{for } f_{gc} < 12.0 \text{ MPa, } \quad W/G > 0.6. \quad (9)$$

Based on the results of Wianecki [30], the relation $\alpha_2 = f_{gt}/f_{gtb} = f(f_{gc})$ for the French gypsum "Molda Normal" may be expressed by (Figure 5):

$$\alpha_2 = \frac{f_{gt}}{f_{gc}} = 0.62 - 0.0035f_{gc}. \quad (10)$$

The values of α_2 vary between 0.6 and 0.53 in a wide range of compression strength, namely for f_{gc} between 2 and 22 MPa.

If we assume that the outermost fibers may carry tensile stress equal to $\sigma_{gt} = 0.5f_{gtb}$, we can conclude that the internal force pattern seems like the diagram ② in Figure 5, provided that we also assume a full plasticization of the tensile zone

according to the classic theory of Muraszew. This theory was developed for the elements with cement binders based on the analysis of bending capacity, according both to the contemporary standards of the Council for Mutual Economic Aid (RWPG, Ryżyński [20]) and the new EU standards (Kamiński et al. [7, 8]). The value of the internal force M_2 calculated for such a scheme is smaller than actual breaking moment:

$$M_2 = 0.1458bh^2 f_{gtb} < M_n, \quad (11)$$

$$M_2 : M_n = 0.8746.$$

The diagram ③ in Figure 5 illustrates the pattern of internal forces calculated analytically in the bended gypsum beam. The pattern agrees with the following experimental facts found objectively:

1. The neutral axis is located in the middle of height of the beam (according to the results of examinations as in Figure 2).
2. The breaking moment of the internal forces M_3 equals to the value of the moment M_n found experimentally.

The conditions assumed for the force pattern as in the diagram ③ in Figure 5 suggest the possibility of determining the representative calculated tensile strength of cured gypsum bended f_{gt}'' (as dry) in the following form:

$$f_{gt}'' = \delta 0.5 f_{gtb} = 0.5747 f_{gtb}, \quad (12)$$

where the correction coefficient δ increases the stresses both in the compression and in the tensile zones to meet the condition of $M_3 = M_n$; the coefficient $\delta = M_2/M_1 = 1.14338$.

The cracking moment M_r , equal to the moment M_n , which breaks the dry bended beam made of not-reinforced gypsum may be calculated from the formula:

$$M_r = M_n = W_{gep} f_{gt}'', \quad (13)$$

where W_{gep} stands for the elastoplastic bending strength factor.

The W_{gep} values were calculated in the following analyzes:

- condition of strength:

$$M_n \leq W_{gep} f_{gt}'' = W_{gep} \delta \cdot 0.5 f_{gtb} = W_{gep} \delta \cdot 0.5 \frac{6M_n}{bh^2}; \quad (14)$$

- after division of the both sides by M_n one obtains:

$$1 \leq W_{gep} \delta \cdot 0.5 \frac{1}{W_{ge}}, \quad (15)$$

where W_{ge} is an “elastic” bending strength factor equal to:

$$W_{ge} = \frac{bh^2}{6}; \quad (16)$$

• after transformation of formula (15), the searched value of the elastic/plastic bending strength factor W_f may be obtained in the following form:

$$W_{gep} = \frac{W_{ge}}{0.5\delta} = \beta W_{ge} = 1.7496W_{ge}. \quad (17)$$

After substitution of Equation (17) for Equation (16), one can obtain the searched formula for the W_{gep} factor, namely:

$$W_{gep} = 1.7496 \frac{bh^2}{6} = 0.2916bh^2. \quad (18)$$

The relation derived based on original results of bending tests carried out with dry gypsum beams proved to be identical with that used in the standard of concrete structures [23] for calculation of cross-sections of bended plain concrete beams.

Finally, after substitution of (18) for (14), one can obtain the following formula for the load capacity of the bended cross-sections of dry gypsum elements:

$$M_n = W_{gep} f_{gt}'' = 0.2916bh^2 f_{gt}''. \quad (19)$$

After making use of the results of our own strength determination studies [12], $f_{gtb} = f(G/W)$, according to the following formula:

$$f_{gtb} = 1.533\omega'^{1.77}, \quad (20)$$

the calculated value of tension strength at bending may be determined by the relation:

$$f_{gt}'' = 0.5747 f_{gtb} = 0.5747 \cdot 1.533\omega'^{1.77} = 0.88\omega'^{1.77} \text{ [MPa]}, \quad (21)$$

where $\omega' = G/W$ stands for a dimensionless parameter.

In this way, load capacity of bended dry beams, made of building gypsum at the determined parameter G/W may be obtained by:

$$M_n = 0.2916bh^2 f_{gt}'' = 0.2916bh^2 \cdot 0.88 \left(\frac{G}{W} \right)^{1.77} \cdot 10^3$$

$$= 0.256bh^2 \left(\frac{G}{W} \right)^{1.77} \cdot 10^3 \text{ [kNm]}, \quad (22)$$

where:

b, h – width and height of the gypsum beam cross-section [m],

0.88 – numerical parameter of Equation (22) [MPa],

10^3 – conversion factor, MPa = 10^3 kN/m².

5. Summary and conclusions

Load distribution in normal cross-sections of bended dry gypsum elements is almost linear; however, the deformations on the tension side ε_{gt}^- exceed those of the outermost compressed fibers ε_{gc}^+ , which is in accordance with $\varepsilon_{gt}^- = 1.14 \div 1.06 \varepsilon_{gc}^+$. This results from a natural tendency of the tensile fibers to plasticize, which is equivalent to plastic flow. In such approximation, one can assume the validity of the Bernoulli distribution: flat cross-sections prior and after loading. The ultimate deformability of the outermost tensile fibers in the tensile zone, determined in the form of relation (3), has a considerable heuristic value and gives information about ultimate deformation ability of dry gypsum.

An important result of the study is determination of the moduli of elasticity for outermost fibers of the bended gypsum elements: in the compression zone E_{gtb}^+ and in the tension zone E_{gtb}^- (Figure 4b).

The analyzes of internal force distribution in the cross-sections of the bended gypsum beams proved that reliable calculation results follow the diagram ③ Figure 5, i.e. there occurs full plasticization of the tensile zone. Identical scheme was found by Muraszew [19, 26] for the bended concrete cross-sections. The representative tensile strength of bended gypsum f_{gt}'' (relation (12)), and elastic/plastic bending strength factor W_f (relations (17) and (18)) are the original findings on these phenomena in gypsum cross-sections.

The general relations (19) and (22), which describe the load capacity of bended elements in normal cross-sections as a function of dimensions of the cross-section and of the W/G ratio, are of a considerable heuristic and practical value in the case of interpolation of test results for gypsum construction models.

References

- [1] Denkiewicz J.: *Analiza cech tworzywa gipsowego jako materialu do modelu do badań konstrukcji z betonu (Analysis of the features of gypsum as the material for examination of concrete structures)*, PhD, Politechnika Śląska, Gliwice, 1970.

-
- [2] Ekogips. Nowy system budownictwa. Ekogips S.A., Warszawa, ul. Barycka 26. Aprobata techniczna ITB, Warszawa, 1994, nr AT-15-2760/97.
- [3] Ferronskaja A.W.: *Dolgowiecznost gipsowych materialow, izdelij i konstrukcji*, Moscow, Strizdat, 1984.
- [4] Godycki-Ćwirko T.: *Mechanika betonu*, Arkady, Warszawa, 1982.
- [5] Hanusch H.: *Gipskartonplatten. Trockenbau. Montagebau. Ausbau*, Verlagsgesellschaft R. Müller, Köln, 1978.
- [6] Jeulin D., Monnaie P., Peronnet F.: *Gypsum morphological analysis and modeling*, Cement and Concrete Composites, 2001, 23, 299–311.
- [7] Kamiński M., (Editor): *Podstawy projektowania konstrukcji żelbetowych według Eorokodu 2*, Wydawnictwo Naukowe PWN, Warszawa–Wrocław, 1996.
- [8] Kamiński M., Szechiński M., Ubysz A.: *Teoretyczne i praktyczne podstawy obliczania ugięć elementów żelbetowych*, Dolnośląskie Wydawnictwo Naukowe, Wrocław, 1998.
- [9] Klin S.: *Budownictwo z gipsu w Polsce*, Materiały Budowlane, 1998, nr 10, 42–47.
- [10] Klin S.: *Oznaczanie wytrzymałości gipsu na rozciąganie różnymi metodami. Cz. I. Metody oznaczeń. Oznaczanie wytrzymałości gipsu w stanie suchym*, Cement Wapno Gips, 1987, nr 12, 261–267.
- [11] Klin S.: *Oznaczanie wytrzymałości gipsu na rozciąganie różnymi metodami. Cz. II. Oznaczanie wytrzymałości w stanie nasycenia wodą*, Cement Wapno Gips, 1988, nr 1, 1–7.
- [12] Klin S.: *Relacje między wybranymi cechami stwardniałych zaczynów gipsowych*, Zeszyty Naukowe Instytutu Budownictwa Politechniki Wrocławskiej, 1991, nr 64, 67–71.
- [13] Lewandowski W.: *Ściany wewnętrzne i zewnętrzne w systemie SOVA-SYSTEM z pustaków gipsowych*, Świadectwo ITB nr 901/92, Materiały Budowlane, 1990, nr 4.
- [14] Liaszkiewicz I.M.: *Effektywnyje stroitielnyje materialy na osnovie gipsa i fosfogipsa*, Mińsk, Wyższaja Szkoła, 1989.
- [15] Mazur S.: *Eksperymentalny domek gipsowy we Wrocławiu*, Przegląd Budowlany, 1958, nr 2.
- [16] Meuś W., Rzepecki R.: *Elementy i konstrukcje z tworzyw gipsowych i gipsobetonów*, Arkady, Warszawa 1963.
- [17] Mikoś J.: *Budujemy z gipsu. Informator*, Wydawnictwo Instytutu Ekonomiki Przemysłu Chemicznego, Gliwice, 2004.
- [18] Mikoś J.: *PRAS-GIPS – uprzemysłowiony system budownictwa jednorodzinnego*, Przegląd Budowlany, 1980, nr 7.
- [19] Muraszew W.J.: *Treszczinostojcziwost i procznost żelbetona*, Maszstrojizdat, Moscow, 1950.
- [20] Objawiński R.: *Pustaki gipsowe typu RC. Świadectwo ITB nr 536/85*, Warszawa, 1985.
- [21] PN-B-03002:1987. *Konstrukcje murowe. Obliczenia statyczne i projektowanie.*
- [22] PN-B-03002:1999. *Konstrukcje murowe niezbrojone. Projektowanie i obliczanie.*
- [23] PN-B-03264:1984. *Konstrukcje betonowe, żelbetowe i sprężone. Obliczenia statyczne i projektowanie.*
- [24] Rolek L.: *System R*, Materiały Budowlane, 1998, nr 10.
- [25] Rolek R., Krajewski J.: *Sposób wykonywania monolitycznych konstrukcji żelbetowych w deskowaniach traconych z gipsu lub tworzywa gipsowego łącznie ze wznoszeniem ścian osłonowych*, Patent P 290394, 1998.

- [26] Ryżyński A.: *Obliczanie momentu powodującego zarysowanie elementu żelbetowego w oparciu o teorię Muraszewa*, Inżynieria i Budownictwo, 1966, nr 10, 405–407.
- [27] Smih R.G., Orangun C.O.: *Gypsum Plaster Models of Unbonded Prestressed Concrete Beams*, Civil Engineering of Public Works Review. Part 1, 1961, No. 660, 906–909.
- [28] Soroka J., Sereda P.J.: *Interrelation of hardness, modules of elasticity and porosity in various gypsum systems*, Journal of the American Society, 1968, Vol. 51, No. 6, 335–340.
- [29] Urban L.: *Hydrofobowe gipsowe prefabrykaty ścienne typu K*, Materiały Budowlane, 1990, nr 10, 17–20.
- [30] Wianecki J.: *Proprietes mecanique du platre de Paris eu due de son utilisation comme materiau pour modeles reduits*, Biull. RILEM, 1963, No. 20, 103–112.
- [31] Wołżenski A.W.: *O perspektywach proizvodstwa i primienienija gipsowych metrialow w stroitelstwie*, Stroitelnyje Materialy, 1985, nr 10, 17–18.

Rozkład odkształceń i naprężeń w przekrojach normalnych zginanych elementów gipsowych

Przedstawiono wyniki badań rozkładu odkształceń i naprężeń w przekrojach normalnych zginanych belek gipsowych w stanie suchym. Belki te wykonano z zaczynów gipsu budowlanego o $W/G = 0,5; 0,6; 0,8; 1,0$ i $1,5$. Odkształcenia zmierzono metodą tensooporową, a ugięcia belek – za pomocą czujników przemieszczeń. Stwierdzono prawie liniowe rozkłady odkształceń zgodnie z zasadą Bernoulliego dla poziomych wytyżeń aż do $\sigma_{gt}/f_{gt} = 0,9$. Określono graniczne wartości odkształceń w strefie rozciąganej w postaci zależności $\varepsilon_{gtb}^- = 46,24 f_{gc}^{0,0888} \cdot 10^{-5}$. Dokonano analizy różnych schematów rozkładu sił wewnętrznych, czyli naprężeń w zginanych przekrojach normalnych. Przyjęto obliczeniowy schemat: trójkątny w strefie ściskanej i prostokątny w strefie rozciąganej. Ustalony na podstawie badań własnych rozkład jest zgodny z teorią Muraszewa opracowaną dla przekrojów betonowych. Określono reprezentatywną wytrzymałość gipsu na rozciąganie przy zginaniu $f_{gt}'' = 0,5\delta f_{gtb} = 0,574 f_{gtb}$, gdzie f_{gtb} oznacza wytrzymałość normatywną jak dla materiałów sprężystych. Ustalono sprężysto-plastyczny wskaźnik wytrzymałości na zginanie dla przekrojów gipsowych w postaci związku $W_{gep} = W_{ge} / 0,5\delta = 1,7496 W_{ge}$, gdzie: $W_{ge} = bh^2 / 6$ jak dla materiałów sprężystych. Ustalono zależność określającą nośność przekrojów gipsowych na zginanie w postaci $M_n = W_{gep} f_{gt}''$.



Optimization of composite structure shape with boundary element method approach

PIOTR KONDERLA

Wrocław University of Technology, Wybrzeże Wyspiańskiego 27, 50-370 Wrocław

Composite structures consisting of thin reinforced laminas, modelled as orthotropic bodies, are considered. The problem of the optimal shape is examined within the scope of sensitivity and optimization theories, particular consideration being given to shape sensitivity and optimal shape design. The boundary element method (BEM) approach has been formulated and implemented in the computer code, which allows the problem to be solved numerically. The design of the optimal shape for the specimen which was used to test the composite material under biaxial stress conditions is presented as a numerical example.

Keywords: *optimization, sensitivity, composite material, boundary element method, orthotropic body*

1. Introduction

Flat composite structures, laminates consisting of thin reinforced laminas, are considered. Each of the laminas is modelled as an orthotropic body, and one of the principal directions is parallel to the reinforcement of the laminas. In the laminate, any individual laminas of identical orthotropic properties are mutually rotated in such a way that the laminate as a homogeneous body is an orthotropic body.

In the paper, the optimal shape problem is examined within the scope of sensitivity and optimization theories, particular consideration being given to the shape sensitivity and optimal shape design. This is one of the most difficult problems dealt with in optimization theories. Analytical solutions can be obtained only for some simple problems, and that is why use is commonly made of numerical methods such as FEM, FDM and BEM. In the case of shape sensitivity analysis, the boundary element method becomes an especially favourable numerical technique owing to the properties of the discrete models. The parameters of the discrete model are located on the boundary of the domain, and any change in the location of the boundary during the optimization process is noticed by these parameters in a natural way. Each change in the location of the boundary entails modification of the discrete model. In the past few years, the optimizations of construction shape as well as relevant sensitivity analysis have been the subject of numerous scientific researches [1, 2]. The results of those investigations were used for the needs of the study reported on in this paper.

The objective of the study was to investigate the BEM algorithm. The BEM approach was formulated and implemented in the computer code, which allows the problem to be solved numerically. The optimal shape design for the specimen which

was used to test the composite material under biaxial stress conditions is presented as a numerical example [3].

2. Physical model of the composite material

The composite material specimen (Figure 1) is the subject of optimization. It is used for investigating the biaxial state of stress. The specimen consists of identical thin laminas connected and uniaxially reinforced. Two laminas are assumed to lie in the centre of the specimen Ω_I and 8 laminas in the other area Ω_{II} . The laminas in the laminate are arranged alternately according to the direction of reinforcement $[0^\circ, 90^\circ]$ with reference to the direction x_1 .

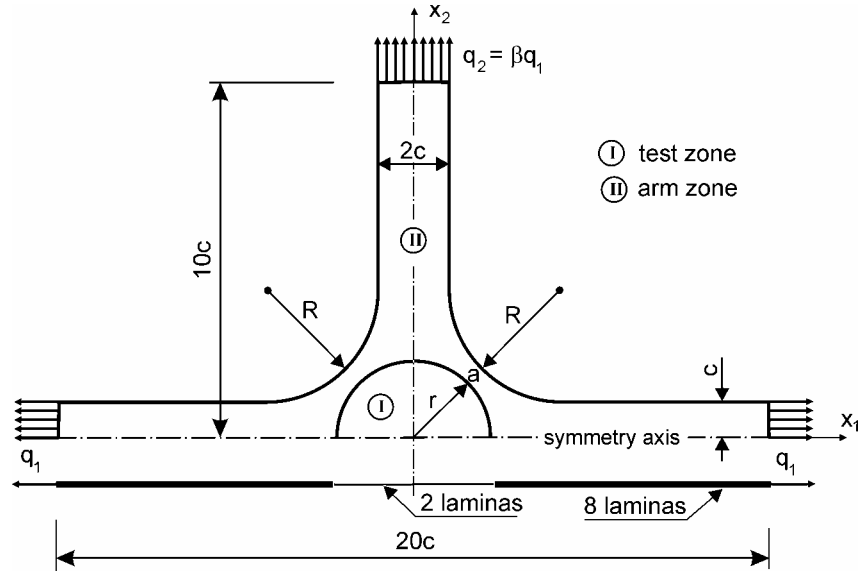


Fig. 1. Static scheme of composite material specimen

It has been assumed that the physical model of a single lamina is an orthotropic elastic-ideally plastic material in a plane state of stress. For each lamina, a local coordinate system $\{\hat{x}_1, \hat{x}_2\}$ compatible with the principal directions of orthotropy is defined and standard descriptions of the fields of stress and strain in the vector form are adopted:

$$\hat{\boldsymbol{\sigma}} = \begin{Bmatrix} \hat{\sigma}_1 \\ \hat{\sigma}_2 \\ \hat{\sigma}_6 \end{Bmatrix}, \quad \hat{\boldsymbol{\varepsilon}} = \begin{Bmatrix} \hat{\varepsilon}_1 \\ \hat{\varepsilon}_2 \\ \hat{\varepsilon}_6 \end{Bmatrix} = \begin{Bmatrix} \partial \hat{u}_1 / \partial \hat{x}_1 \\ \partial \hat{u}_2 / \partial \hat{x}_2 \\ \partial \hat{u}_1 / \partial \hat{x}_2 + \partial \hat{u}_2 / \partial \hat{x}_1 \end{Bmatrix}, \quad (1)$$

where two of the first coordinates of the stress vector indicate normal stresses in the directions \hat{x}_1 and \hat{x}_2 , respectively, and the third coordinate is shear stress. The strain vector is defined by the linear Cauchy equations (1).

The material is a Hooke's body in the range of elastic deformations, and the constitutive equations for the n^{th} lamina in the local coordinate system take the form:

$$\begin{Bmatrix} \hat{\sigma}_1 \\ \hat{\sigma}_2 \\ \hat{\sigma}_6 \end{Bmatrix}^{(n)} = \begin{bmatrix} \hat{Q}_{11} & \hat{Q}_{12} & 0 \\ \hat{Q}_{21} & \hat{Q}_{22} & 0 \\ 0 & 0 & \hat{Q}_{66} \end{bmatrix}^{(n)} \begin{Bmatrix} \hat{\epsilon}_1 \\ \hat{\epsilon}_2 \\ \hat{\epsilon}_6 \end{Bmatrix}^{(n)} \Rightarrow \hat{\boldsymbol{\sigma}}^{(n)} = \hat{\mathbf{Q}}^{(n)} \hat{\boldsymbol{\epsilon}}^{(n)}, \quad (2)$$

where

$$\hat{Q}_{11} = \frac{E_1}{1 - \nu_{12}\nu_{21}}, \quad \hat{Q}_{22} = \frac{E_2}{1 - \nu_{12}\nu_{21}}, \quad \hat{Q}_{12} = \hat{Q}_{21} = \nu_{12}\hat{Q}_{22} = \nu_{21}\hat{Q}_{11}, \quad \hat{Q}_{66} = G_{12}, \quad (3)$$

and $E_1, E_2, \nu_{12}, G_{12}$ are material constants of the material of the lamina.

We assume the global coordinate system $\{x_1, x_2\}$, and $\boldsymbol{\sigma}^{(n)}$ and $\boldsymbol{\epsilon}^{(n)}$ stand for the stress and strain vectors of the n^{th} lamina in this system. The transformation equations for expressing stresses in an $\{x_1, x_2\}$ global coordinate system in terms of stresses in a $\{\hat{x}_1, \hat{x}_1\}$ local coordinate system take the form [9]

$$\boldsymbol{\sigma}^{(n)} = \mathbf{T}_{(n)} \hat{\boldsymbol{\sigma}}^{(n)}, \quad (4)$$

where

$$\mathbf{T}_{(n)} = \begin{bmatrix} \cos^2 \theta & \sin^2 \theta & -2 \sin \theta \cos \theta \\ \sin^2 \theta & \cos^2 \theta & 2 \sin \theta \cos \theta \\ \sin \theta \cos \theta & -\sin \theta \cos \theta & \cos^2 \theta - \sin^2 \theta \end{bmatrix}. \quad (5)$$

The angle θ is the angle from the global x_1 -axis to the local \hat{x}_1 -axis of the n^{th} lamina in anticlockwise direction.

By virtue of similarly, the strain transformation equations are

$$\hat{\boldsymbol{\epsilon}}^{(n)} = \mathbf{T}_{(n)}^T \boldsymbol{\epsilon}^{(n)}. \quad (6)$$

Making use of expressions (4) and (6) the constitutive Equations (2) for the n^{th} lamina in the global coordinate system can be written as

$$\boldsymbol{\sigma}^{(n)} = \mathbf{T}_{(n)} \hat{\mathbf{Q}}^{(n)} \mathbf{T}_{(n)}^T \boldsymbol{\varepsilon}^{(n)} = \mathbf{Q}^{(n)} \boldsymbol{\varepsilon}^{(n)}, \quad (7)$$

where

$$\mathbf{Q}^{(n)} = \mathbf{T}_{(n)} \hat{\mathbf{Q}}^{(n)} \mathbf{T}_{(n)}^T = \begin{bmatrix} Q_{11} & Q_{12} & Q_{13} \\ Q_{21} & Q_{22} & Q_{23} \\ Q_{31} & Q_{32} & Q_{33} \end{bmatrix} \quad (8)$$

in which

$$\begin{aligned} Q_{11} &= \hat{Q}_{11} \cos^4 \theta + 2(\hat{Q}_{12} + 2\hat{Q}_{66}) \sin^2 \theta \cos^2 \theta + \hat{Q}_{22} \sin^4 \theta, \\ Q_{12} &= (\hat{Q}_{11} + \hat{Q}_{22} - 4\hat{Q}_{66}) \sin^2 \theta \cos^2 \theta + \hat{Q}_{12} (\sin^4 \theta + \cos^4 \theta), \\ Q_{22} &= \hat{Q}_{11} \sin^4 \theta + 2(\hat{Q}_{12} + 2\hat{Q}_{66}) \sin^2 \theta \cos^2 \theta + \hat{Q}_{22} \cos^4 \theta, \\ Q_{16} &= (\hat{Q}_{11} - \hat{Q}_{12} - 2\hat{Q}_{66}) \sin \theta \cos^3 \theta + (\hat{Q}_{12} - \hat{Q}_{22} + 2\hat{Q}_{66}) \sin^3 \theta \cos \theta, \\ Q_{26} &= (\hat{Q}_{11} - \hat{Q}_{12} - 2\hat{Q}_{66}) \sin^3 \theta \cos \theta + (\hat{Q}_{12} - \hat{Q}_{22} + 2\hat{Q}_{66}) \sin \theta \cos^3 \theta, \\ Q_{66} &= (\hat{Q}_{11} + \hat{Q}_{22} - 2\hat{Q}_{12} - 2\hat{Q}_{66}) \sin^2 \theta \cos^2 \theta + \hat{Q}_{66} (\sin^4 \theta + \cos^4 \theta). \end{aligned}$$

If $\boldsymbol{\sigma}$ and $\boldsymbol{\varepsilon}$ are stress and strain vectors of the laminate, then for the connected laminas we can write

$$\boldsymbol{\varepsilon}^{(n)} = \boldsymbol{\varepsilon} \quad \text{for } n = 1, 2, \dots, N \quad (9)$$

and

$$\boldsymbol{\sigma} = \frac{1}{N} \sum_{n=1}^N \boldsymbol{\sigma}^{(n)} = \frac{1}{N} \sum_{n=1}^N \mathbf{Q}^{(n)} \boldsymbol{\varepsilon}^{(n)} = \mathbf{Q} \boldsymbol{\varepsilon}, \quad (10)$$

where N is the number of laminas in the laminate, and

$$\mathbf{Q} = \frac{1}{N} \sum_{n=1}^N \mathbf{Q}^{(n)}. \quad (11)$$

Because of the symmetrical arrangement of the laminas in the laminates, the matrix \mathbf{Q} is also symmetrical and the laminate after homogenization is an orthotropic body, in which the axes x_1 and x_2 are the principal axes of orthotropy.

It is assumed that the failure of each lamina follows the Tennyson failure criterion

[4]. The function of this yield criterion at the stress space is

$$A_1\hat{\sigma}_1 + A_2\hat{\sigma}_2 + A_6\hat{\sigma}_6 + A_{11}\hat{\sigma}_1^2 + A_{22}\hat{\sigma}_2^2 + A_{66}\hat{\sigma}_6^2 + 2A_{12}\hat{\sigma}_1\hat{\sigma}_2 + 3A_{112}\hat{\sigma}_1^2\hat{\sigma}_2 + 3A_{122}\hat{\sigma}_1\hat{\sigma}_2^2 + 3A_{166}\hat{\sigma}_1\hat{\sigma}_6^2 + 3A_{266}\hat{\sigma}_2\hat{\sigma}_6^2 = 1. \quad (12)$$

The values of the elasticity coefficients and those of the tensor coefficients in Equation (12) for the 3M SP288-T300 GRE composite material have been obtained by Tennyson [4] (see Table 1 and Table 2). It is assumed that the failure of the laminate will occur if the state of stress in one of the laminas reaches the failure surface (the first ply failure criterion).

Table 1. The elasticity coefficients for the 3M SP288-T300 GRE composite material

E_1 [GPa]	E_2 [GPa]	G_{12} [GPa]	ν_{12}
141.34	9.650	4.095	0.26

Table 2. The failure criterion coefficients for the 3M SP288-T300 GRE composite material

A_1 [MPa ⁻¹]	A_2 [MPa ⁻¹]	A_6 [MPa ⁻¹]	A_{11} [MPa ⁻²]	A_{22} [MPa ⁻²]	A_{66} [MPa ⁻²]
-3.602e-4	1.503e-2	0.0	8.921e-7	8.280e-5	1.088e-4
A_{12} [MPa ⁻²]	A_{112} [MPa ⁻³]	A_{122} [MPa ⁻³]	A_{166} [MPa ⁻³]	A_{266} [MPa ⁻³]	
-4.697e-6	-8.842e-10	-1.550e-8	-1.272e-8	-3.130e-7	

For further analysis we defined the relative effort measure (REM) of a laminate. The algorithm for determining this measure is as follows:

- we perform statical analysis to obtain the state of strain for a laminate $\boldsymbol{\varepsilon}$, and with Equation (9) we have $\boldsymbol{\varepsilon}^{(n)} = \boldsymbol{\varepsilon}$ for $n = 1, 2, \dots, N$,
- we calculate the strain and stress in individual laminas, $\hat{\boldsymbol{\varepsilon}}^{(n)}, \hat{\boldsymbol{\sigma}}^{(n)}$ ($n = 1, 2, \dots, N$), using Equations (6) and (2),
- incorporating the term $\zeta_{(n)}\hat{\boldsymbol{\sigma}}^{(n)}$ into Equation (12), we obtain

$$B_3\zeta_{(n)}^3 + B_2\zeta_{(n)}^2 + B_1\zeta_{(n)} = 1 \quad \text{for } n = 1, 2, \dots, N. \quad (13)$$

The REM $\zeta_{y(n)}$ is the value of the minimal positive root of Equation (13). This measure is a multiplier of the stress vector such that the point $\zeta_{y(n)}\hat{\boldsymbol{\sigma}}^{(n)}$ in the stress space lies on the yield surface of one of the laminas.

3. Formulation of the optimization problem

For the composite samples under study, the optimization problem can be formulated as follows: we have to calculate the dimensions of the specimen in such a way that the difference in the effort measure between the domain Ω_I and the domain Ω_{II}

takes a maximal value. In that case, the probability of specimen failure in the domain Ω_{II} will be minimal.

We assumed the objective function in the form of the following stress criterion:

$$\Psi = \zeta_{y(I)}^0 - \zeta_{y(II)}^{\max}, \quad (14)$$

where $\zeta_{y(I)}^0$ denotes the REM at the central point of the specimen and $\zeta_{y(II)}^{\max}$ stands for the maximal REM in the domain Ω_{II} (arm zones).

The relative dimensions of the specimen are assumed as design parameters

$$\mathbf{b} = (b_1, b_2)^T \equiv (\bar{r}, \bar{a})^T = \left(\frac{r}{c}, \frac{a}{c} \right)^T, \quad (15)$$

where the dimensions r , a and c are shown in Figure 1.

At the same time we assume that the loads of the specimen satisfy the following relations:

$$\begin{aligned} q_1 &= \text{const.}, \\ \beta &= q_2 / q_1 \in \langle 0, 1 \rangle. \end{aligned}$$

4. BEM algorithm for static analysis of the construction

Consider a weightless orthotropic body occupying a plane domain $\Omega = \Omega_I \cup \Omega_{II}$ bounded by the boundary $\Gamma = \Gamma_1 \cup \Gamma_2 \cup \Gamma_3 \cup \Gamma_4$, (Figure 2). On the boundary Γ_1 , homogeneous kinematic boundary conditions in the direction normal to the boundary are applied; on the boundary Γ_4 , the loads depicted in Figure 1 are applied; the boundary Γ_3 is free, and the boundary Γ_1 separates the subdomains.

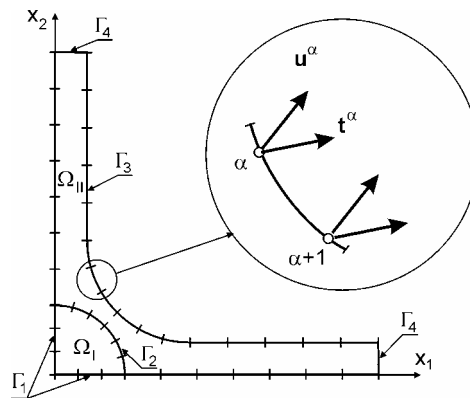


Fig. 2. Discrete model of the domains

The starting point of start for the algorithm is the Somiliano integral equation [5]:

$$\mathbf{C}\mathbf{u}(\xi) = \int_{\Gamma} \mathbf{G}(\mathbf{x}, \xi) \mathbf{t}(\mathbf{x}) d\Gamma - \int_{\Gamma} \mathbf{F}(\mathbf{x}, \xi) \mathbf{u}(\mathbf{x}) d\Gamma, \quad (16)$$

which is equivalent to the set of differential equations describing the plane problem. Equation (16) defines the displacement vector of the point ξ and relates it to the displacements and traction forces on the boundary Γ . The function matrixes $\mathbf{G}(\mathbf{x}, \xi)$ and $\mathbf{F}(\mathbf{x}, \xi)$ are functions of a fundamental solution and matrix \mathbf{C} depends on the boundary smoothness. The fundamental solution for an orthotropic plane body has been found by Butterfield and Tomlin [6], who made use of Lekhnitskii's solution [7].

The algorithm reduced to the numerical solution of the integral Equation (16). The main elements of the algorithm in the direct version are presented as follows:

a) A finite dimension numerical model is matched to the domain Γ . The boundary of each subdomain Ω_{I} and Ω_{II} is divided into disjoint elements $\Gamma_{(e)}$ ($e = 1, 2, \dots, \bar{e}$), with nodal points \mathbf{x}^{α} ($\alpha = 1, 2, \dots, \bar{\alpha}$). Note that on the common boundary of the subdomains Γ_2 there are formally double elements and nodal points. For the numerical model it is assumed that the common elements and nodal points belonging to Ω_{I} and Ω_{II} overlap. With such a behavioural pattern it is convenient to formulate the boundary conditions.

b) The main parameters of the problem are the displacements \mathbf{u}^{α} and the traction forces \mathbf{t}^{α} in the nodal points (Figure 2). The nodal points are regularly arranged inside the element, not at the ends of the element. The position of the nodal points at the ends of the element may complicate the algorithm.

c) The displacement functions $\mathbf{u}(\mathbf{x})$ and the traction forces $\mathbf{t}(\mathbf{x})$ on the boundary Γ are composed of local approximations of these functions; thus

$$\begin{aligned} \mathbf{u}(\mathbf{x}) &= \mathbf{N}_{\alpha}(\mathbf{x}) \mathbf{u}^{\alpha}, \\ \mathbf{t}(\mathbf{x}) &= \mathbf{N}_{\alpha}(\mathbf{x}) \mathbf{t}^{\alpha}, \end{aligned} \quad (17)$$

where $\mathbf{N}_{\alpha}(\mathbf{x})$ is a polynomial base function connected with the nodal point \mathbf{x}^{α} . This function is nonzero only if the element includes a nodal point \mathbf{x}^{α} ($\mathbf{x}^{\alpha} \in \Gamma_{(e)}$). The functions $\mathbf{u}(\mathbf{x})$ and $\mathbf{t}(\mathbf{x})$ in Equation (17) are continuous on the boundary elements. On the boundaries of the elements there are finite discontinuities of these functions as a consequence of the assumed location of the nodal points inside the elements only (not on the element boundaries).

d) For each of the subdomains Ω_h ($h = \text{I, II}$) we write Equation (16), assuming that $\xi = \xi^{\alpha} \equiv \mathbf{x}^{\alpha} \in \Omega_h$:

$$\mathbf{C}\mathbf{u}(\xi^{\alpha}) = \int_{\Gamma_h} \mathbf{G}(\mathbf{x}, \xi^{\alpha}) \mathbf{N}_{\beta}(\mathbf{x}) \mathbf{t}^{\beta} d\Gamma - \int_{\Gamma_h} \mathbf{F}(\mathbf{x}, \xi^{\alpha}) \mathbf{N}_{\beta}(\mathbf{x}) \mathbf{u}^{\beta} d\Gamma, \quad (18)$$

a)
for $\alpha = 1, 2, \dots, \bar{\alpha}$; $h = \text{I, II}$.

Using the notations

$$\begin{aligned}\mathbf{F}_\beta^\alpha &= \int_\Gamma \mathbf{F}(\mathbf{x}, \xi^\alpha) \mathbf{N}_\beta(\mathbf{x}) d\Gamma + \mathbf{C} \delta_\beta^\alpha, \\ \mathbf{G}_\beta^\alpha &= \int_\Gamma \mathbf{G}(\mathbf{x}, \xi^\alpha) \mathbf{N}_\beta(\mathbf{x}) d\Gamma, \\ \mathbf{C} &= \frac{1}{2} \begin{bmatrix} 1 & 0 \\ 0 & 1 \end{bmatrix},\end{aligned}\tag{19}$$

Equation (18) may be written in the form

$$\mathbf{F}_\beta^\alpha \mathbf{u}^\beta - \mathbf{G}_\beta^\alpha \mathbf{t}^\beta = 0.\tag{20}$$

Expression (20) presents a set of $2\bar{\alpha}$ linear algebraic equations including $4\bar{\alpha}$ nodal parameters.

b) Using kinematic and kinetic boundary conditions as well as compatible conditions on the boundary Γ_2 we may solve the set of Equations (20) and determine the nodal parameters \mathbf{u}^α and \mathbf{t}^α for $\alpha = 1, 2, \dots, \bar{\alpha}$

b) Then we calculate the displacement, strain and stress at any point of the domain Ω_h^i ($h = \text{I, II}$). The displacement was obtained using Equation (16). The stress $\boldsymbol{\sigma}(\mathbf{x})$ was established in terms of the differential quotient on the basis of the calculated displacements in the vicinity of the point \mathbf{x} .

1. BEM algorithm for sensitivity analysis of the construction shape

The optimization problem formulated in Section 3 refers to the search for the optimal shape of the construction for which the objective function is maximal. Below a general algorithm is formulated to calculate the sensitivity of the construction when the boundary domain is changed.

For a fixed set of design variables $\mathbf{b} = (b_1, b_2)^T$, the body occupies a domain Ω with the boundary Γ . If one of the design variables changes by about δb_i , the body takes up a domain Ω_τ with the boundary Γ_τ . The transition from the configuration Ω to the configuration Ω_τ can be written in the form of an equation of motion for a body

$$\mathbf{x}_\tau = \mathbf{T}(\mathbf{x}, \tau),\tag{21}$$

where τ is a time parameter, and thus for $\tau = 0$ we have $\mathbf{x}_\tau = \mathbf{x}$.

The velocity of change of the configuration is given by

$$\mathbf{v}(\mathbf{x}, \tau) = \frac{d\mathbf{x}_\tau}{d\tau} = \frac{\partial \mathbf{T}(\mathbf{x}, \tau)}{\partial \tau}, \quad (22)$$

hence

$$\mathbf{x}_\tau(\mathbf{x}, \tau) = \mathbf{x} + \tau \mathbf{v}(\mathbf{x}, \tau). \quad (23)$$

Since the dead load is lacking, the state of stress in the domain Ω_τ at the time $\tau = 0$ depends exclusively on the functions on the boundary Γ_τ (displacements and load tractions). In this case, the objective function Ψ determined by Equation (14) may be written in the form of a functional:

$$\Psi = \int_{\Gamma_\tau} g_\tau(\mathbf{x}_\tau) d\Gamma_\tau. \quad (24)$$

The functions in Equation (21) need to be written with reference to the initial configuration (for the time $\tau = 0$). If we assume the following notation:

- ◆ $\mathbf{n}(\mathbf{x})$ denotes the normal vector on the boundary Γ ,
- ◆ $\mathbf{J} \equiv \begin{bmatrix} \frac{\partial T_i}{\partial x_j} \end{bmatrix} = \mathbf{I} + \tau \begin{bmatrix} \frac{\partial v_i}{\partial x_j} \end{bmatrix} = \mathbf{I} + \tau \mathbf{D}$ is the transformation matrix,
- ◆ $\mathbf{D} \equiv \begin{bmatrix} \frac{\partial v_i}{\partial x_j} \end{bmatrix}$ stands for the transformation velocity matrix,

then Equation (24) can be written in the form [8]:

$$\Psi = \int_{\Gamma} g_\tau(\mathbf{x} + \tau \mathbf{v}(\mathbf{x})) \|\mathbf{J}\| \|\mathbf{J}^{-T} \mathbf{n}\| d\Gamma, \quad (25)$$

where $\|\dots\|$ is euclidean norm and $\mathbf{J}^{-T} \equiv (\mathbf{J}^{-1})^T$.

If the velocity $\mathbf{v}(\mathbf{x})$ is normal to Γ , the material derivative of the functional (25) for $\tau = 0$ is given by

$$\begin{aligned} \Psi' &= \left. \frac{d\Psi}{d\tau} \right|_{\tau=0} = \int_{\Gamma} [\dot{g}(\mathbf{x}) + g(\mathbf{x})(\text{div } \mathbf{v}(\mathbf{x}) - (\mathbf{D}^T \mathbf{n}))] d\Gamma \\ &= \int_{\Gamma} [g'(\mathbf{x}) + \nabla g(\mathbf{x})^T \mathbf{v}(\mathbf{x}) + Hg(\mathbf{x})(\mathbf{v}(\mathbf{x})^T \mathbf{n})] d\Gamma \end{aligned}$$

$$= \int_{\Gamma} [g'(\mathbf{x}) + (\nabla g(\mathbf{x})^T \mathbf{n} + Hg(\mathbf{x}))(\mathbf{v}(\mathbf{x})^T \mathbf{n})] d\Gamma, \quad (26)$$

where:

H is a curvature of the boundary line,

$\dot{g}(\mathbf{x}) = g'(\mathbf{x}) + \nabla g^T \mathbf{v}(\mathbf{x})$ is a material derivative of the function $g(\mathbf{x})$,

$g'(\mathbf{x}) \equiv \lim_{\tau \rightarrow 0} \left[\frac{g_{\tau}(\mathbf{x}) - g(\mathbf{x})}{\tau} \right]$ is a partial derivative of the function $g(\mathbf{x})$.

The material derivative Ψ' can be identified with the design sensitivity of the construction if the following conditions are fulfilled:

- a) the function $\mathbf{T}(\mathbf{x}, \tau)$ in Equation (14) must be a linear function of τ for $\mathbf{x} \in \Gamma$, which means that the trajectory of each point x on the boundary is a segment and that velocity $v(x)$ is independent of τ ,
- b) the boundary line $\mathbf{x}_{\tau} = \mathbf{T}(\mathbf{x}, \tau)$ should correspond with the change of the design variable, i.e. $\delta b_i = \tau$.

If the above conditions are fulfilled, then

$$\Psi' \equiv \Psi'_i = \frac{\partial \Psi}{\partial b_i}. \quad (27)$$

1. Numerical realization of the optimization problem

Making use of the algorithm described in Section 5, we developed our own program which enabled static analysis and optimization of linear elastic composite constructions in the plane state of stress. With this program we optimized the construction shown in Figure 1. The discrete BEM model is depicted in Figure 2. Calculations were carried out with two-nodal elements.

The optimal parameters were determined by iteration, using the algorithm described in Section 5. In the parameter space \mathbf{b}_0 was adopted as the starting point. In the iteration process, further points in the parameter space were determined by the gradient of the objective function (2), first of all the rates of the design variables were assumed according to the expression

$$\delta b_i = \alpha \frac{\partial \Psi}{\partial b_i}, \quad (28)$$

where α is an arbitrary constant.

The path of the sequence of the design parameters obtained by the optimization procedure is shown in Figure 3. For the purpose of control, the functional Ψ at selected grid points of the parameter space was determined and the isolines of Ψ were shown

(as in paper [3]).

The calculations were done by means of the author's computer program.

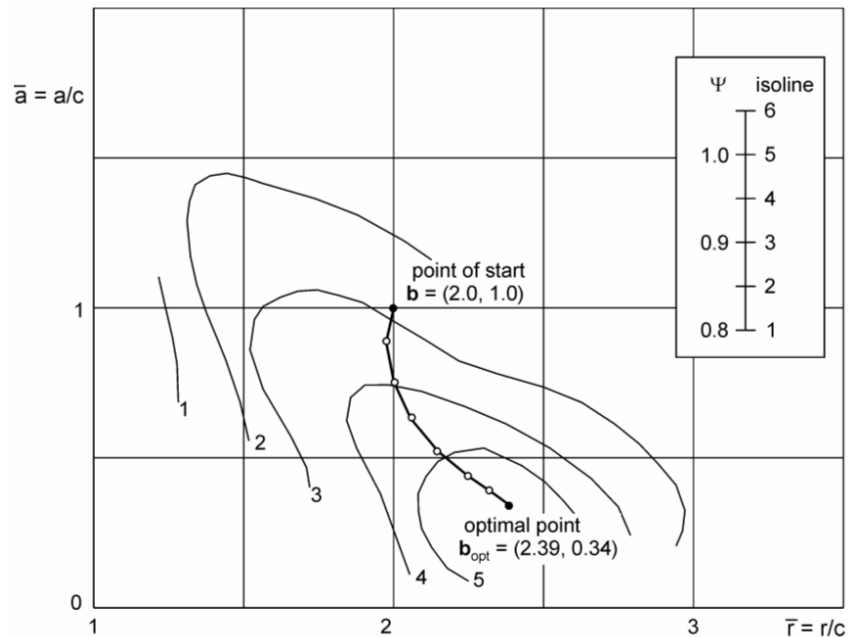


Fig. 3. Isolines of the functional Ψ in the space of design parameters

2. Conclusions

In the paper, the algorithm of the boundary element method for shape optimization has been formulated. The subject to be optimized is an orthotropic body, which consists of identical thin laminas working in the plane stress state. There is a failure criterion for each lamina as a function of the limit surface in the stress space. The first ply failure criterion has been assumed.

The design variables of the defined optimization problem are the geometric parameters of the body shape. The change of the shape in the course of the optimization process is defined by the transformation expression (21) in the form of a motion equation on the assumption that velocity is constant and the velocity vector is perpendicular to the body boundary. The design sensitivity of the objective function is described by Equation (26). It should be noted that the first component of the integrand is a derivative of the function g related to the design variables, the remaining components being directly dependent on the displacement of the boundary.

The example under analysis confirms the efficiency of the BEM algorithm pre-

sented. The results obtained in the study reported on in this paper are consistent with those attained in our previous research [3]. It is an indirect proof of the correctness of the algorithm formulated.

References

- [1] Burczyński T.: *Metoda elementów brzegowych w mechanice*, Wyd. Nauk.-Tech., Warszawa, 1995.
- [2] Dems K., Mróz Z.: *Variational approach by means of adjoint systems to structural optimization and sensitivity analysis-II. Structure shape variation*, Int. J. Solid Structures, 1984, Vol. 20, No. 6, pp. 527–552.
- [3] Konderla P., Sacharuk Z.: *Optimization specimen geometry for biaxially loaded orthotropic materials*, [in:] *Aktualne problemy naukowo-badawcze budownictwa*, XXXV Konf. Nauk. KILiW PAN, Kom. Nauki PZITB, Krynica, 20–27.09.1989. Referaty. T. 1. *Teoria konstrukcji*, Wrocław, 1989, pp. 83–88.
- [4] Tennyson R., Wharram G.: *Evaluation of the Tensor Polynomial Failure Criterion for Composite Materials*, NASA Constructor Rep. 172547, 1985.
- [5] Banerjee P.K., Butterfield R.: *Boundary Element Methods in Engineering Science*, McGraw-Hill Company, London, 1981.
- [6] Tomlin G.R., Butterfield R.: *Elastic analysis of zoned orthotropic continua*, J. Eng. Mech. Division, 1974, 3, pp. 221–234.
- [7] Lekhnitskii S.G.: *Theory of Elasticity of an Anisotropic Elastic Body*, Koldes-Days, San Francisco, 1963.
- [8] Haug E.J., Choi K.K., Komkov V.: *Design Sensitivity Analysis of Structural Systems*, Academic Press Inc., New York, 1986.
- [9] Jones R.M.: *Mechanics of Composite Materials*, McGraw-Hill Book Company, New York, 1975.

Optimalizacja kształtu kompozytowej konstrukcji w ujęciu metody elementów brzegowych

Przedmiotem analizy była kompozytowa konstrukcja złożona z cienkich warstewek zbrojonych włóknami węglowymi. Badano problem optymalnego kształtowania konstrukcji kompozytowej w ujęciu teorii wrażliwości i optymalizacji. Opracowano algorytm numerycznego rozwiązania zadania z wykorzystaniem metody elementów brzegowych. Jako przykład zastosowania tego algorytmu wyznaczono optymalny kształt próbki materiału kompozytowego przeznaczonej do dwuosiowych badań wytrzymałościowych. Obliczenia numeryczne wykonano, korzystając z autorskiego programu komputerowego.